Gravitational Collapse and Holographic Thermalization

Memoria de Tesis Doctoral realizada por

Javier Abajo Arrastia

presentada ante el Departamento de Física Teórica
de la Universidad Autónoma de Madrid
para optar al Título de Doctor en Física Teórica

Tesis Doctoral dirigida por **Dra. Esperanza López Manzanares ,**
Investigadora Científica del Instituto de Física Teórica UAM/CSIC

Departamento de Física Teórica
Universidad Autónoma de Madrid

Instituto de Física Teórica
UAM/CSIC

Diciembre de 2015

A mis padres

Contents

1

Motivation and Summary / Motivación y Resumen

Since long ago physics has succeeded in providing satisfactory descriptions of quantum systems with many interacting degrees of freedom in equilibrium, but only recently, significant steps forward have been taken in order to understand similar systems also out of equilibrium. In the recent years, important advances have been made on experimental setups in different areas, such as optical lattices, ultra cold atoms and heavy ions collisions, while theory has progressed to understand those phenomena not only in the specific fields of condensed matter physics but also in gravitation and high energy physics through the applications of holography theories. This work shows some results about nonequilibrium quantum dynamics that follow from the holographic interpretation of gravity solutions for two specific setups.

The framework is the AdS/CFT correspondence, which has already proven useful in the description of strongly coupled quantum field theories. Ever since the Maldacena conjecture at the end of the last century [6], thermodynamic properties of quantum systems have been studied holographically. In particular, the deconfined phase of strongly coupled field theories at thermodynamic equilibrium corresponds to a black hole in an asymptotically AdS spacetime [9]. Small departs out of equilibrium, describable in terms of linear response theory, have also been interpreted holographically. Especially, the hydrodynamic long wavelength limit has been well understood [15]. In this context the fluid/gravity correspondence has appeared [18]. One of its major successes has been the introduction of holographic plasmas, which behave much like perfect fluids (with very low specific viscosity) [16] and remarkably reproduce experimental data from heavy ion collisions. Moreover, fluid dynamics in non linear regimes have also been understood holographically [17] [18].

In this line of work, further holographic setups have been built in order to describe strongly coupled field theories far from equilibrium. Generically, it is assumed that a macroscopic system brought into a highly excited state will evolve towards a stationary state analogous to thermal equilibrium, in the sense that macroscopic observables will acquire thermal values. The holographic description of such a process has been proposed to correspond to a process of gravitational collapse (i.e. formation of a black hole) [42] [47] [48]. The far from equilibrium evolution of an anisotropic plasma [49] and a boost invariant plasma [50] [51] have been addressed using holography. In [52] the evolution of a massless scalar field minimally coupled to gravity was studied in the limit of small amplitude, and it was already pointed out that non local observables in the strongly coupled field theory, such as Wilson lops and two point functions, could provide important information about the thermalization process, not contained in the simpler one point functions. However, these articles only considered observables extracted from an expansion of the dual gravity background close to the boundary, in particular the one point function

the energy-momentum tensor.

In parallel, further entries of the holographic dictionary were discovered. In particular, a non local observable in the quantum field theory, the entanglement entropy, was put in correspondence with a geometric quantity in the dual spacetime manifold [3]. The entanglement entropy measures the quantum entanglement between some subsystem and its complement at a given time, and is determined by the Von Neumann entropy calculated from the reduced density matrix ρ of such a subsystem. The entanglement entropy has proven useful to track the evolution of systems out of equilibrium, since the entanglement between degrees of freedom at different points is modified by perturbations of the system. Holographically, the entanglement entropy is proportional to the proper area of the extremal surface γ that ends at the boundary of the dual subsystem at the conformal boundary of the AdS spacetime [3][4]. Explicitly, the holographic identification for the entanglement entropy S of the subsystem A is:

$$S_A = -\mathrm{Tr}_A\left(\rho_A \log \rho_A\right) = \frac{\mathrm{Area}(\gamma_A)}{4G_N} \tag{1.1}$$

In general, according to the AdS/CFT correspondence, a quantum state is related globally to a gravity solution. The asymptotic part and the deep inner region of the AdS spacetime are associated with the UV and the IR regimes of the dual field theory, respectively. The precise identification of the local degrees of freedom of the quantum field theory with concrete regions in the dual spacetime is not yet known. However, Equation (1.1) gains further insight into this issue and relates the state of a subsystem, as described by the entanglement entropy, with a specific surface in the dual asymptotic AdS geometry.

The evolution of the holographic entanglement entropy in a dynamical spacetime comprising the formation of a black hole was explicitly studied in [1], confirming the known dual 2-dimensional CFT results [5]. A variety of *holographic thermalization* models has arisen since then, through the study of the holographic entanglement entropy and other geometric quantities in different collapsing scenarios in asymptotically AdS spacetimes [79]-[84].

The results of [1] are restated in Chapter 4. A three dimensional AdS Vaidya spacetime is considered, which represents the gravitational collapse of a shell of null dust or incoherent radiation in AdS. As shown, this setup is dual to a quantum quench, the non equilibrium dynamic evolution of a quantum system after a sudden change in one of the parameters of the hamiltonian. It has been shown how conformal symmetry constrains the dynamics of quantum quenches for a CFT [5]. Besides, quantum quenches can be realized experimentally in systems of cold atoms, together with a subsequent time development under negligible dissipation. The phenomenology is characterized specially by the appearance of effective thermalization with a horizon effect. Namely, thermalization is only observed at the local level over regions whose sizes increase with time. This phenomenon is due to the causal scrambling of quantum correlations over the system, which proceeds at a finite speed v_E. Macroscopic observables for equilibrated systems are equivalent to those obtained for the corresponding systems at thermal equilibrium at a temperature related to the energy provided by the perturbation.

The Vaidya model and a quantum quench differ only in the type of perturbation that determines the initial entanglement pattern and triggers the time evolution. While for the systems considered in the quantum quenches of [5] the entanglement is initially localized on very small scales, in the quenched systems dual to the Vaidya spacetime there are

long range correlations in the initial state. Taking this into account, the same conclusions about the evolution of the entanglement entropy in 2-dimensional CFTs are found in the gravity model. In addition, according to the holographic proposal, it is shown how the evolution is manifestly unitary and the system always remains in a pure state.

Given the essential role that the event horizon plays in the thermodynamic description of a black hole and in turn of the dual thermal state, it arises the question of whether generalized notions of horizon [19][20] may be relevant for the holographic description of a quantum field theory far from equilibrium. In this case, for the dual dynamical spacetime, the apparent horizon is a local object that signals the formation of a singularity, and is more appropriate than the event horizon, which depends on the global causal structure. Whereas for a static black hole the geodesics relevant for the computation of the holographic entanglement entropy do not cross the event horizon, both the event and the apparent horizons are traversed by the corresponding geodesics in the Vaidya model. The holographic results show how these geodesics describe the entanglement entropy of subsystems in the dual field theory after the perturbation, whose portion inside the horizon generates a contribution to the holographic entanglement entropy, which grows linearly with time. This will turn to be the holographic counterpart of the local equilibration observed in the dual CFT quench dynamics. The relation of the slope of the linear increase of the entropy and the slope of the extensive part of the entanglement entropy in thermal equilibrium determines $v_E = 1$ in total agreement with the dual CFT description. On the other side, in the first stages of the evolution, the presence of the apparent horizon does not affect the referred geodesics. The time after which the horizon governs the shape of the geodesic is of the order of the thermalization scale found for quark-gluon plasma experiments.

A different setup of AdS gravitational collapse is analysed in Chapter 5, which follows [2] and deals with Einstein gravity in asymptotically global AdS_4 space minimally coupled to a massless scalar field. Numerical solutions are found, and the interest is twofold, regarding to some details of the collapsing process and to the evolution of the holographic entanglement entropy for such solutions. These collapse scenarios are dual to equilibration processes of strongly coupled quantum systems on compact space. For some initial configurations, there are pulses of energy traveling through AdS and bouncing several times at the conformal boundary before collapsing to form a black hole. Accordingly, the holographic entanglement entropy oscillates, and we propose that the entanglement pattern is approximately recovered periodically as happens in out of equilibrium QFT *revivals* [91]-[94].

Numerical simulations concerning (non) equilibration processes of closed systems have been performed ever since the very dawn of computation. Indeed, the seminal work that marks the start of this era was developed in 1953 by Fermi, Pasta, Ulam and Tsingou in order to study one of such systems. They considered the evolution after perturbations of a classical closed system with different non linear interactions (one dimensional anharmonic chain with quadratic and cubic couplings) [63]. Confirming Ulam's expectations after having performed the first *numerical experiment* ever [64], nowadays computation is widely assumed to be one of the three pillars that sustain scientific progress (together with theory and experiment), and in fact this essay is yet another modest step forward within this discipline.

The main results of the FPUT work were that, contrary to what would have been expected on the grounds of statistical mechanics, non linearities are not enough to gener-

ically produce an ergodic behavior consistent with thermalization, since there exist quasi periodic solutions for which the distribution of energy is far from equipartition. This is known as the FPU paradox. Although the importance of this result was initially underestimated in terms of numerical errors, later attempts to explain the paradox have made emerge new subjects such as integrability and dynamical (classical) chaos. According to integrability, the observed quasi periodic solutions were explained by the closeness of the system to an integrable one and the necessary conservation of the integrals of motion [65]. On the other hand, within chaos theory, criteria for stochasticity were found on the basis of resonance overlapping. This was applied to the FPUT model and the threshold for stochasticity was determined [66], showing that the initial conditions taken by FPUT were below it and, in effect, in a regime of quasi periodic motion.

In the quantum realm the process of thermalization is yet much less clear even at the theoretical level, and quantum thermalization is still not well understood. From the experimental data, mounting evidence points towards a rich variety of evolutions, depending on the microscopic dynamics as well as on the initial conditions, and it has been observed how a fast approach to ergodic behavior is not always realized. In some cases, like for hard core atomic interactions, integrability inhibits thermalization by freezing the momentum distribution, such that memory of the initial state is not lost [67]. In others, the system passes through a transient quasi stationary plateau at intermediate times, known as prethermalization [68][69], before thermal equilibrium is ultimately attained. Theoretical efforts have been put into trying to derive a statistical description for these quasi-stationary states by means of a Generalized Gibbs Ensemble [70]-[74]. In addition, in some cases the dephasing time can be well over the scale of oscillations in the finite system (the size divided by the speed of excitations), giving rise to several recurring partial reconstructions of the initial state [91]-[94], and to an oscillating behavior of some observables. Among other empiric milestones, a *quantum Newton's cradle* has been constructed experimentally neatly manifesting this phenomenology [67].

The model studied in Chapter 5 shows holographic situations in which non equilibrium dynamics of a closed system does not follow a fast approach to thermal behavior. A related point of view is presented in [86], where a free Dirac fermion on a circle is quenched and the subsequent evolution studied within the CFT. It is found that the initial state is reconstructed periodically in time. The conjectured holographic dual process is the successive formation and evaporation of a black hole in global AdS spacetime, which necessarily involves quantum gravity.

As mentioned above, the classical gravity limit allows for solutions in which the energy pulse moves quasi periodically in AdS bouncing against the boundary before a black hole is formed. In this dynamic spacetime, the holographic entanglement entropy oscillates before the equilibrated state is reached, and we conjecture that the entanglement pattern is approximately reconstructed several times for the dual processes in the strongly coupled field theory, and that in fact these solutions are related to the revivals appearing after a perturbation in closed system as in [91]-[94]. Moreover, generically the first emerging horizon after several bounces does not absorbe the complete pulse. After collapse the remnant energy keeps moving periodically being partially absorbed by the black hole at each period.

The study of gravitational instabilities driven by perturbations of matter fields was initiated by Choptuik, who considered spherically symmetric scalar collapse in asymptotically flat spacetimes [88]. He found the threshold that separates solutions ending up in a

black hole from which do not not, and discovered that the collapsing solutions have universal properties characterized by a power of the distance to the threshold in parameter space with a critical exponent. Similarly, in [89], the corresponding setup was posed for AdS_3 and equivalent results were found. Below the threshold there are solutions with a periodic regime in which the scalar pulse bounces back and forth radially between the origin and the boundary. The pressure of the field (unlike null dust) fights against collapse, and in fact dominates for small enough amplitudes, while the asymptotic structure of AdS in effect implies reflecting boundary conditions. This physics is essentially the same as for spherical scalar collapse on Minkowski space-time with reflecting boundary conditions at finite radius [105].

Similar calculations were performed for AdS_4 [90], which improved technically the simulations in resolution and time as to establish that even for subcritical pulses, after a large enough number of bounces, the evolution ended up by forming an apparent horizon. A great variety of similar scenarios have been studied [95]-[104]. In [100] it was demonstrated perturbatively that there exist fully stable periodic non-linear solutions, and conjectured the existence of *islands of stability* around them in the space of initial conditions. The perturbative analysis was further supported in [101]-[103] with the explicit construction of solutions.

Given the AdS/CFT correspondence, the goal is to relate the variety of collapsing processes with the multiple relaxation processes observed in real closed quantum systems. In Chapter 5 the holographic entanglement entropy is used to try to contribute to answer this challenge.

In Chapter 6 some aspects of the gravitational turbulence that happen in the previously described AdS_4 collapses are shown to a greater extent, through the analysis of the spectrum of the scalar field and the energy. This is defined by using the basis of oscillons, the eginfunctions of the corresponding linearized problem. These functions have already been used for the perturbative constructions of [101]-[103], and also spectral decompositions of the scalar field and the energy were defined in [90][99].

The results presented in Chapter 6 are meant to highlight the importance of the selfinteraction of the scalar field energy pulse in relation to the collapse process. Localized pulses travel several times along AdS bouncing against the boundary and scattering at the origin. At the point of maximal implosion, nonlinear interactions driven by the coupling to gravity are enhanced and the energy is transferred to higher modes, notably more than during the rest of the evolution. This stepwise transfer of energy to higher modes coinciding with shocks at the origin is not observed for spread distributions of energy, for which non linear interactions happen continuously and, in this same way, the excitation of higher modes takes place.

These results reflect the main characteristic of turbulence, which is that the energy flows from bigger to smaller distances. In fluid mechanics, turbulence is due to a competition between inertial forces and viscosity, and the imprint is the appearance of eddies down to a minimal scale known as the Kolmogorov microscale [106], where viscosity dominates over inertia. Einstein equations coupled to a scalar field in AdS show an analogue phenomenon. The competition occurs between gravitational interaction and the pressure of the scalar field. A limiting small scale at which the phenomenon stops happening is determined by the appearance of a trapped surface, unavoidable in gravity when the energy focuses on smaller and smaller regions.

The chapters summarized in these paragraphs are contained in the second block in which this work is organized. In addition, the first block contains two introductory chapters which review some of the topics of quantum field theory and holography that define the theoretical frame in which the rest of the work is developed and justifies the conclusions reached. First, the entanglement entropy and quantum quenches are introduced, and then a brief introduction to the AdS/CFT correspondence and the holographic entanglement entropy is presented, showing also how it is explicitly computed and describing some of the methods used in the next chapters. Finally, conclusions are brought together and summarized.

Motivación y Resumen

La física ha tenido éxito desde hace mucho tiempo describiendo satisfactoriamente sistemas cuánticos con muchos grados de libertad en interacción en equilibrio, pero solo recientemente se han dado significativos pasos adelante para entender sistemas similares también fuera del equilibrio. En los últimos años se han producido importantes avances en experimentos de distintas áreas, como redes ópticas, átomos súper fríos y colisiones de iones pesados, mientras que la teoría ha progresado para entender estos fenómenos no solo en los campos especı'ficos de la fśica de la materia condensada, sino también en gravitación y fśica de altas energías a través de las aplicaciones de teorías de holografía. Este trabajo muestra algunos resultados de dinámica cuántica fuera del equilibrio que se deducen de la interpretación holográfica de soluciones de gravedad en dos construcciones particulares.

El marco es la correspondencia AdS/CFT, que ya ha demostrado ser útil en la descripción de teorías de campos en acoplo fuerte. Ya desde la conjetura de Maldacena a finales del siglo pasado [6] se han estudiado holográficamente las propiedades termodinámicas de sitemas cuánticos. En particular, la fase deconfinada de teorías de campos en acoplo fuerte en equilibrio termodinámico corresponde con un agujero negro en espacio asintóticamente AdS [9]. Desviaciones pequeñas fuera del equilibrio, que se decriben en términos de teoría lineal de respuesta, también han sido interpretadas holográficamente. En especial, el límite hidrodinḿico de onda larga se ha entendido bien [15]. En este contexto ha aparecido la correspondencia fluido/gravedad [18]. Uno de sus mayores éxitos ha sido la descripción de plasmas holográficos, que se comportan de forma muy parecida a fuidos perfectos (con viscosidad especfica muy baja) [16] y remarcablemente reproducen los datos experimentales de colisiones de iones pesados. Es más, la dinámica de fluidos en regímenes no lineales también ha sido bien entendida holográficamente [17][18].

En esta ruta de trabajo se han construido aún más escenarios holográficos para describir teorías de campos en acoplo fuerte fuera del equilibrio. Genéricamente se asume que un sistema macroscópico que es llevado a un estado altamente excitado evolucionará hacia un estado análogo al equilibrio térmico, en el sentido en que observables macrocópicos tomarán valores térmicos. Se ha propuesto que la descripción holográfica de tal proceso corresponde a un proceso de colapso gravitatorio (es decir, la formación de un agujero negro) [42][47][48]. Usando holografía se han estudiado la evolución fuera del equilibrio de un plasma anisótropo [49] y de un plasma invariante bajo boosts [50][51]. En [52] se estudió la evolución de un campo escalar sin masa mínimamente acoplado en el límite de amplitud pequeña, y ya se señaló cómo observables no locales de la teoría de campos en acoplo fuerte, como los Wilson loops y funciones a dos puntos, podrían proporcionar información importante sobre el proceso de termalización, no contenida en las más simples funciones a un punto. Sin embargo, estos artículos solo consideraron observables extraídos de una expansión del espacio gravitatorio dual cerca de la frontera, en especial la función a un punto del tensor energía-momento.

En paralelo se descubrían nuevas entradas del diccionario holográfico. En particular, a un observable no local en la teoría cuántica de campos, la entropía de entrelazamiento, se le hizo corresponder una cantidad geométrica de la variedad del espaciotiempo dual [3]. La entropía de entrelazamiento mide el entrelazamiento cuántico entre un subsistema y su complemento en un instante dado, y se determina calculando la entropía de Von Neumann de la matriz densidad reducida ρ de ese subsistema. La entropía de entrelazamiento ha demostrado ser útil para seguir la evolución fuera del equilibrio, pues el entrelazamiento entre grados de libertad en distintos puntos se ve modificado por perturbaciones del sis-

tema. Holográficamente, la entropía de entrelazamiento es proporcional al área propia de la superficie extrema γ que acaba en la frontera del subsistema dual en la frontera conforme del espacio AdS [3][4]. Explícitamente, la identificación holográfica para la entropía de entrelazamiento S del subsistema A es:

$$S_A = -\mathrm{Tr}_A \left(\rho_A \log \rho_A\right) = \frac{\mathrm{Area}(\gamma_A)}{4G_N} \tag{1.2}$$

En general, según la correspondencia AdS/CFT, un estado cuántico está relacionado globalmente con una solución de gravedad. La parte asintótica y la parte profunda en el interior del espaciotiempo AdS están asociadas con los regímenes UV e IR de la teoría de campos dual, respectivamente. La identificación precisa de grados de libertad locales de la teoría cuántica de campos con regiones concretas del espaciotiempo dual todavía no se conoce. Sin embargo, la Ecuación (1.2) proporciona algo más de información y relaciona el estado de un subsistema, tal y como se describe por la estropea de entrelazamiento, con una superficie específica en la geometría AdS dual.

La evolución de la entropía de entrelazamiento holográfica en un espaciotiempo dinámico que contiene la formación de agujero negro fue estudiada explícitamente en [1], confirmando los resultados conocidos de la teoría de campos conforme de 2 dimensiones dual. Una variedad de modelos de *termalización holográfica* ha aparecido desde entonces, a través del estudio de la entropía de entrelazamiento holográfica y otras cantidades geométricas en distintos escenarios de colapso en espacios asintóticamente AdS [79]-[84].

Los resultados de [1] se vuelven a exponer en el Capítulo 4. Se considera un espaciotiempo AdS Vaidya de tres dimensiones, que representa el colapso de una capa de polvo nulo o radiación incoherente en AdS. Como se muestra, este modelo es dual a un quench cuántico, la evolución dinámica fuera del equilibrio de un sistema cuántico después de un cambio brusco en uno de los parámetros del hamiltoniano. Se ha visto cómo la simetría conforme encorseta la dinámica de los quenches cuánticos en una TCC (Teoría de Campos Conforme) [5]. Además, los quenches cuánticos se pueden realizar experimentalmente en sistemas de átomos fríos junto con una posterior evolución temporal con disipación despreciable. La fenomenología está caracterizada especialmente por la aparición de termalización efectiva con un efecto horizonte. Esto es, la termalización solo se observa al nivel local en regiones de tamaño mayor según el tiempo es mayor. Este fenómeno es debido a la interacción causal de correlaciones cuánticas en el sistema, que sucede a una velocidad finita v_E. Los observables macroscópicos para sistemas equilibrados son equivalentes a los que se obtienen para los correspondientes sistemas en equilibrio térmico a una temperatura relacionada con la energía suministrada por la perturbación.

El modelo de Vaidya y un quench cuántico difieren solo en el tipo de perturbación que determina el perfil inicial de entrelazamiento y que lanza la evolución temporal. Mientras que para los sistemas considerados en los quenches cuánticos de [5] el entrelazamiento está inicialmente localizado en escalas muy pequeñas, en los sistemas quencheados que son duales al espaciotiempo de Vaidya hay correlaciones de largo alcance en el estado inicial. Teniendo esto en cuenta, las mismas conclusiones sobre la evolución de la entropía de entrelazamiento en TCC de dos dimensiones se encuentran en el modelo gravitatorio. Además, de acuerdo con la propuesta holográfica, se muestra que la evolución es manifiestamente unitaria y el sistema siempre permanece en un estado puro.

Dado el papel esencial que el horizonte de eventos juega en la descripción termodinámica de un agujero negro y por tanto en el estado térmico dual, surge la cuestión

de si conceptos generalizados de horizonte [19][20] pueden ser relevantes en la descripción holográfica de una teoría cuántica de campos lejos del equilibrio. En este caso, para el espaciotiempo dual, el horizonte aparente es un objeto local que señala la formación de una singularidad, y es más apropiado que el horizonte de eventos, que depende de la estructura causal global. Mientras que para un agujero negro estático las geodésicas relevantes para el cálculo de la entropía de entrelazamiento holográfica no cruzan el horizonte de eventos, éste junto con el horizonte aparente sí que son atravesados por las geodésicas correspondientes en el modelo de Vaidya. Los resultados holográficos muestran cómo estas geodésicas describen subsistemas en la teoría de campos dual después de la perturbación, y su porción dentro del horizonte genera una contribución a la entropía de entrelazamiento holográfica que crece linealmente con el tiempo. Esto vendrá a ser la contraparte holográfica del equilibrio local observado en las dinámicas duales de quench en la TCC. La relación de la pendiente del crecimiento lineal y la pendiente de la parte extensiva de la entropía de entanglement para el equilibrio térmico determina $v_E = 1$, en total acuerdo con la descripción dual de la TCC. El tiempo tras el cual el horizonte rige la forma de las geodésicas es del orden de la escala de termalización encontrada en experimentos con plasma de quarks-gluones.

En el Capítulo 5 se analiza un planteamiento distinto de colapso gravitatorio en AdS, que sigue [2], tratando con gravedad de Einstein en espacio asintóticamente AdS_4 global mínimamente acoplada a un campo escalar sin masa. Se encuentran soluciones numéricas, y el interés es doble, apuntando a algunos detalles del proceso de colapso y a la evolución de la entropía de entrelazamiento holográfica para esas soluciones. Estos escenarios de colapso son duales a procesos de equilibrio de sistemas cuánticos en acoplo fuerte en espacio compacto. Para algunas configuraciones iniciales aparecen pulsos de energía viajando a través de AdS y rebotando varias veces en la frontera conforme antes de colapsar para formar un agujero negro. De acuerdo con esto, la entropía de entrelazamiento holográfica oscila, y proponemos que el perfil de entrelazamiento se recupera aproximadamente varias veces periódicamente, como sucede en los *revivals* de teoría cuántica de campos fuera del equilibrio [91]-[94].

Desde los mismos albores de la computación se han llevado a cabo simulaciones numéricas sobre procesos de (no) llegada al equilibrio de sistemas cerrados. Ciertamente, el trabajo inicial que marca el arranque de esta era fue desarrollado en 1953 por Fermi, Pasta, Ulam and Tsingou con el objetivo de uno de esos sistemas. Consideraron la evolución después de perturbaciones de un sistema clásico cerrado con distintas interacciones no lineales (una cadena anarmónica unidimensional con acoplos cuadráticos y cúbicos) [63]. Confirmándose los pronósticos de Ulam después de haber llevado a cabo el primer *experimento numérico* de la historia, hoy en día está asumido ampliamente que la computación es uno de los tres pilares que sustentan el progreso científico (junto con la teoría y el experimento), y de hecho este trabajo es un modesto paso más en esta disciplina.

Los principales resultados del modelo FPUT fueron que, al contrario de lo que se habría esperado sobre las bases de la mecánica estadística, las no linealidades no son suficientes como para que se produzca genéricamente un comportamiento ergódico consistente con termalización, pues existen soluciones cuasiperiódicas para las cuales la distribución de energía está lejos de la equipartición. Esto se conoce como la paradoja FPU.

Si bien la importancia de este resultado fue inicialmente subestimada en términos de errores numéricos, posteriores propuestas para explicar la paradoja han hecho emerger nuevos campos como la integrabilidad y el caos (clásico) dinámico. Según integrabilidad,

las soluciones cuasiperiódicas que se observaron se explicaban porque el sistema en consideración era cercano a uno integrable y por la conservación necesaria de las constantes del movimiento [65]. Por otro lado, dentro de teoría del caos se encontraron criterios para el comportamiento estocástico basándose en solapamiento de resonancias. Esto se aplicó al modelo de FPUT y se determinó el umbral de estocasticidad [66], mostrando que las condiciones iniciales tomadas por FPUT estaban por debajo y, de hecho, en el régimen de movimiento cuasiperiódico.

En los dominios cuánticos el proceso de termalización está todavía mucho menos claro incluso al nivel teórico, y la termalización cuántica todavía no se entiende bien. Los experimentos evidencian la existencia de una rica variedad de evoluciones dependiendo de la dinámica microscópica así como de las condiciones iniciales, y se ha observado cómo no siempre se da una rápida llegada al comportamiento ergódico. En algunos casos, como para interacciones atómicas de núcleos duros, la integrabilidad inhibe la termalización al congelar la distribución de momentos, de forma que no se pierde la memoria del estado inicial [67]. En otros, el sistema atraviesa transitoriamente un plateau cuasi estacionario a tiempos intermedios, conocido como pretermalización [68][69], antes de que al final se alcance el equilibrio térmico. Se han hecho esfuerzos en el campo teórico para intentar dar una descripción estadística para estos estados cuasiestacionarios por medio de Colectivos de Gibbs Generalizados [70]-[74]. Además, en algunos casos el tiempo de desfase puede estar bien por encima de la escala de oscilaciones del sistema finito (el tamaño dividido por la velocidad de las excitaciones), dando lugar a varias reconstrucciones parciales recurrentes del estado inicial [91]-[94], y a un comportamiento oscilatorio de algunos observables. Entre otros hitos empíricos, un *péndulo de Newton cuántico* se ha construido experimentalmente, manifestando claramente esta fenomenología [67].

El modelo estudiado en el Capítulo 5 muestra situaciones holográficas en las que la dinámica fuera del equiibrio de un sistema cerrado no alcanza rápidamente el equilibrio térmico. En [86] se presenta un punto de vista relacionado. Se estudia en TCC la evolución después de un quench de un fermión de Dirac libre y se encuentra que el estado inicial se reconstruye periódicamente en el tiempo. Se conjetura que el proceso holográfico dual es la sucesiva formación y evaporación de un agujero negro en espaciotiempo AdS global, lo cual necesariamente involucra gravedad cuántica.

Como se muestra más adelante en detalle, en el límite de gravedad clásica se encuentran soluciones en las que el pulso de energía se mueve cuasiperiódicamente en AdS, rebotando contra la frontera antes de que se forme un agujero negro. En este espaciotiempo dinámico, la entropía de entrelazamiento holográfica oscila antes de que se alcance el estado de equilibrio, y conjeturamos que el perfil de entrelazamiento se reconstruye varias veces para el proceso dual en la teoría de campos en acoplo fuerte, y que de hecho estas soluciones están relacionadas con los revivals que aparecen después de una perturbación en sistemas cerrados, como en [91]-[94]. Es más, genéricamente el primer horizonte que emerge después de varios rebotes no absorbe completamente el pulso. Después del colapso la energía remanente se sigue moviendo periódicamente siendo absorbida parcialmente por el agujero negro en cada periodo.

El estudio de inestabilidades gravitatorias producidas por perturbaciones de campos de materia fue iniciado por Choptuik, quien consideró colapso escalar con simetría esférica en espacio asintóticamente plano [88]. Encontró el umbral que separa las soluciones que terminan formando un black hole de las que no, y descubrió que las soluciones con colapso tienen propiedades universales caracterizadas por una potencia de la distancia al valor

del umbral en el espacio de parámetros con un exponente crítico. De manera parecida, en [89] se estudió el planteamiento correspondiente para AdS_3, y se encontraron resultados equivalentes. Por debajo del umbral hay soluciones con un régimen periódico en el que el pulso escalar rebota de una y otra vez radialmente entre el origen y la frontera. La presión del campo (al contrario que el polvo nulo) lucha contra el colapso, y de hecho domina para amplitudes suficientemente pequeñas, mientras que la estructura asintótica de AdS implica en efecto condiciones de contorno reflectantes. La física es esencialmente la misma que para colapso escalar esféricamente simétrico en espacio de Minkowski con condiciones de contorno reflectantes en un radio finito [105].

En [90] se realizaron cálculos parecidos en AdS_4, mejorando técnicamente las simulaciones en resolución y tiempo como para establecer que, incluso para pulsos subcríticos, después de un número de rebotes suficientemente largo la evolución terminaba formando un horizonte aparente. Se ha estudiado una gran variedad de escenarios parecidos [95]-[104]. En [100] se demostró perturbativamente que existen soluciones no lineales completamente estables, y se conjeturó la existencia de *islas de estabilidad* alrededor de ellas en el espacio de condiciones iniciales. El análisis perturbativo fue posteriormente apoyado por [101]-[103] con la construcción explícita de soluciones.

Dada la correspondencia AdS/CFT, el objetivo es relacionar la variedad de procesos de colapso con los múltiples procesos de relajación observados en sistemas cuánticos cerrados reales. En el Capítulo 5 se utiliza la entropía de entanglement holográfica para intentar contribuir con una respuesta a este desafío.

En el Capítulo 6 se muestran en más profundidad algunos aspectos de la turbulencia gravitatoria que sucede en los procesos de colapso en AdS_4 descritos previamente, a través del análisis del espectro del campo escalar y la energía. Se define usando la base de oscilones, las autofunciones del problema linealizado. Ya se han utilizado estas funciones para las construcciones perturbativas de [101]-[103], y también en [90][99] se definieron descomposiciones espectrales del campo escalar y de la energía.

El objetivo de l os resultados del Capítulo 6 es mostrar la importancia de la autointeracción del pulso de energía del campo escalar en relación al proceso de colapso. Los pulsos localizados viajan varias veces a través de AdS rebotando contra la frontera y dispersándose en el origen. En el punto de máxima implosión se potencian las interacciones no lineales que se producen a través de gravedad, y la energía se transfiere a modos más altos, notablemente más que durante el resto de la evolución. Esta transferencia escalonada de energía a modos más altos coincidiendo con los choques en el origen no se observa para distribuciones de energía esparcidas, para las que las interacciones no lineales suceden continuamente, y de esta misma forma sucede la excitación de modos más altos.

Estos resultados reflejan la principal característica de la turbulencia, y es que la energía fluye de distancias más grandes a más pequeñas. En mecánica de fluidos la turbulencia es debida a una competición entre fuerzas de inercia y viscosidad, y la marca es la aparición de remolinos hasta una escala mínima conocida como la micro escala de Kolmogorov [106], para la cual la viscosidad domina sobre la inercia. Las ecuaciones de Einstein acopladas a un campo escalar en AdS muestran un fenómeno análogo. La competición ocurre entre la interacción gravitatoria y la presión del campo escalar. Una escala limitante mínima a la cual el fenómeno deja de ocurrir queda determinada por la aparición de una superficie atrapada, inevitable en gravedad cuando la energía se concentra en regiones más y más pequeñas.

Los capítulos que se han resumido en estos párrafos están contenidos en el segundo bloque en el que este trabajo está organizado. Además, el primer bloque incluye dos capítulos introductorios que repasan algunos de los temas de teoría cuántica de campos y holografía que definen el marco teórico en el que se desarrolla el resto del trabajo y que justifican las conclusiones que se alcanzan. Primero, se introducen la entropía de entrelazamiento y los quenches cuánticos, y después se da una breve introducción a la correspondencia AdS/CFT y se presenta la entropía de entrelazamiento holográfica, mostrando también explícitamente cómo calcularla y describiendo algunos de los métodos usados en los siguientes capítulos. Finalmente, se reúnen y resumen las conclusiones.

Part I

Foundations

2 Quantum Basics

In this introductory chapter we review some aspects related to quantum physics that are relevant for this work. In particular, the entanglement entropy and the quantum quenches are the main topics.

2.1 Entanglement Entropy (EE)

2.1.1 Quantum Entanglement

A quantum system that posseses entanglement is a composite system that requires to be described in its entirety, as it is not possible to fully describe a component of the system without considering the others. Formally, let the total Hilbert space of a quantum system be expressed as the direct product of other Hilbert spaces:

$$\mathcal{H} = \mathcal{H}_A \otimes \mathcal{H}_B \otimes ... \tag{2.1}$$

An entangled state cannot be expressed as a direct product of states from the subsystem spaces. It is pure in the total Hilbert space but it is not possible to associate any subsystem with a definite pure state in its corresponding Hilbert space. An entangled state is then expressed as a linear superposition of direct products of states from the subsystem spaces. For a two-component system, $\mathcal{H} = \mathcal{H}_A \otimes \mathcal{H}_B$, it is written:

$$|\Psi\rangle = |\phi_1\rangle_A \otimes |\phi_2\rangle_B + |\phi_3\rangle_A \otimes |\phi_4\rangle_B + ... \tag{2.2}$$

For a non entangled state, measurements on a subsystem do not affect the other. A non entangled state is a tensor product of states of the individual subspaces:

$$|\Psi\rangle = |\phi_1\rangle_A \otimes |\phi_2\rangle_B \tag{2.3}$$

Let us introduce the density matrix ρ. It is useful for describing the total system when it is in a pure state $|\Psi\rangle$,

$$\rho = |\Psi\rangle\langle\Psi|, \tag{2.4}$$

as well as for statistically mixed states. In these cases, if the state $|\Psi_j\rangle$ has a statistical probability p_j, the density matrix is defined as

$$\rho = \sum_j p_j |\Psi_j\rangle\langle\Psi_j| \tag{2.5}$$

For a thermal equilibrium ensemble, in which the p_j are given by the Boltzmann distribution, the associated density matrix, for an inverse temperature β and a hamiltonian H, is

$$\rho_{\text{th}} = e^{-\beta H} \tag{2.6}$$

The density matrix is definite positive and conveniently normalized to trace 1, such that the expectation value of any observable $\mathcal{O}$ is computed by $\langle \mathcal{O} \rangle = \text{Tr}(\rho \mathcal{O})$.

We also define the reduced density matrix ρ_A, corresponding to the subsystem A, as the effective density matrix seen by an observer restricted to A, or, equivalently, who has no access to its complement $\bar{A}$. Hence, it is built out of ρ by tracing over the degrees of freedom of $\bar{A}$:

$$\rho_A = \text{Tr}_{\bar{A}} \rho = \sum_j \langle \phi_j^{\bar{A}} | \rho | \phi_j^{\bar{A}} \rangle \tag{2.7}$$

Where $\{|\phi_j^{\bar{A}}\rangle\}$ is a complete basis of $\mathcal{H}_{\bar{A}}$.

The degree of entanglement among different subsystems is encoded in the reduced density matrices. A maximally entangled state is that for which the reduced density matrix associated to any subsystem is proportional to the identity. This implies that a measure on that subsystem is random, as every possible outcome is equally probable, and therefore that only measure can give no information about the total state.

For example, for two spin-1/2 particles, the total state space is the tensor product of the individual spaces of the two particles, and there are four maximally entangled states, known as Bell states, for which $\rho_A = \frac{1}{2}\text{diag}(1,1)$. An instance of them is $\frac{1}{\sqrt{2}}(|00\rangle + |11\rangle)$.

2.1.2 Definition and Properties of the Entanglement Entropy

The Entanglement Entropy (EE) is a measure of entanglement. The EE assigned to the subsystem A is defined as the Von Neumann entropy of its reduced density matrix ρ_A:

$$S_A = -\text{Tr}_A (\rho_A \log \rho_A) \tag{2.8}$$

In many cases in QFT the reduced density matrix is not easily obtainable, and the definition (2.8) is not of much use. However, there are methods for obtaining the quantity $\text{Tr}\rho_A^n$, with n integer. One can show that the EE can be computed by analytically extending n and taking the limit

$$S_A = -\lim_{n \to 1} \frac{\partial}{\partial n} \text{Tr} \rho_A^n \tag{2.9}$$

Properties of EE:

- When the system is in a pure state, the EE evaluated of any two complementary subsystems, A and $\bar{A}$, are the same:

$$S_A = S_{\bar{A}} \tag{2.10}$$

- The EE of the complete system is zero.
- Subadditivity: For any two subsystems A_1 and A_2:

$$S_{A_1 \cup A_2} \leq S_{A_1} + S_{A_2} \tag{2.11}$$

- Strong subadditivity: This is a stronger condition:

$$S_{A_1} + S_{A_2} \geq S_{A_1 \cup A_2} + S_{A_1 \cap A_2} \tag{2.12}$$

Also, for any three subsystems (A_1, A_2, A_3), with empty intersections among them, the strong subadditivity reads:

$$S_{A_1 \cup A_2 \cup A_3} + S_{A_2} \leq S_{A_1 \cup A_2} + S_{A_2 \cup A_3} \tag{2.13}$$

- Divergence and Area Law:

Let the quantum theory under consideration be regulated with an ultraviolet cutoff a and defined on a manifold with d spatial dimensions. The leading term of the EE of the system A, for $d \geq 2$, generically has the form [22][23] :

$$S_A = C \, \frac{\text{Area}(\partial A)}{a^{d-1}} + ... \tag{2.14}$$

Where C is a constant that depends on the particular system and ∂A is the boundary of A. In the continuum limit $a \to 0$ the EE diverges as the inverse power of a to the dimensionality of the boundary ∂A of the subsystem. The physical interpretation stands in that the entanglement between degrees of freedom defined on nearby points is stronger than that between degrees of freedom on separated points. Thus, the entanglement between A and its complement is dominated by contributions coming from the boundary.

For linear systems, $d = 1$, the boundary is of zero measure. The divergence in this case is logarithmic: $S_A = \frac{c}{3} \log \frac{\ell}{a}$, where ℓ is the length of the system. We shall prove this result below in section 2.1.3.

The validity of (2.14) is not completely general for any QFT. Explicit violations of the area law have been found for fermionic systems [24][25]. In these cases (2.14) is corrected with a logarithmic term:

$$S_A \sim \left(\frac{\ell}{a}\right)^{d-1} \log(k_F \ell) \tag{2.15}$$

Where k_F is the momentum associated to the Fermi surface.

The field theories studied in this work obey the are law (2.14).

- (Non) Extensivity and Thermal Equilibrium:

The EE is not in general an extensive quantity. When it is, the EE coincides with the thermal entropy. In a thermal equilibrium state, for subsystems with a length scale bigger than the inverse temperature β, the EE is dominated by statistical thermal correlations, and tends to be extensive and to coincide with the thermal entropy. The strict equality is attained in the limit in which A is the whole system. Conversely, if the typical length scale of the subsystem is well below the inverse temperature, thermal excitations cannot fit in the subsystem, and the EE corresponds to that of the vacuum state:

$$S_A \approx S_A^{\text{vac}} \quad , \quad \text{if} \;\; \text{size}(A) \ll \beta \tag{2.16}$$

$$S_A \approx S_A^{\text{therm}} \quad , \quad \text{if} \;\; \text{size}(A) \gg \beta \tag{2.17}$$

Below, in section 2.1.5, the explicit simple example of an interval at thermal equilibrium in a CFT_{1+1} clearly shows this behaviour.

2.1.3 Entanglement Entropy in QFT. The Replica Trick.

Here we describe the standard method to compute EE in quantum field theory. Actually the aim is to calculate $\mathrm{Tr}\rho_A^n$ through the so called *replica trick*. This was initiated in [26] and systematized in [27], [28]. For definiteness let us consider a QFT in 1+1 dimensions, defined on the complex plane with Euclidean time, (x, t_E). At $t_E = 0$, for the field configuration $\phi_0(x)$, the ground state wave function Ψ and its conjugate are:

$$\Psi(\phi_0(x)) = \int_{\phi(t_E=-\infty,x)=\phi_{\mathrm{in}}(x)}^{\phi(t_E=0,x)=\phi_0(x)} \mathcal{D}\phi\ e^{-S[\phi]} \tag{2.18}$$

$$\bar{\Psi}(\phi_0(x)) = \int_{\phi(t_E=0,x)=\phi_0(x)}^{\phi(t_E=\infty,x)=\phi_{\mathrm{out}}(x)} \mathcal{D}\phi\ e^{-S[\phi]} \tag{2.19}$$

The elements of the corresponding density matrix are then

$$\langle\phi_0|\rho|\phi_0'\rangle = (Z_1)^{-1}\Psi(\phi_0(x))\bar{\Psi}(\phi_0'(x)) \tag{2.20}$$

Where Z_1 is the partition function that links the ϕ_{in} and ϕ_{out} configurations and has been introduced for a correct normalization of ρ.

2.1.4 Single Interval

Let us consider from now on that the subsystem A is an interval of length ℓ between the points u and v:

$$A = \{x \mid u \leq x \leq v\} \tag{2.21}$$

In order to get the reduced density matrix ρ_A in A we need to trace over the degrees of freedom in its complement region $\bar{A}$. This means to assume the same field configuration at $t_E = 0$ for all $x \in \bar{A}$. Then, the path integral may be expressed as:

$$\langle\phi_0|\rho_A|\phi_0'\rangle = \frac{1}{Z_1}\int_{\phi(t_E=-\infty,x)=\phi_{\mathrm{in}}(x)}^{\phi(t_E=\infty,x)=\phi_{\mathrm{out}}(x)} \mathcal{D}\phi\, e^{-S[\phi]}\left[\delta(\phi(0^+,x)-\phi_0(x))\delta(\phi(0^-,x)-\phi_0'(x))\right]_{x\in A} \tag{2.22}$$

$\mathrm{Tr}\rho_A^n$ is obtained by taking together n copies and integrating over the repeated successive $n-1$ field configurations:

$$\langle\phi_0|\rho_A^n|\phi_0'\rangle = \int\left(\prod_{i=1}^{n-1}\mathcal{D}\phi_i\right)\langle\phi_0|\rho_A|\phi_1\rangle\langle\phi_1|\rho_A|\phi_2\rangle...\langle\phi_{n-1}|\rho_A|\phi_0'\rangle \tag{2.23}$$

We use (2.22) $n-1$ times in the integrand of (2.23) and, then, $\mathrm{Tr}\rho_A^n$ is computed by identifying and integrating over the unpaired field configurations ϕ_0 and ϕ_0'. Altogether, the operations of taking the n-th power and the trace correspond to

$$Z_{\mathcal{M}_n} = \int(\mathcal{D}\phi)_{\mathcal{M}_n}\ e^{-\int_{\mathcal{M}_n} d^2x\mathcal{L}[\phi]} \tag{2.24}$$

This represents a path integral in an n-sheeted manifold $\mathcal{M}_n$, which consists in n copies of the original complex plane with successive identifications of the field configurations. With this, we can write

$$\mathrm{Tr}\rho_A^n = \frac{Z_{\mathcal{M}_n}}{Z_1^n} \tag{2.25}$$

In order to evaluate the path integral $Z_{\mathcal{M}_n}$, it is convenient to introduce n replicated fields: $\phi \to \{\phi_k\}_{k=1}^n$, such that $Z_{\mathcal{M}_n}$ can be written as the following integral in the simple complex plane:

$$\int_{\mathbb{C}} \left(\prod_{k=1}^{n} \mathcal{D}\phi_k \right) e^{-\int_{\mathbb{C}} d^2x \sum_{k=1}^{n} \mathcal{L}[\phi_k]} \tag{2.26}$$

For this to hold, the replicated fields need to be connected through twist boundary conditions that can be defined associated to rotations around the interval endpoints u and v. Defining $z = x + it_E$, these conditions read

$$\mathcal{C}_u^{(n)} : \quad \phi_k(e^{2\pi i}(z-u)) = \phi_{k+1}(z-u) \quad , \; k = 1...n-1 \tag{2.27}$$

$$\mathcal{C}_v^{(-n)} : \quad \phi_{k+1}(e^{2\pi i}(z-v)) = \phi_k(z-v) \quad , \; k = 1...n-1 \tag{2.28}$$

These imply a branch cut supported on A, such that any field crossing the x-axis at $x < u$ does not feel any twist and propagates in the same sheet. A field crossing the x-axis at $u < x < v$ is affected by the condition on u and jumps up to another copy, and fields crossing the x-axis at $x > v$ suffer both twists and keep propagating in the same copy. Implementing these conditions, we may write:

$$Z_{\mathcal{M}_n} = \int_{\mathbb{C}, \{\mathcal{C}_u^{(n)}, \mathcal{C}_v^{(-n)}\}} \left(\prod_{k=1}^{n} \mathcal{D}\phi_k \right) e^{-\int_{\mathbb{C}} d^2x \sum_{k=1}^{n} \mathcal{L}[\phi_k]} \tag{2.29}$$

The path integral $Z_{\mathcal{M}_n}$, being originally defined in (2.24) as the original theory on a replicated manifold $\mathcal{M}_n$, is expressed in (2.29) as a collection of replicas of the theory on $\mathbb{C}$ with a branch cut on A and the twist conditions (2.27)-(2.27).

The last obstacle is the explicit inclusion of such conditions $\mathcal{C}_u^{(n)}$ and $\mathcal{C}_v^{(-n)}$ in the path integral. This can be saved by taking into account that it is possible to associate a local primary field to any branch point as u and v. In particular, associated to $\mathcal{C}_u^{(n)}$ and $\mathcal{C}_v^{(-n)}$ as defined in (2.27)-(2.28), there exist twist fields $\mathcal{T}_n$ and $\tilde{\mathcal{T}}_n$, whose insertion into the path integral implements the corresponding twist conditions (2.27)-(2.28) [27]. They are formally defined by:

$$\int \left(\prod_{k=1}^{n} \mathcal{D}\phi_k \right) \mathcal{T}_n(u)\mathcal{O}(z) \equiv \int_{\mathcal{C}_u^{(n)}} \left(\prod_{k=1}^{n} \mathcal{D}\phi_k \right) \mathcal{O}(z) \tag{2.30}$$

$$\int \left(\prod_{k=1}^{n} \mathcal{D}\phi_k \right) \tilde{\mathcal{T}}_n(v)\mathcal{O}(z) \equiv \int_{\mathcal{C}_v^{(-n)}} \left(\prod_{k=1}^{n} \mathcal{D}\phi_k \right) \mathcal{O}(z) \tag{2.31}$$

Then, introducing the twist fields in (2.29), we obtain

$$\mathrm{Tr}\rho_A^n = \frac{1}{Z_1^n} Z_{\mathcal{M}_n} = \frac{1}{Z_1^n} \int_{\mathbb{C}} \left(\prod_{k=1}^{n} \mathcal{D}\phi_k \right) \mathcal{T}_n(u)\tilde{\mathcal{T}}_n(v) e^{-\sum_{k=1}^{n} S[\phi_k]} = \langle \mathcal{T}_n(u)\tilde{\mathcal{T}}_n(v) \rangle_{\mathbb{C}} \tag{2.32}$$

The computation of the reduced density matrix has been converted to the calculation of a two point function of primary operators. As in a CFT correlation functions depend only on the conformal dimension of the inserted operators (apart from an overall factor), we only need to know what the conformal dimension of the twist field $\mathcal{T}_n$ is.

For this, we first note that the two point function is fixed, up to normalization, by conformal invariance [32]:

$$\langle \mathcal{T}_n(u,0)\tilde{\mathcal{T}}_n(v,0)\rangle_{\mathbb{C}} = \frac{1}{|u-v|^{2d_n}} \tag{2.33}$$

Where d_n is the conformal dimension of the twist operators. The conformal Ward identity [32] for the two point function (2.33) will be useful:

$$\begin{aligned}\langle \mathcal{T}_n(u,0)\tilde{\mathcal{T}}_n(v,0)T(w)\rangle_{\mathbb{C}} = \\ \left(\frac{1}{w-u}\frac{\partial}{\partial u} + \frac{d_n}{(w-u)^2} + \frac{1}{w-v}\frac{\partial}{\partial v} + \frac{\bar{d}_n}{(w-v)^2}\right)\langle \mathcal{T}_n(u,0)\tilde{\mathcal{T}}_n(v,0)\rangle_{\mathbb{C}},\end{aligned} \tag{2.34}$$

The stress tensor in $\langle \mathcal{T}_n(u,0)\tilde{\mathcal{T}}_n(v,0)T(w)\rangle_{\mathbb{C}}$ is that of the replicated model, which consists in n copies, and therefore $T(w) = nT_k(w)$. Hence:

$$\frac{\langle \mathcal{T}_n(u,0)\tilde{\mathcal{T}}_n(v,0)T(w)\rangle_{\mathbb{C}}}{\langle \mathcal{T}_n(u,0)\tilde{\mathcal{T}}_n(v,0)\rangle_{\mathbb{C}}} = \frac{n\langle \mathcal{T}_n(u,0)\tilde{\mathcal{T}}_n(v,0)T_i(w)\rangle_{\mathbb{C}}}{\langle \mathcal{T}_n(u,0)\tilde{\mathcal{T}}_n(v,0)\rangle_{\mathbb{C}}} \tag{2.35}$$

The relation between expectation values in the replicated model and in $\mathcal{M}_n$ is implemented through the twist fields:

$$\langle \mathcal{O}(w;\text{sheet}j)\rangle_{\mathcal{M}_n} = \frac{\langle \mathcal{T}_n(u_1,0)\tilde{\mathcal{T}}_n(v_1,0)\mathcal{O}_j(w)\rangle_{\mathbb{C}}}{\langle \mathcal{T}_n(u_1,0)\tilde{\mathcal{T}}_n(v_1,0)\rangle_{\mathbb{C}}} \tag{2.36}$$

Then, (2.35) reduces to:

$$\frac{n\langle \mathcal{T}_n(u,0)\tilde{\mathcal{T}}_n(v,0)T_i(w)\rangle_{\mathbb{C}}}{\langle \mathcal{T}_n(u,0)\tilde{\mathcal{T}}_n(v,0)\rangle_{\mathbb{C}}} = n\langle T(w,\text{sheet } i)\rangle_{\mathcal{M}_n} \tag{2.37}$$

So we are led with the computation of the stress tensor on $\mathcal{M}_n$. To this aim we note that there is a conformal transformation relating $\mathcal{M}_n$ and $\mathbb{C}$:

$$z = \left(\frac{w-u}{w-v}\right)^{\frac{1}{n}} \tag{2.38}$$

We recall the transformation of the one point function of the stress-energy tensor [32]:

$$\langle T(w)\rangle_{\mathcal{M}_n} = \left(\frac{\partial z}{\partial w}\right)^2\langle T(z)\rangle_{\mathbb{C}} + \frac{c}{12}\{z,w\} \tag{2.39}$$

Where

$$\{z,w\} = \frac{z'''z' - 3/2z''^2}{z'^2} = \frac{c(n^2-1)}{24n^2}\frac{(u_1-v_1)^2}{(w-a_1)^2(w-a_2)^2} \tag{2.40}$$

Then, given that $\langle T(z)\rangle_{\mathbb{C}} = 0$,

$$\langle T(w)\rangle_{\mathcal{M}_n} = \frac{c(n^2-1)}{24n^2}\frac{(u_1-v_1)^2}{(w-a_1)^2(w-a_2)^2} \tag{2.41}$$

And substituting this in (2.37) we obtain

$$\frac{\langle \mathcal{T}_n(u_1,0)\tilde{\mathcal{T}}_n(v_1,0)T(w)\rangle_{\mathbb{C}}}{\langle \mathcal{T}_n(u_1,0)\tilde{\mathcal{T}}_n(v_1,0)\rangle_{\mathbb{C}}} = \frac{c(n^2-1)}{24n}\frac{(u-v)^2}{(w-u)^2(w-v)^2} \tag{2.42}$$

Finally, combining (2.42) with the Ward identity (2.34) and the general form of two point functions (2.33), we can extract the conformal dimension and get:

$$d_n = \frac{c}{12}\left(n - \frac{1}{n}\right) \tag{2.43}$$

Back to the pursued $\mathrm{Tr}\rho_A^n$ in (2.32), we have obtained:

$$\mathrm{Tr}\rho_A^n = c_n \left(\frac{v-u}{a}\right)^{-\frac{c}{6}\left(n-\frac{1}{n}\right)} \tag{2.44}$$

Where we included the undetermined two point function normalization constant c_n, as well as the parameter a, with units of E^{-1}, for the result to be dimensionally correct. This is associated to the renormalization of the two point functions [27]. In a lattice field theory a is to be identified with the lattice size and corresponds to the regulator of the intrinsic divergent of the EE, as explained in the context of the area law in (2.14).

Let the points u and v be located on the real axis separated a distance $\ell = |v-u|$. Then, derivating (2.44) using (2.9), we obtain the EE of a single interval of length ℓ for the ground state of a CFT_{1+1} on a line:

$$S_A = \frac{c}{3}\log\frac{\ell}{a} + c_1' \tag{2.45}$$

The constant c_1' is universal and is related to the c_n above.

2.1.5 Thermal Equilibrium and Compact Space

The conformal transformation

$$w \to z = \frac{B}{2\pi}\log w \tag{2.46}$$

Takes each sheet in the w-plane into an infinite cylinder with circumference length B. The density matrix computed on this manifold represents different physical situations depending on the assignment of coordinates.

Under conformal transformations, two point functions transforms covariantly [32]:

$$\langle \mathcal{T}_n(z_1,\bar{z}_1)\tilde{\mathcal{T}}_n(z_2,\bar{z}_2)\rangle = |w'(z_1)w'(z_2)|^{d_n}\langle \mathcal{T}_n(w_1,\bar{w}_1)\tilde{\mathcal{T}}_n(w_2,\bar{w}_2)\rangle \tag{2.47}$$

This is the case of $\mathrm{Tr}\rho_A^n$, as it has been previously shown.

Thermal Equilibrium State:

Partition functions defined on periodic imaginary time represent theories in a thermal equilibrium state. We assign (euclidean) time to the compact direction and make $B = \beta$ the inverse temperature. This results in an n-sheeted cylinder with branch points along the longitudinal direction. The quantity $\mathrm{Tr}\rho_A^n$ is calculated by transforming (2.44) with the logarithmic map (2.46). Then, using $S_A = -\lim_{n\to 1}\frac{\partial}{\partial n}\mathrm{Tr}\rho_A^n$, we obtain the EE:

$$S_A = \frac{c}{3}\log\left(\frac{\beta}{\pi a}\sinh\frac{\pi\ell}{\beta}\right) + c_1' \tag{2.48}$$

We can expand to find:

$$S_A \approx \frac{c}{3}\log\frac{\ell}{a} + c_1' \quad , \text{ for } \ell \ll \beta \tag{2.49}$$

$$S_A \approx \frac{\pi c}{3\beta}\ell + c_1' \quad , \text{ for } \ell \gg \beta \tag{2.50}$$

The small size limit (2.49) reproduces the vacuum entanglement (2.45), while the large size limit (2.49) is a linear function of ℓ with a slope proportional to the temperature. It is identified with thermal entropy.

Compact Space:

Alternatively, assigning the compact direction of the cylinder defined by the map (2.46) to the space coordinate allows to study the ground state of the theory on compact space of length B. One obtains for the EE:

$$S_A = \frac{c}{3}\log\left(\frac{B}{\pi a}\sin\frac{\pi\ell}{B}\right) \tag{2.51}$$

2.2 Quantum Quenches

An interesting setup for the study of the dynamics of non-equilibrium systems is that of quantum quenches [33][5][34], in which the initial state is taken as the ground state of a QFT hamiltonian that is *quenched* instantaneously through the change of some parameter like mass or coupling. The new hamiltonian is responsible for the subsequent evolution of the prepared initial state.

The study of quantum quenches dynamics corresponds to the classic quantum mechanical problem of tracking the evolution of a state $|\Psi(t)\rangle$:

$$|\Psi(t)\rangle = e^{-iHt}|\Psi(0)\rangle = \sum_j e^{-iE_j t}|\phi_j\rangle\langle\phi_j|\Psi(0)\rangle \tag{2.52}$$

Such that $|\phi_j\rangle$ and E_j are the eigenstates of the hamiltonian H and their corresponding energies respectively, and $|\Psi(0)\rangle$, is the ground state of the hamiltonian H_0, which in turn is related to H through the change of value of some parameter. However, the infinite number of local degrees of freedom present in a QFT makes this problem untractable under a Schrodinger picture approach as in (2.52).

It is interesting to know how quantum correlations change after a quench. In this section we first review correlation functions in a scalar field theory and the EE in a CFT, where conformal invariance highly constrains the evolution irrespectively of interactions. Then, we shall discuss the main phenomenology associated to quenches, and which is manifest in both examples: the horizon effect or how the perturbation produced by the quench propagates at a finite speed, and the effective thermalization or how observables look like thermal after the quench.

2.2.1 Coupled Oscillators after a Deep Quench

Let us review the instructive example of [36] and consider coupled harmonic oscillators described by the hamiltonian :

$$H = \frac{1}{2}\sum_r \pi^2(r) + \frac{1}{2}\sum_{r,r'} K(r-r')(\phi(r)-\phi(r'))^2 \tag{2.53}$$

This is actually a free field theory as can be seen by passing to momentum space:

$$H = \sum_k \left(\frac{1}{2}\pi_k\pi_{-k} + \frac{1}{2}\omega_k^2\phi_k\phi_{-k}\right) \tag{2.54}$$

Where the dispersion relation $\omega_k = \omega_k(k)$, depending on the function K above, encodes all the couplings among the oscillators. Let us consider a relativistic form

$$\omega_k^2 = k^2 + m^2 \tag{2.55}$$

This allows to describe a system with mass gap m and maximum velocity of excitations equal to 1. The quantum quench is implemented by a sudden change at $t = 0$ of the mass: $m_0 \to m$.

In a free field theory all physical observables are determined by the two point function:

$$\langle\Psi_0|T\phi(t_1,\mathbf{r}_1)\phi(t_2,\mathbf{r}_2)|\Psi_0\rangle \equiv \int \frac{d^d\mathbf{k}}{(2\pi)^d} e^{i\mathbf{k}\cdot(\mathbf{r}_1-\mathbf{r}_2)} C_{\rm q}(t_1,t_2,\omega(\mathbf{k})) \tag{2.56}$$

As the hamiltonian (2.54) consists in non-interacting harmonic oscillators of different frequencies, the propagator is expressed as the inverse Fourier transform of the propagator of a single degree of freedom with frequency ω, $C_{\rm q}(t_1,t_2,\omega)$. Let us first compute this apart, and consider a single degree of freedom $\phi(t)$ and hamiltonians H_0 and H, before and after the quench respectively.

$$H_0 = \frac{1}{2}\pi^2 + \frac{1}{2}\omega_0^2\phi^2 \tag{2.57}$$

$$H = \frac{1}{2}\pi^2 + \frac{1}{2}\omega^2\phi^2 \tag{2.58}$$

The ground state $|\Psi_0\rangle$ of H_0 is the initial state. The propagator $C_{\rm q}$ for this quenched system is

$$C_{\rm q}(t_1,t_2) \equiv \langle\Psi_0|T\phi(t_1)\phi(t_2)|\Psi_0\rangle \tag{2.59}$$

Where the evolution of the field ϕ in the Heisenberg picture is determined by the equation of motion derived from the hamiltonian after the quench, $\ddot{\phi} + \omega^2\phi = 0$. The solution is written in the form

$$\phi(t) = \phi(0)\cos(\omega t) + \frac{\pi(0)}{\omega}\sin(\omega t) \tag{2.60}$$

Using this solution and the canonical commutation relation $[\phi(0),\pi(0)] = i$, the propagator (2.59) is:

$$C_{\rm q}(t_1,t_2) = \langle\Psi_0|\phi^2(0)\Psi_0\rangle\cos\omega t_1\cos\omega t_2 + \tag{2.61}$$

$$+\langle\Psi_0|\pi^2(0)\Psi_0\rangle\frac{1}{\omega^2}\sin\omega t_1\sin\omega t_2 + \tag{2.62}$$

$$+\langle\Psi_0|\left(\phi(0)\pi(0)+\pi(0)\phi(0)\right)|\Psi_0\rangle\frac{1}{2\omega}\sin\omega(t_1+t_2) - \tag{2.63}$$

$$-\frac{i}{2\omega}\sin\omega|t_1-t_2| \tag{2.64}$$

This is expressed in terms of quantities that depend on the initial state. Introducing creation and annihilation operators at $t = 0$ through $\phi(0) = \frac{1}{\sqrt{2\omega_0}}(a_0 + a_0^\dagger)$ and $\pi(0) = i\sqrt{\frac{\omega_0}{2}}(-a_0 + a_0^\dagger)$, and imposing the initial condition associated to the ground state of the initial Hamiltonian, $a_0|\Phi_0\rangle = 0$, we find:

$$\langle\Psi_0|\phi^2(0)|\Psi_0\rangle = \frac{1}{2\omega_0} \tag{2.65}$$

$$\langle\Psi_0|\pi^2(0)|\Psi_0\rangle = \frac{\omega_0}{2} \tag{2.66}$$

$$\langle\Psi_0|\left(\phi(0)\pi(0) + \pi(0)\phi(0)\right)|\Psi_0\rangle = 0 \tag{2.67}$$

And the propagator for ((2.57) ,(2.58)), the system with one oscillator, is:

$$C_{\rm q}(t_1, t_2) = \frac{(\omega - \omega_0)^2}{4\omega^2\omega_0}\cos\omega(t_1 - t_2) + \frac{\omega^2 - \omega_0^2}{4\omega^2\omega_0}\cos\omega(t_1 + t_2) + \frac{1}{2\omega}e^{-i\omega|t_1 - t_2|} \tag{2.68}$$

Deep Quench Limit:

Expression (2.68) is to be inserted in (2.56) in order to get the propagator for the system with many non-interacting oscillators (2.54). Let us do that restricting to the *deep quench limit*, that is, taking

$$m_0 \gg m \tag{2.69}$$

$$t \equiv (t_2 - t_1) \gg m_0^{-1} \tag{2.70}$$

$$r \equiv |(\mathbf{r}_2 - \mathbf{r}_1)| \gg m_0^{-1} \tag{2.71}$$

This limit maintains the essential phenomenology of quenches that is relevant for this work. The full two point function (2.56), after substituting (2.68) and restricting to the deep quench limit, takes the form:

$$C_{\rm dq}(r, t) = \int \frac{d^d\mathbf{k}}{(2\pi)^d}e^{i\mathbf{k}\cdot\mathbf{r}}\frac{m_0}{4\omega_k^2}(1 - \cos(2\omega_k t)) \tag{2.72}$$

For the massless case ($m = 0$ and $\omega_k = |\mathbf{k}|$) exact expressions for the propagator can be found. For 1+1 dimensions we have

$$C_{\rm dq}(r, t) = \begin{cases} 0 & \text{, for } r > 2t \\ \frac{m_0}{8}(2t - r) & \text{, for } r < 2t \end{cases} \tag{2.73}$$

For the massive case, $m \neq 0$, (2.72) is integrated numerically. A plot of the result is shown in Figure (2.1). We see that the propagator vanishes for $r > 2t$. We find analytical expressions for $r < 2t$ in the asymptotic regime for large r and t for d space dimensions:

$$C_{\rm dq}^{(d)}(r, t) \sim \begin{cases} 0 & \text{, for } r > 2t \\ t^{-d/2}\cos(2mt) & \text{, for } r < 2t, \quad \text{with fixed } r \text{ and large } t \\ \dfrac{e^{-mr}}{r^{(d-1)/2}} & \text{, for } r < 2t, \quad \text{and for large } r \end{cases} \tag{2.74}$$

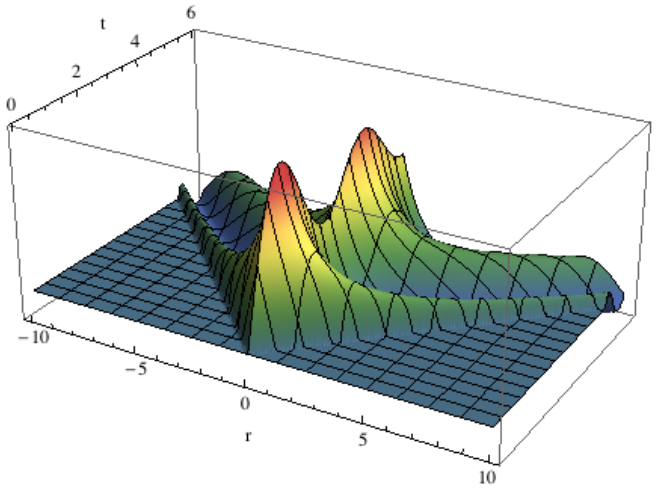

Figure 2.1: Numerical integration of (2.72), the massive propagator $C_{\rm dq}$ in in the deep quench limit, plotted in arbitrary units. The horizon at $r = 2t$ is manifest, as $C_{\rm dq}$ vanishes for $r > 2t$.

2.2.2 Evolution of Entanglement Entropy in CFT$_{1+1}$ after a Quench

In this section we study some dynamics of quantum quenches in 1+1 dimensional CFTs found in [33][5]. The initial state will be the ground state of a non-critical system with mass gap m_0, while after the quench the mass gap will be zero and the tools of CFT can be applied.

In section 2.1.3 it was shown how the trace of the n-th power of the reduced density matrix is equivalent to the correlation function of twist operators in the non replicated geometry inserted at the boundaries of the subsystem. As conformal invariance fixes the form of these correlation functions, the manifold over which the path integral is defined encodes the details of the physical situation. In this way we showed in section 2.1.3 how the complex plane is used for computing the ground state density matrix, and how the cases of thermal equilibrium state and compact space are reachable by means of conformally mapping from the original complex plane. Then, to analyze a quantum quench, we first need to identify the appropriate manifold.

In the path integral, a state after a quench is essentially implemented through a restriction over the domain of integration. Let us repeat the discussion that led to the manifold $\mathcal{M}_n$, but this time specifically for the quenched system. If at $t = 0$ the state of the system is $|\psi_0\rangle$, at any (real) time the elements of the density matrix are:

$$\langle\psi''|\rho(t)|\psi'\rangle = \langle\psi''|e^{-itH}|\psi_0\rangle\langle\psi_0|e^{itH}|\psi'\rangle \tag{2.75}$$

In order to make the associated path integral absolutely convergent, we introduce a factor $e^{-\epsilon H}$. The physical effect of this inclusion is to filter out high energy modes (typically above the inverse of the regulator, ϵ^{-1}). We have

$$\langle\psi''|\rho(t)|\psi'\rangle_\epsilon = Z^{-1}\langle\psi''|e^{-itH-\epsilon H}|\psi_0\rangle\langle\psi_0|e^{itH-\epsilon H}|\psi'\rangle \tag{2.76}$$

With the normalization constant given by $Z = \langle\psi_0|e^{-\epsilon H}|\psi_0\rangle$. The expression (2.76) corresponds to the product of two path integrals that describe unitary evolution in an ana-

lytically continued time, which runs from $-\epsilon - it$ to 0 for the first integral, and from 0 to $\epsilon - it$ the second. This strip is plotted in Figure (2.2). The reduced density matrix can thus be built as a path integral over this strip geometry, where in addition we need to sew together the pieces of the two edges along $\tau = 0$ that are not in the subsystem A (this is equivalent to taking the trace over the complement of A). Then $\mathrm{Tr}\rho_A^n$ is a path integral over a manifold built by replicating n times the strip geometry with cyclic identifications along the branch points.

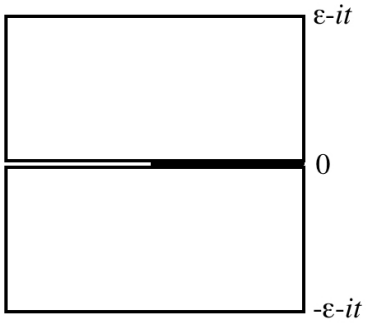

Figure 2.2: Representation of the manifold over which CFT correlation functions of twist operators are computed for obtaining $\mathrm{Tr}\rho_A^n$ after a quantum quench, as in (2.77) .

As we shall see below, there is a conformal mapping relating the strip geometry with the upper half complex plane, and we shall address to some aspects of boundary conformal field theories (BCFT) [33]. In particular, we want to study the system in the limit in which the time t after the quench and the size ℓ of the subsystem are much larger than the microscopic scales, so the renormalization group (RG) theory can be applied. Then, for a conformal hamiltonian, there is a bulk RG fixed point. The boundary conditions then flow to a boundary fixed point, so in this limit it is possible to replace $|\psi_0\rangle$ by the corresponding RG-invariant boundary state $|\psi_0^*\rangle$. This is equivalent, at leading order, to changing the boundary conditions and introduce the *extrapolation length* τ_0, which measures the typical distance between the actual boundary state and the RG-invariant one. It is of order the inverse mass gap of the pre-quench hamiltonian: $\tau_0 \sim m_0^{-1}$. At the end the effect will be changing ϵ by $\epsilon + \tau_0$. At this point the regulator can be removed,and we find that the strip in which to compute the path integral has a width $2\tau_0$ in the time direction.

Once the manifold has been identified, the EE can be computed using (2.9). $\mathrm{Tr}\rho_A^n$ transforms as a two point function of primary operators of dimension d_n.

$$\mathrm{Tr}\rho_A^n = \langle \tilde{\mathcal{T}}_n(z_2)\mathcal{T}_n(z_1)\rangle_{\mathrm{strip}} \tag{2.77}$$

We do not know a priori what form the two point function has in the quench strip geometry due to conformal invariance. However, the conformal transformation

$$z(w) = e^{\pi w/2\tau_0} \tag{2.78}$$

Maps the strip to the upper half plane. Thus

$$\langle \tilde{\mathcal{T}}_n(w_2)\mathcal{T}_n(w_1)\rangle_{\mathrm{strip}} = |w'(z_1)w'(z_2)|^{-d_n}\langle \tilde{\mathcal{T}}_n(z_2)\mathcal{T}_n(z_1)\rangle_{\mathrm{UHP}} \tag{2.79}$$

In the upper half plane the correlation function is fixed by conformal invariance and has the form:

$$\langle \tilde{\mathcal{T}}_n(z_2)\mathcal{T}_n(z_1)\rangle_{\text{UHP}} = c_n \left(\frac{|z_1 - \bar{z}_2||z_2 - \bar{z}_1|}{|z_1 - z_2||\bar{z}_1 - \bar{z}_2||z_1 - \bar{z}_1||z_2 - \bar{z}_2|} \right)^{d_n} \mathcal{F}_n(x) \tag{2.80}$$

Where x is the ratio

$$x = \frac{(z_1 - \bar{z}_1)(z_2 - \bar{z}_2)}{(z_1 - \bar{z}_2)(z_2 - \bar{z}_1)} \tag{2.81}$$

And the function $\mathcal{F}_n$ depends on the full operator content of the theory. In the limit $\ell/\tau_0, t/\tau_0 \gg 1$ we have

$$x \approx \frac{e^{\pi t/\tau_0}}{e^{\pi \ell/2\tau_0} + e^{\pi t/\tau_0}} \tag{2.82}$$

So $x \approx 0$ when $t < \ell/2$ and $x \approx 1$ when $t > \ell/2$. The latter case corresponds to having the points (z_1, z_2) deep in the bulk, then $\mathcal{F}_n(1) = 1$, as dictated by scaling. When $x \approx 0$ the insertion points are close to the boundary, and $\mathcal{F}_n(0) = 1$ as well. Thus, the exact form of $\mathcal{F}_n$ in all its domain does not affect the the physics after the quench in the limit $\ell/\tau_0, t/\tau_0 \gg 1$. Then, as for these purposes $\mathcal{F}_n = 1$ in (2.81), the details of the underlying theory are irrelevant, and $\text{Tr}\rho_A^n$ is determined only by the factors imposed by conformal symmetry in (2.79) and (2.81). We obtain

$$\text{Tr}\rho_A^n \approx c_n \left(\frac{\pi}{2\tau_0} \right)^{d_n} \left(\frac{e^{\pi \ell/2\tau_0} + e^{\pi t/\tau_0}}{e^{\pi \ell/2\tau_0} e^{\pi t/\tau_0}} \right)^{d_n} \tag{2.83}$$

And using (2.9) the EE:

$$S_A(t) \approx -\frac{c}{3} \log \tau_0 + \begin{cases} \dfrac{\pi c t}{6\tau_0} & \text{, for } t < \ell/2 \\ \dfrac{\pi c \ell}{12\tau_0} & \text{, for } t > \ell/2 \end{cases} \tag{2.84}$$

The sharp transition at $t = \ell/2$ is smoothed over a region $|t - \ell/2| \sim \tau_0$, which separates equilibrated from non-equilibrated situations as shown by (2.84): For times $t < \ell/2$ the EE grows linearly, while for $t > \ell/2$ it saturates to a constant value that depends linearly with the size ℓ of the system A.

2.2.3 Horizon Effect and the Quasiparticles Picture

A notable feature has arisen concerning the spacetime dependence after the quench of correlation functions of harmonic oscillators in section 2.2.1 and of the EE in section 2.2.2. Equations (2.73) and (2.74) express the propagator of the oscillators system as a piecewise defined function, such that for $r > 2t$ the propagator is identically zero. The surface $r = 2t$ is said to be a *horizon*, as it splits the spacetime into two regions with null and non null correlations. An analog situation is found for the EE in a CFT as expressed in (2.84): The surface $\ell = 2t$ separates two domains where the EE behaves differently.

As it is familiar from special relativity, the propagation of interactions at a finite speed imposes causality, and the imprint is a light cone or horizon in spacetime diagrams. The domain of dependence of the propagator or the entanglement entropy in the quench scenarios above shows similar features: the spacetime surface $\ell = 2t$ is a causal cone or

horizon, which allows for interpretating that the effects of the perturbation produced by the quench propagate at a finite speed and causality is manifest. This has been referred as the *Horizon Effect*. An important implication of this causal behavior is that relaxation can only be attained at the local level: An infinitely long system would require an infinite time to equilibrate.

Although the coupled oscillators model of 2.2.1 consists in non interacting fields, remarkably the Horizon Effect is an essential feature of quantum quenches and is also present in interacting QFTs. Let us note that no details about interactions have been taken into account in the EE case in 2.2.2. Furthermore, as it will be shown holographically in this work, the Horizon Effect will appear even in the strongly coupled regime of CFT.

In order to interpret physically the causal structure associated to the Horizon Effect, Cardy and Calabrese introduced in [5] a model in which the perturbation after the quench is transported by some quasiparticles that propagate causally and classically at a finite speed.

At the instant of the quench, the excess of energy of the initial state $|\psi_0\rangle$ relative to the ground state of the hamiltonian H sources quasiparticle excitations. These are created in pairs (in 1+1 dimensions) at every point of space. Once created, the quasiparticles propagate freely in opposite senses all at the same speed $v_E = 1$ in a CFT. Two quasiparticles in the same pair are highly entangled, while quasiparticles created at separated points are less entangled, until the separation reaches the correlation length $\sim \tau_0$ of the initial hamiltonian. Particles created at bigger distances are not correlated at all.

Let us first consider the case in which $m_0 \to \infty$. The correlation length vanishes and there is only entanglement between quasiparticles created at the same point. At a given time the EE of a subsystem A will be proportional to the number of quasiparticles in A entangled with quasiparticles out of A. In this case this is the number of pairs of quasiparticles that have only one component in A, see Figure (2.3). As all the quasiparticles propagate at the same speed $v = 1$, the number of pairs contributing to the entanglement of a region of size ℓ grows linearly with time until $t = \ell/2$, when a constant value is attained. Once the saturation has been reached, the EE depends linearly on ℓ, as the quasiparticles were created homogeneously and bigger subsystems contain extensively more quasiparticles. This is exactly the result found in (2.84).

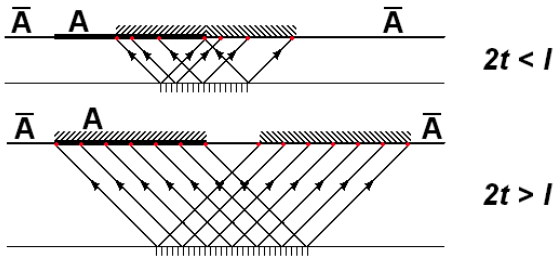

Figure 2.3: Motion of pairs of entangled quasiparticles. For $t < \ell/2$ there are still interior points in the interval that have not been reached by any entangled quasiparticle. The number of such points decreases linearly with time, because the quasiparticles move all at the same speed and they were created homogeneously. For $t > \ell/2$ a constant number of quasiparticles is reached, and is proportional to ℓ.

If the correlation length has a finite value, then a given quasiparticle is entangled not only with its partner into the pair but also with neighboring quasiparticles up to a separation $\sim \tau_0$. Then the saturation of the entanglement entropy to a constant value is finally attained at a time $t \sim \ell/2 + \tau_0/2$, explaining the rounding of the critical region at $t = \ell/2$ over a size $|t - \ell/2| \sim \tau_0$.

It is noted that the fact that even in non integrable systems at strong coupling the free quasiparticles picture works well, as it is shown holographically, does not bring support to take this model as an actual physical description of these processes in general theories, but as a tool to model the causal behavior associated with the Horizon Effect.

2.2.4 Effective Thermalization and the Generalized Gibbs Ensemble

Let us take again the quenched coupled oscillators of section 2.2.1 and the propagator for that system, obtained in (2.68). At the same time let us consider the same theory at finite temperature $T = \beta^{-1}$. The thermal propagator in real time is:

$$C_{\rm th}(t_1, t_2, k) = \frac{1}{2\omega_k}\left(e^{-i\omega_k|t_1-t_2|} + 2\frac{\cos\omega_k(t_1-t_2)}{e^{\beta\omega_k}-1}\right) \tag{2.85}$$

This looks like the quench propagator $C_{\rm q}(t_1, t_2, k)$ in (2.68) except for the $(t_1 + t_2)$-term. However, for large times this term can be neglected. The equivalence between quench and thermal propagators allows to conclude that for late times the system tends to a state with thermal correlations, that is, an *Effective Thermalization* takes place after the quench. By comparison, the effective temperature $\beta_{\rm eff}^{-1}$ is given by

$$\beta_{\rm eff} = \frac{2}{\omega_k}\log\left(\frac{\omega_k+\omega_0}{\omega_k-\omega_0}\right) \tag{2.86}$$

In the free system (2.54) the different momentum modes do not mix, preventing thermalization to a common effective temperature, as it is expressed in the dependence of $\beta_{\rm eff}$ on k. The large distance behavior of the propagator is determined by the$k = 0$ mode, for which the temperature coincides with the collective effective temperature obtained in the deep quench limit ($m_0 \gg m$ and $m_0 \gg k$):

$$\beta \approx \frac{4}{m_0} \tag{2.87}$$

However, the state is not stationary and therefore nor thermal. In fact, unitary evolution cannot take a pure state into a mixed one. This system *looks like* thermal in the sense that in the mentioned regimes correlation functions have a thermal form at at a temperature given by (2.87). As correlators determine all local observables in a free theory, these also acquire thermal values, making the system look like thermal at the macroscopical level.

Considering the example of the EE in section 2.2.2, regarding the results in (2.84) we observe an analogous behavior. For regions inside the horizon, $\ell < 2t$, the EE grows linearly with ℓ, thus it is extensive as the thermal entropy is. The slope is proportional to the temperature. By comparison we conclude that the EE for $\ell < 2t$ corresponds to thermal entropy at an effective temperature

$$\beta_{\rm eff} = 4\tau_0 \approx \frac{4}{m_0} \tag{2.88}$$

These systems have shown how the region inside the horizon after a quench looks like thermal, at an effective temperature that is inversely proportional to the mass off the hamiltonian whose ground state is taken as the initial state in the process.

Two apparent contradictory facts have appeared in the effective thermalization phenomenon concerning the nature of the asymptotic late time state. On the one hand, as the initial state is pure and the evolution is unitary, the final asymptotic state must still be pure. On the other hand, macroscopic observables on the asymptotic late time state have thermal values, and the thermal equilibrium state is mixed. One understands intuitively that a finite system can be thermalized being in contact with its infinite complement which acts as a bath [5][37], but this is not enough to predict the value of the equilibrium temperature.

It has been proposed that the final asymptotic state is given by the *Generalized Gibbs Ensemble* (GGE) [71]. This is defined as the state that maximizes the entropy subject to all the integrals of motion. Let the full set of integrals of motion be $\{I_m\}$. The GGE is then described by the density matrix

$$\rho = Z^{-1} e^{-\sum_m \lambda_m I_m} \tag{2.89}$$

With

$$Z = \mathrm{Tr}\left(e^{-\sum_m \lambda_m I_m}\right) \tag{2.90}$$

And the $\{\lambda_m\}$ being Lagrange multipliers, which are fixed by the conservation of the corresponding integrals of motion, provided these are known at $t = 0$:

$$\langle I_m \rangle = \mathrm{Tr}(\rho I_m) = \langle I_m \rangle_{t=0} \tag{2.91}$$

The associated state is pure only if the model integrable. Otherwise, the GGE represents a mixed state and it does not fully explain the evolution after a quench from a pure initial state.

The GGE for the system of coupled oscillators of section 2.2.1 is obtained as follows. The hamiltonian can be diagonalized and expressed as

$$H = \sum_k \omega_k n_k = \sum_k h_k \tag{2.92}$$

With $n_k = a_k^\dagger a_k$ being the number of particles with momentum k. In the last equality the total hamiltonian has been written as the sum of effective hamiltonians $h_k = \omega_k n_k$ for each momentum value k. The infinite set $\{n_k\}$ are integrals of motions, since $[H, n_k] = 0$. The GGE for this system is

$$\rho = Z^{-1} \exp\left(-\sum_k \lambda_k n_k\right) \tag{2.93}$$

Rearranging this expression to write

$$\rho = Z^{-1} \exp\left(-\sum_k \beta_k h_k\right) \ , \tag{2.94}$$

this density matrix may be interpreted as describing an equilibrium thermodynamic state with effective momentum-dependent temperatures $\beta_k = \frac{\lambda_k}{\omega_k}$.

In order to determine the Lagrange multipliers we compute $\langle n_k \rangle$ from the density matrix:

$$\langle n_k \rangle = \mathrm{Tr}\,(\rho n_k) = -\frac{\partial}{\partial \lambda_k} \log Z = \frac{1}{e^{\lambda_k} - 1} \tag{2.95}$$

and also at $t = 0$:

$$\begin{aligned} \langle n_k \rangle &= \langle a_k^\dagger a_k \rangle = \frac{1}{4} \left(\sqrt{\frac{\omega_k}{\omega_{0k}}} - \sqrt{\frac{\omega_{0k}}{\omega_k}} \right)^2 \langle a_{(0)-k} a_{(0)-k}^\dagger \rangle \\ &= \frac{1}{4} \left(\frac{\omega_k}{\omega_{0k}} + \frac{\omega_{0k}}{\omega_k} \right) - \frac{1}{2} \equiv d_k^2 \end{aligned} \tag{2.96}$$

Equating the last two expressions allows to determine λ_k. The effective temperature is then

$$\beta_{\mathrm{eff}}(k) = \frac{\lambda_k}{\omega_k} = \frac{1}{\omega_k} \log \left(1 + d_k^{-2} \right) \tag{2.97}$$

The effective temperature is in general dependent on k, even for the conformal evolution, $m = 0$, with arbitrary m_0. The large distance effects are described by the $k = 0$ mode, for which the temperature is the same as the common temperature obtained for all the modes in the limit $m_0 \to \infty$:

$$\beta_{\mathrm{eff}}(m = 0) = \frac{4}{m_0} \tag{2.98}$$

3
Holographic Basics

In the second introductory chapter some aspects of the AdS/CFT correspondence are briefly reviewed, in particular the holographic entanglement entropy.

3.1 Holography

Generically, holography refers to the equivalence between gravitational theories and quantum theories with no dynamical gravity in a lower dimensional space. The AdS/CFT duality is one of the best instances of holographic relationships between two theories, as these are explicitly known. The correspondence was established at the end of last century [6] [7] [8], but before that, several discoveries were made, suggesting that holography can be something intrinsic to some of the known theories of physics. Three of these milestones were:

- Gauge theories are stringy.
  G. t'Hooft studied the structure of interactions in $U(N)$ gauge theories [10], and showed that, in the limit $N \to \infty$ and g^2N fixed, the perturbative expansions have a topological structure in powers of $1/N$ similar to those found in perturbative closed strings theories in powers of the string coupling constant. The extension of this result to $SU(N)$ gauge theories is possible, as the difference between quark propagators in $SU(N)$ and $U(N)$ theories is a term that vanishes for $N \to \infty$.

- AdS_3 Asymptotics and CFT_{1+1}.
  Brown and Henneaux found explicit relations between AdS_3 gravity and CFT_{1+1} [11].The global symmetry group of CFT_{1+1} makes this theory one of the best known CFTs, and on the other side three-dimensional gravity is a singularly simple gravity theory. They showed that the group algebra of the asymptotic isommetry group of AdS_3 is the Virasoro algebra, with the central charge related to the gravity coupling constant by $c = \frac{3R}{2G_N^{(3)}}$.

- Holographic Principle.
  The intrinsic causal structure of gravity imposes several bounds on the entropy, stating that for a given volume, bounds on the entropy depend on the boundary of the volume. Without requiring to detail the character of the degrees of freedom, these inequalities are essentially a statement about amount of information as is encoded by the entropy. The holographic principle asserts that [12] [13] [14]:

  The gravitational dynamics of a given volume is describable in terms of degrees of freedom defined on the boundary of that volume.

The AdS/CFT Correspondence.

The first explicit realization of two theories related holographically was proposed by Maldacena [6]. A stack of N parallel D3-branes in a (9+1) dimensional Minkowski spacetime was taken, and two different descriptions of this system were considered.

On the one hand, the string theory associated to this system contains two kind of excitations: excitations of the branes, described by open strings ending in the branes, and excitations of the rest of space, described by closed strings. At low energy the massive modes are integrated out and the effective theory is schematically defined by

$$I = I_{\text{bulk}} + I_{\text{branes}} + I_{\text{int}} \ , \tag{3.1}$$

Here I_{bulk} is the action of the massless closed strings in the bulk, which form a supermultiplet of type IIB supergravity. I_{branes} is the action of the branes, and contains the action for a vector multiplet of an $\mathcal{N} = 4$ supersymmetric $U(N)$ gauge theory together with higher derivative corrections proportional to powers of α'. I_{int} stands for the interactions between the branes and bulk parts.

The decoupling between the branes and bulk sectors arises when taking the limit $\alpha' \to 0$ while keeping the energy fixed. Then I_{branes} becomes the action of the pure $\mathcal{N} = 4$ $U(N)$ super Yang Mills theory, I_{bulk} describes the free supergravity action and I_{int} vanishes.

On the other hand, a supergravity approach can also be associated to the original system of N parallel D3-branes. In this description, the branes act as sources for the supergravity equations. The solution is a black brane metric in the (9+1) dimensional space. This space produces a redshift such that an observer at infinity associates low energies to any excitation near the horizon. Thus, in the low energy limit, an observer at infinity perceives only low energy excitations which correspond either to low energy massless modes in the bulk or to otherredshifted arbitrary excitations near the horizon. Theses two sectors become independent in the low energy limit, and what is left is supergravity in the bulk decoupled from the modes of the near horizon geometry, which is $\text{AdS}_5 \times S^5$.

Comparing the two descriptions of the low energy limit of the N parallel D3-branes, we note that, as one of the decoupled theories coincides in both descriptions (free supergravity in the bulk), it is natural to conjecture the equivalence between the other two theories, allowing to state that

Type IIB superstring theory in $AdS_5 \times S^5$ is dual to $\mathcal{N} = 4$ $U(N)$ super Yang- Mills theory in 3+1 dimensions.

Specifically, the two related theories are:

- Type IIB superstring theory on $\text{AdS}_5 \times S^5$, with both AdS_5 and S^5 spaces having the same radius R, with the string coupling constant g_s and with a quantized flux for the 5-form F_5 across the sphere: $\int_{S^5} F_5 = N$.
- $\mathcal{N} = 4$ super Yang-Mills theory in 4 dimensions with gauge group $U(N)$ and coupling constant g_{YM}.[1]

[1] A $U(N)$ gauge theory is, up to some $\mathbb{Z}_N$ identifications, equivalent to a free $U(1)$ vector multiplet times an $SU(N)$ gauge theory. The $U(1)$ degrees of freedom correspond in the gravity picture to excitations living in the region connecting the throat with the asymptotic part of the space. If we consider that the bulk AdS theory does not include these throat excitations, then the correspondence is actually relating AdS gravity with an $SU(N)$ theory.

The relations between the two sets of parameters are:

$$\left(\frac{R^2}{\alpha'}\right)^2 = g_{\rm YM}^2 N \quad , \quad 4\pi g_s = g_{\rm YM}^2 \tag{3.2}$$

Equivalently, we may express these relations in terms of other parameters. In the gravity side we introduce the string length through $\ell_s^2 = \alpha'$, and also eliminate g_s in favor of the Planck length ℓ_P using $\ell_P = g_s^{1/4}\ell_s$. In the field theory side we introduce the t'Hooft parameter $\lambda = g_{\rm YM}^2 N$. We obtain

$$\left(\frac{\ell_s}{R}\right)^2 = \frac{1}{\sqrt{\lambda}} \tag{3.3}$$

$$\left(\frac{\ell_P}{R}\right)^8 = \frac{1}{(4\pi)^2}\frac{1}{N^2} \tag{3.4}$$

Regarding (3.3), when $\left(\frac{\ell_s}{R}\right)^2 \ll 1$, the extended nature of the microscopic string can be neglected, as it is much smaller than the curvature of the space. Also, as the mass of stringy states is proportional to $1/\ell_s$, in this limit the contribution of massive states to low energy processes is suppressed, and one can consider only the massless modes, that is, a supergravity theory. In the field theory side this corresponds to $\lambda \gg 1$. Incorporating stringy effects in supergravity (α' expansion) amounts to an expansion in powers of $1/\sqrt{\lambda}$ in the field theory.

Considering now (3.4), the ratio $\left(\frac{\ell_P}{R}\right)^8$ determines the quantum gravitational fluctuations. These are suppressed when $\left(\frac{\ell_P}{R}\right)^8 \ll 1$, which is equivalent to $N^2 \gg 1$. In this limit the quantum nature of the string is suppressed. This is also seen by considering large N at fixed λ (the planar limit in the field theory). Then, by (3.2), we have $g_s \to 0$, thus quantum interactions of the string vanish.

In summary, N^2 controls the quantum character of the gravity theory and λ the extended nature of the fundamental object in the gravity theory. By taking different limits we arrive to different forms of the duality, from the most general to the more specific, they are summarized in the next table:

Parameters	Quantum Field Theory	Gravitational Theory
$\forall$ N, λ	$\mathcal{N} = 4$ SYM	Full string theory on $AdS_5 \times S^5$
$N \to \infty$, λ fixed	$\mathcal{N} = 4$ SYM in the planar limit. $1/N$-expansion	Classical string theory on $AdS_5 \times S^5$. g_s-expansion (perturb str. th.)
$N \to \infty$, $\lambda \to \infty$	$\mathcal{N} = 4$ SYM in the planar limit and at strong coupling. $1/\sqrt{\lambda}$-expansion	Classical supergravity ($\sim$ Einstein grav.) on $AdS_5 \times S^5$. α'-expansion

The large N and λ limit amounts to classical supergravity in the bulk, which is essentially Einstein gravity coupled to matter fields. In this work we shall consider the AdS/CFT correspondence only in this weaker form: the gauge QFT will be in the limit of infinite colors and at strong coupling, and the gravitational dual will be General Relativity with negative cosmological constant coupled to some matter fields.

AdS Fields ↔ CFT operators.

The correspondence relates operators in the CFT with bulk field with prescribed boundary conditions. When the field theory is deformed by introducing a source $\phi(x)$ for a local gauge invariant operator $\mathcal{O}(x)$, that is, by adding to the action a term $\int d^4x\phi(x)\mathcal{O}(x)$, then a dual bulk field $\Phi(x,z)$ is incorporated into the gravity theory with an asymptotic value identified with the field theory source:[2]

$$\phi(x) \approx \lim_{z\to 0} \Phi(x,z) \tag{3.5}$$

Where z is the radial coordinate of AdS and the boundary is at $z=0$. Thus, $\phi(x)$ and $\mathcal{O}(x)$ are dual in the sense that the AdS field acts as a source for the field theory operator

An important operator in the QFT is the stress energy tensor $T_{\mu\nu}(x)$. Since it couples to the metric through $\int d^4x g_{\mu\nu}(x)T^{\mu\nu}(x)$, we identify the bulk metric $G_{\mu\nu}(x,z)$ as its dual bulk field, and, according to the previous discussion, it obeys $\lim_{z\to 0} G_{\mu\nu}(x,z) \approx g_{\mu\nu}(x)$.

An essential statement is the identification of the partition function of both theories with the asymptotic value for the bulk field as stated in (3.5). Then [7] [8]:

$$\mathcal{Z}_{\text{CFT}}[\phi(x)] = \mathcal{Z}_{\text{grav}}[\Phi(x,z) \mid_{z=0} \approx \phi(x)] \tag{3.6}$$

This partition function is difficult to obtain in general. However, in the classical gravity limit the integral is dominated by:

$$\mathcal{Z}_{\text{grav}} \approx e^{-I_{\text{grav}}} \tag{3.7}$$

With I_{grav} being the on-shell classical gravity action subject to the boundary conditions $\Phi(x,z) \mid_{z=0} \approx \phi(x)$.

Correlation Functions. Geodesic Approximation.

Correlation functions of a boundary operator $\mathcal{O}$ are obtained by identifying its dual ϕ and computing bulk correlation functions extracted from functional derivation of (3.6). This is particularly useful for the case of large N and λ, in which the field theory is at strong coupling and it admits no perturbative computations but the dual gravity theory is classical and its partition function can be well approximated by the on-shell action.

Equation (3.6) is a crucial element in the correspondence, as it establishes a precise operational relation between the gravitational and the gauge theories by the identification of their partition functions. It also follows from (3.6) the *holographic* spirit of the correspondence, since the conformal boundary of AdS can be considered as the manifold where the field theory is defined. A set of prescriptions arises to compute holographically field theory correlators in terms of perturbative bulk interactions described by Witten diagrams [7].

Alternatively, the two point function of an operator $\mathcal{O}$ of conformal dimension Δ can be found holographically with

$$\langle \mathcal{O}(x_1)\mathcal{O}(x_2)\rangle = \int \mathcal{D}\mathcal{P} e^{i\Delta\ L(\mathcal{P}(x_1,x_2))} \tag{3.8}$$

[2] The second order equations of motion for the bulk fields allow for two independent solutions or modes. At the boundary of AdS one is finite and the other diverges. It is the divergent term (with a renormalization factor omitted in (3.5)) which is identified with the source of the dual QFT operator. The normalizable mode is identified with the expectation value of the corresponding dual operator, $\langle \mathcal{O}(x)\rangle$.

Where the integral is summing over all possible bulk paths such that they end at x_1 and x_2 at the boundary of AdS, and $L(\mathcal{P})$ is the proper length along the path $\mathcal{P}$ [21] [42].

If the conformal dimension is large, $\Delta \gg 1$, a WKB approximation can be performed on the integral, which results to be dominated by the paths associated to the saddle points of the integral, i.e. geodesics. The correlator is thus expressed as a sum over geodesics:

$$\langle \mathcal{O}(x_1)\mathcal{O}(x_2)\rangle = \sum_{\text{geod}} e^{-\Delta\ L_{\text{geod}}(x_1,x_2)} \tag{3.9}$$

Where $L_{\text{geod}}(x_1, x_2)$ is the geodesic distance between points x_1 and x_2.

AdS space.

AdS space is the background of the gravity theory. It appears in the correspondence as the near horizon geometry of the stack of N D3-branes in the supergravity description. It is a maximally symmetric space, solution of the vacuum Einstein equations with negative cosmological constant (the classical theory of interest here). Let the coordinates X_a parametrize a $(d+2)$-dimensional Minkowski spacetime with two timelike coordinates such that $ds^2 = -dX_{-1}^2 - dX_0^2 + \sum_{i=1}^{d} dX_i^2$. AdS_{d+1} space is defined by the hyperboloid $X_{-1}^2 - X_0^2 + \sum_{i=1}^{d} X_i^2 = -R^2$ embedded in the $(d+2)$-dimensional Minkowski space. R is a parameter with units of length. The AdS metric is the induced metric of the flat ambient space in the hyperboloid. [3]

The form of the radial coordinate whose limit defines the conformal boundary of AdS is unspecified, and depending on this choice surfaces at constant radius and the boundary can have different geometry or even different topology [46]. We will use Poincaré and global coordinates in Chapters 4 and 5 respectively.

Thermodynamics.

The correspondence relates other states than the field theory vacuum to spaces that are asymptotically AdS. One of such excited states corresponds to thermal equilibrium [9]. The dual asymptotic AdS space is invariant under translations in the conformal boundary directions and rotations of the spatial dimensions. In addition, the thermodynamic properties of the CFT state must exist also in the gravitational dual, as the partition functions are identified with (3.6).

The thermal structure of AdS was studied by Hawking and Page [43], who found that two solutions, thermal AdS and Schwarzschild-AdS, are dominant in the gravitational path integral for temperatures below and above a critical temperature, respectively. The duality relates thermal AdS with the QFT confined phase, and Schwarzschild-AdS with the QFT deconfined phase [9]. For AdS_{d+1} with $d > 3$ Schwarzschild AdS black holes have negative specific heat for small radius, and they are unstable in the canonical ensemble as they are in fat space.

For large black holes, the black hole and the CFT canonical ensemble thermodynamic parameters are identified. The entropy is proportional to the area of the horizon.

$$S = \frac{\text{Vol}(S^{d-1}) r_h^{d-1}}{4G_N} \tag{3.10}$$

[3] This space allows for closed timelike trajectories, contrary to what happens for its universal covering space.

3.2 Holographic Entanglement Entropy

Ryu and Takayanagi (RT) conjectured that the entanglement entropy of a given subsystem in the field theory can be obtained holographically [3]. The correspondence states that the AdS space encodes all the data of the dual CFT. The UV of the field theory corresponds to the region close to the boundary, and the IR to the bulk. As reviewed in chapter 2, the EE is associated to a lack of accessibility to some part of the total Hilbert space: the EE of the system A is obtained from its reduced density matrix, which is what remains after taking the trace of the total density matrix over the degrees of freedom of the complement $\bar{A}$. This split in the QFT Hilbert space is implemented in the bulk by postulating some *holographic screen* associated to A that hides the part of the space related to $\bar{A}$. Let this surface be named γ_A. Consistently, we assume that γ_A is anchored at the common boundary of A and $\bar{A}$ (see Figure 3.1), $\partial\gamma_A = \partial\bar{A} = \partial A$. The surface γ_A has the same dimensionality than the spatial system A, $(d-1)$, or equivalently, codimension two in the bulk. γ_A is associated to A through the homology condition: the surface γ_A and the system A form the boundary of a d-dimensional volume Σ in AdS. That is:

$$\gamma_A \cup A = \partial\Sigma \tag{3.11}$$

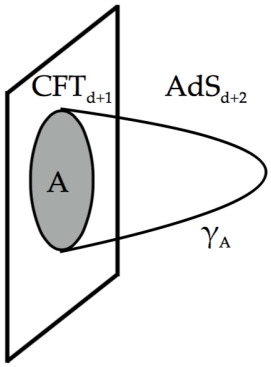

Figure 3.1: The surface γ_A is anchored to ∂A at the boundary of AdS and extends into the bulk. The RT prescription demands γ_A to have a minimal area.

The surface γ_A is fully defined by imposing a condition inspired from gravitational entropy bounds [41]. It is sufficient to refer to the simplest form, the Bekenstein entropy bound, which states that for a given spacelike region Σ, the maximum entropy that it can hold is bounded:

$$S_\Sigma \leq \frac{\text{Area}(\partial\Sigma)}{4G_N} \tag{3.12}$$

The prescription is to consider the severest bound in (3.12), so the holographic surface γ_A is required to be have minimal area. Having noted in checks in AdS_3/CFT_2 that the bound (3.12) is actually saturated for the minimal area surface, it is proposed that the same holds in higher dimensions too. The HEE is then:

The HEE of a space region A defined on the conformal boundary of AdS is proportional to the proper area of γ_A, the minimal surface on an equal time slice in AdS which

is anchored at ∂A at a constant time in the boundary and homologous to A (condition (3.11)):

$$S_A = \frac{\text{Area}(\gamma_A)}{4G_N} \tag{3.13}$$

For non static spaces the HEE is given by (3.13), but with γ_A being a surface of extremal area [4].

3.2.1 Properties

The properties of the EE are verified by the HEE as defined in (3.13):

- Divergence

  The divergence of the EE is one of the many UV divergences that occur in QFT. The holographic counterpart of a UV divergence in QFT is the divergence of the AdS metric for $r \to \infty$. This implies that the proper volume of any object that reaches the AdS boundary is divergent. This is the case of the HEE. Introducing a regulator a for the field theory amounts to cutting off the AdS space and restricting the AdS radial coordinate to $r \leq r_\infty$, where $r_\infty \sim 1/a$.

- Strong Subadditivity:

  The HEE verifies the property (2.12):

  $$S_A + S_B \geq S_{A\cup B} + S_{A\cap B} \tag{3.14}$$

  It can be shown that this actually holds not only for the proper area of the holographic surface γ, but for any extensive geometric quantity defined by that surface. The proof can be represented in geometric terms (see Figure (3.2)). The union of the surfaces associated to left hand side of (3.14) are rearranged according to:

  $$\text{Area}(\gamma_A)+\text{Area}(\gamma_B) = \text{Area}(\gamma_A\cup\gamma_B) = \text{Area}(\gamma_1\cup\gamma_2) = \text{Area}(\gamma_1)+\text{Area}(\gamma_2) \tag{3.15}$$

  Where γ_1 and γ_2 are such that they anchor $A\cup B$ and $A\cap B$ respectively. γ_1 and γ_2 are not required to obey the minimal area condition, so they have an area bigger or equal to the x surfaces that anchor $A\cup B$ and $A\cap B$ respectively, which are minimal by construction. That is:

  $$\text{Area}(\gamma_1) \geq \text{Area}(\gamma_{A\cup B}) \tag{3.16}$$
  $$\text{Area}(\gamma_2) \geq \text{Area}(\gamma_{A\cap B}) \tag{3.17}$$

  Then (3.14) holds.

- (Non) Extensivity and the AdS black hole:

  In a general background, $\text{Area}(\gamma_A)$ does not grow extensively with respect to the size of A. However, it does so on a black hole background for regions with typical scales bigger than β, when the minimal surface γ_A wraps a portion of horizon that grows proportionally with the size of the system. As a result, the proper area of such a surface is the area of the part of black hole horizon that is wrapped and depends extensively on the size of A. In this situation, the field theory EE is given by the dual AdS black hole entropy. In the other limit, for small systems for which the EE is only sensitive to vacuum correlations, the minimal surfaces are in the asymptotic part of the space where the metric is effectively pure AdS.

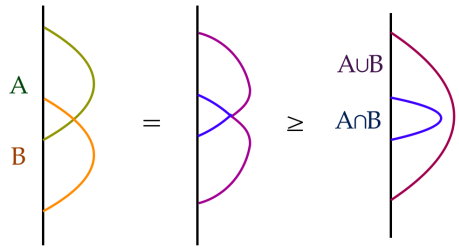

Figure 3.2: Scheme of the strong subadditivity relation (3.14).

3.2.2 Derivations of the Holographic Entanglement Entropy Proposal

In this section we briefly review some of the arguments supporting the RT formula (3.13) and the proof given in [76].

Assuming Holographic Approximations for Twist Field Correlators

An intuitive derivation of the HEE formula is presented in [44]. Using the replica trick, the quantity $\mathrm{Tr}\rho_A^n$ is expressed as correlators of twist fields $\mathcal{T}_n$. For an interval in a CFT_{1+1} the twist fields are defined at the endpoints of the interval, p and q, and $\mathrm{Tr}\rho_A^n$ is the two-point function. The conformal dimension has been obtained in (2.43) and is $d_n = \frac{c}{12}(n - n^{-1})$.

Two point functions can be obtained in AdS/CFT by the geodesic distance L_{pq} between the insertion points of the operators, as stated in the geodesic approximation (3.9), which is valid as long as the conformal dimension of the corresponding operator is large. This is the case of the twist fields, whose dimension is proportional to the central charge c, which in turn is large in the classical gravity regime of the correspondence. Then, we can write

$$\langle \mathcal{T}_n(p)\tilde{\mathcal{T}}_n(q)\rangle \approx e^{-d_n L_{pq}} \tag{3.18}$$

And, using (2.9), we find the HEE:

$$S_A = -\frac{\partial}{\partial n}\log \mathrm{Tr}\rho_A^n|_{n=1} = -\frac{\partial}{\partial n}\log\langle \mathcal{T}_n(p)\tilde{\mathcal{T}}_n(q)\rangle|_{n=1} = \frac{L_{pq}}{4G_N^{(3)}} \ , \tag{3.19}$$

where we made use of the $\mathrm{AdS}_3/\mathrm{CFT}_2$ relation $c = \frac{3}{2G_N^{(3)}}$.

In higher dimensions the same reasoning can be applied to arrive to the RT proposal for the HEE. $\mathrm{Tr}\rho_A^n$ is given by $\langle \mathcal{T}_n\rangle$, where the twist field is defined on ∂A. As for a spacelike Wilson loop [38] [39], we assume that :

$$\langle \mathcal{T}_n\rangle \approx e^{-\alpha_n \mathrm{Area}(\gamma_A)} \ , \tag{3.20}$$

where γ_A is the RT minimal surface in AdS and α_n is a constant such that $\lim_{n\to\infty}\frac{\alpha_n}{n} < \infty$. Then, using (2.9):

$$S_A = \left(\frac{\partial \alpha_n}{\partial n}\right)_{n=1} \mathrm{Area}(\gamma_A) \ , \tag{3.21}$$

which finally leads to the HEE formula, provided that $\left(\frac{\partial \alpha_n}{\partial n}\right)_{n=1} = \frac{1}{4G_N}$, which can actually be determined by computing the HEE at finite temperature when A is the total space, and comparing with the corresponding thermal entropy.

Asumming the Bulk Extension of $\mathcal{M}_n$

In the computation of $\mathrm{Tr}\rho_A^n$ through the replica trick, one is considering a field theory defined on the replicated manifold $\mathcal{M}_n$, where the branch points at the boundary of the spatial entangling region A induce a deficit angle $\delta = 2\pi(1-n)$ in ∂A. The holographic dual of a field theory defined on such a manifold should be constructed by solving Einstein Equations with negative cosmological constant and with boundary conditions such that the metric approaches that of $\mathcal{M}_n$ at the conformal boundary. This procedure is not solvable in general. However, we can assume that the holographic dual corresponds to a n-sheeted AdS_{d+2} with a deficit angle δ on a codimension two surface γ_A. This assumption is obvious only in three dimensional gravity, as all solutions are locally the same as AdS_3. The curvature scalar for this replicated AdS geometry contains a term with a delta function localized on γ_A:

$$R = 4\pi(1-n)\delta(\gamma_A) + R_{AdS} \tag{3.22}$$

Then the on-shell gravity action is:

$$I_{\text{grav}} = -\frac{1}{16\pi G_N^{(d+2)}}\int dx^{d+2}\sqrt{g}(R+\Lambda) + ... \tag{3.23}$$

$$= -\frac{1}{4G_N^{(d+2)}}(1-n)\mathrm{Area}(\gamma_A) - \frac{1}{16\pi G_N^{(d+2)}}\int dx^{d+2}\sqrt{g}\Lambda + ... \tag{3.24}$$

Following Equation (3.6), in the classical gravity regime the field theory partition function corresponds to $e^{-I_{\text{grav}}}$ with prescribed boundary conditions. Since this partition function is defined over the manifold $\mathcal{M}_n$, it is identified with $\mathrm{Tr}\rho_A^n$, as explained in section 2.1.3. Then the HEE proposal is obtained:

$$S_A = -\frac{\partial}{\partial n}\mathrm{Tr}\rho_A^n|_{n=1} = -\frac{\partial}{\partial n}\exp\left(\frac{(1-n)\mathrm{Area}(\gamma_A)}{4G_N^{(d+2)}}\right)_{n=1} = \frac{\mathrm{Area}(\gamma_A)}{4G_N^{(d+2)}} \tag{3.25}$$

Proof for Spherical Systems

The EE of spherical systems in the CFT ground state has been computed without assuming the Ryu-Takayanagi prescription, and, since the final result coincides with the area of the minimal RT surface, this argument is a proof of the RT formula for systems with spherical symmetry [75].

The strategy consists in, first, to exploit the conformal symmetry and use CFT methods to map the original problem to a more convenient one. Then, making use of standard holography, the EE is obtained. More explicitly, but still briefly:

The objective is to compute the EE of a spherical system A in a CFT defined on $\mathbb{R}^{(1,d-1)}$ or $\mathbb{R}\times S^{d-1}$. The key observation is that there exist appropriate maps that take the causal development of A, D_A, to $\mathbb{R}\times H^{d-1}$, where H is the hyperbolic space.[4] This transformation maps the vacuum density matrix in D_A on to a thermal density matrix in $\mathbb{R}\times H^{d-1}$. The thermal character in $\mathbb{R}\times H^{d-1}$ is demonstrated by noting that the modular flow[5] in $\mathbb{R}\times H^{d-1}$ corresponds to time translations, which must be a symmetry

[4] The metric of $\mathbb{R}\times H^{d-1}$ is written $ds^2 = -d\tau^2 + R^2(du^2 + \sinh^2 u d\Omega_{d-2}^2)$.

[5] Since the density matrix is hermitian and positive semidefinite, it can be expressed by exponentiation of some hermitian operator H_m: $\rho = e^{-H_m}$. The operator H_m is called the modular hamiltonian, and is the generator of the modular flow $U(s) = e^{-iH_m s}$.

of correlation functions. In addition, correlators must be periodic under imaginary shifts in time.

Since the original vacuum density matrix has been mapped on to a thermal one, the EE of the former is mapped to thermal entropy of the later. Then holography is used at this point to compute the thermal entropy of the space $\mathbb{R} \times H^{d-1}$, for which it is necessary to find the dual holographic spacetime. To this aim, the AdS space is foliated with hyperbolic slices. One finds that the holographic dual of a CFT on $\mathbb{R} \times H^{d-1}$ is a topological black hole in AdS[6]. According to the correspondence, the thermodynamic entropy in $\mathbb{R} \times H^{d-1}$ is the Bekenstein-Hawking entropy of the dual black hole, thus proportional to the area of its horizon. Explicitly evaluating this, one arrives to the same result that would have been obtained using the RT formula in the pure AdS space dual to the original $\mathbb{R}^{(1,d-1)}$ or $\mathbb{R} \times S^{d-1}$, as computed in section 3.3.1.

General Proof considering HEE as Generalized Gravitational Entropy

The gravitational entropy, originally introduced by Gibbons and Hawking for gravity solutions with $U(1)$ symmetry, is generalized by Maldacena and Lewkowycz for less symmetric cases [76]. For a general quantum system the density matrix can be obtained from Euclidean evolution in a given manifold B:

$$\rho = \mathcal{P} e^{-\int_{\tau_0}^{\tau_f} d\tau \; H(\tau)} \tag{3.26}$$

The n-th power of this matrix is obtained by considering the manifold B^n as that obtained by gluing together n copies of the original manifold B, and its trace is obtained by identifying the initial and final points:

$$\mathrm{Tr}(\rho^n) = \mathcal{P} e^{-\int_{\tau_0}^{\tau_0+2\pi n} d\tau \; H(\tau)} \equiv Z(n) \tag{3.27}$$

where the length of the original circle has been set to 2π and the identification $\tau \sim \tau + 2\pi n$ has been made. This expression is understood as the partition function $Z(n)$ on the Euclidean manifold B^n. Then the entropy is given by

$$S = -n \frac{\partial}{\partial n} \left(\log Z(n) - n \log Z(1) \right)_{n=1} \tag{3.28}$$

According to (3.7), the partition function is related to the on-shell gravity action I_{grav} for gravity solutions in one more dimension with prescribed boundary conditions. This gravity interpretation is used for the evaluation of (3.28), which is the main subject of [76]. For this, some obstacles are found, mainly due to the analytical continuation of solutions for non integer n. It is shown that (3.28) is given by the area of a codimension-two surface γ of the original solution (that in B). At this surface the compact direction labeled by τ smoothly shrinks to zero size. Then, one demands that the analytically extended solutions obey Einstein Equations to leading order in n-1, which is actually equivalent to impose a minimal area condition on the surface γ. Since it coincides with the Ryu-Takayanagi surface, the HEE conjecture is proven.

[6] The metric of this topological black hole is $ds^2 = \left(\frac{\rho^2}{L^2} - 1\right)^{-1} d\rho^2 - \left(\frac{\rho^2}{L^2} - 1\right) d\tau^2 + \rho^2 (du^2 + \sinh^2 u d\Omega_{d-2}^2)$

3.3 Computing Holographic Entanglement Entropy

In this section we calculate the HEE in some examples. Let us consider the metric of a $(d+1)$ dimensional asymptotically AdS space-time:

$$ds^2 = g_{\mu\nu}dx^\mu dx^\nu \tag{3.29}$$

And let the surface γ in (3.13) be parametrized with coordinates ζ^a, with $a = 1, ..., d-1$. The induced metric in γ_A is:

$$h_{ab} = g_{\mu\nu}\frac{\partial x^\mu}{\partial \zeta^a}\frac{\partial x^\nu}{\partial \zeta^b} \tag{3.30}$$

And the expression for the area is:

$$\text{Area}(\gamma_A) = \int d^{d-1}\zeta\sqrt{\det h} \tag{3.31}$$

The surface γ_A has codimension two, i.e. it has $(d-1)$ degrees of freedom ζ^a. For an arbitrary parametrization in general we need to solve $d+1$ partial differential equations for the $d+1$ functions $x^\mu(\zeta^a)$ in the $d-1$ variables ζ^a. If a number k of the spacetime coordinates themselves is used as parameters then the number of equations as well as the number of variables are reduced by k. This will be convenient for systems A with some symmetry. In addition, for static spacetimes the surface γ_A lives in a constant time slice.

In the next subsections we do some explicit calculations of the HEE for some simple systems applying usual variational methods to deal with the functional (3.31). Then, in subsection 3.3.3, another approach for extremizing (3.31) using the geodesic equation is presented together with an algorithm for numerically solving the equations.

3.3.1 HEE of the Ground State

Interval in CFT$_{1,1}$ on $\mathbb{R}\times\mathbb{R}$

In order to obtain the HEE of an interval of length ℓ in flat space ($A = \{x \mid -\ell/2 \leq x \leq \ell/2\}$), one needs to minimize curves on the AdS background in Poincaré coordinates. The curves are parametrized with $s \in [0, \pi]$. The embedding is then

$$t = t_0 \quad , \quad z = z(s) \quad , \quad x = x(s) \tag{3.32}$$

And the boundary conditions are:

$$z(0) = z(\pi) = 0 \tag{3.33}$$

$$x(0) = \ell/2 \ , \ x(\pi) = -\ell/2 \tag{3.34}$$

The Area functional for the geodesic is:

$$\text{Area}(\gamma_A) = \int ds\sqrt{\frac{x'(s)^2 + z'(s)^2}{z(s)^2}} \tag{3.35}$$

There are two conserved quantities: the conjugate momentum of x, that is p_x, and the quantity associated to invariance in s, named H:

$$p_x = \frac{\partial L}{\partial x'} = \frac{x'}{z\sqrt{x'^2 + z'^2}} \tag{3.36}$$

$$H = \frac{\partial L}{\partial x'}x' + \frac{\partial L}{\partial z'}z' - L = x'^2 + z'^2 \tag{3.37}$$

Where L is the integrand in (3.35). Using H in the first equation we obtain the equivalent system:

$$x' = p_x\sqrt{H}z \tag{3.38}$$
$$x'^2 + z'^2 = H \tag{3.39}$$

The solution for x is

$$x(s) = \left(\frac{1}{p_x} + \frac{\ell}{2}\right) - \frac{1}{p_x}\cos(\sqrt{H}p_x s) \tag{3.40}$$

Since $H = \frac{1}{p_x^2}$, then $x(s) = \left(\frac{1}{p_x} + \frac{\ell}{2}\right) - \frac{1}{p_x}\cos(s)$. With the anchoring condition on the other endpoint of the curve, $x(\pi) = -\frac{\ell}{2}$, we obtain $p_x = -\frac{\ell}{2}$. Hence, the final parametric form of the geodesic is:

$$z(s) = \frac{\ell}{2}\sin(s) \tag{3.41}$$
$$x(s) = \frac{\ell}{2}\cos(s) \tag{3.42}$$

The proper length of this curve is the on-shell functional (3.35) for this solution, which is a divergent quantity. It is regulated by restricting the integral to $s \in [\epsilon, \pi - \epsilon]$:

$$\text{Area}(\gamma_A) = \int_\epsilon^{\pi-\epsilon} \frac{ds}{\sin(s)} = 2\log\left(\frac{2}{\epsilon}\right) \tag{3.43}$$

The relation between the cut-off ϵ and the field theory cut-off a can be obtained by the IR/UV relation $z(\epsilon) = a$. Then, as $z(\epsilon) = \frac{\ell}{2}\epsilon$, we have $\epsilon = \frac{2a}{\ell}$. Also, the gravity constants are expressed in terms of the CFT constants: $c = \frac{3}{2G_N}$. The final expression for the HEE of an interval in flat space is then like the EE (2.45) computed from the replica trick:

$$S_A = \frac{\text{Area}(\gamma_A)}{4G_N} = \frac{1}{2G_N}\log\left(\frac{\ell}{a}\right) = \frac{c}{3}\log\left(\frac{\ell}{a}\right) \tag{3.44}$$

Interval in CFT$_{1,1}$ on $\mathbb{R} \times S^1$

The gravitational dual of the field theory on compact space is AdS in global coordinates:

$$ds^2 = \frac{1}{\cos^2\rho}\left(-dt^2 + d\rho^2 + \sin^2\rho d\theta^2\right) \tag{3.45}$$

Where the radial coordinate of AdS is $\rho \in [0, \pi/2]$. The objective is to obtain the HEE of an arc: $A = \{\theta \mid -B/2 \leq \theta \leq B/2\}$.To this aim, the area functional (3.31) to be minimized is:

$$\text{Area}(\gamma_A) = \int d\theta\sqrt{\sec^2\rho(\theta)(1 + \rho'(\theta)^2) - 1} \tag{3.46}$$

And one finds agreement with (2.51):

$$S_A = \frac{\text{Area}(\gamma_A)}{4G_N} = \frac{c}{3}\log\left(\frac{B}{\pi a}\sin\frac{\pi\ell}{B}\right). \tag{3.47}$$

Ball in CFT$_{1,d-1}$ on $\mathbb{R}\times\mathbb{R}^{d-1}$

We consider a higher dimensional example that has the maximum symmetry, $(d-2)$ generators. Let the system A be a ball of radius ℓ:

$$A=\mathcal{B}_{d-1}=\{x\mid \xi<\ell\} \tag{3.48}$$

Where ξ is the radial coordinate in the boundary. The AdS metric is:

$$ds^2=\frac{-dt^2+dz^2+d\xi^2+\xi^2 d\Omega^2_{(d-2)}}{z^2} \tag{3.49}$$

The surface $\gamma_{\mathcal{B}}$ is parametrized with:

$$\zeta^1=\xi\ \ ,\ \ \zeta^2=\theta_1\ \ ,\ \ \ldots\ \ ,\ \ \zeta^{d-1}=\theta_{d-2} \tag{3.50}$$

The area functional (3.31) for the surface described bythis embedding takes the form:

$$\text{Area}(\gamma_{\mathcal{B}})=\int d\xi d\Omega_{d-2}\xi^{d-2}\frac{\sqrt{1+z'(\xi)^2}}{z^{d-1}}=\text{Vol}(S^{d-2})\int d\xi\ \xi^{d-2}\frac{\sqrt{1+z'(\xi)^2}}{z^{d-1}} \tag{3.51}$$

Now for this variational problem there are no constants of motion, and we are led with a second order equation:

$$\xi z z''+(1+z'^2)((d-1)zz'+d\xi)=0 \tag{3.52}$$

Since in AdS$_3$ the minimal curves are the semicircumferences (3.41)-(3.42), we check that

$$z(\xi)^2+\xi^2=\ell^2 \tag{3.53}$$

obeys the equation (3.52). The area (3.51) is evaluated for this solution, and is solvable in terms of ordinary hypergeometric functions. The divergences structure of the area results as folllows. As expected from the area law (2.14), the most divergent term is proportional to the area of the boundary of the system: $\left(\frac{\ell}{a}\right)^{\dim(\partial\mathcal{B})}$. Also, there are subleading divergent terms with descending powers of $\left(\frac{\ell}{a}\right)^{\alpha}$, with α of the same parity as $\dim(\partial\mathcal{B})$. When this is even, the $\alpha=0$ term is logarithmic. In summary, the HEE for the ball in flat space is

$$S_{\mathcal{B}_{(d-1)}}=\begin{cases}\displaystyle\sum_{j=0}^{(\dim(\partial\mathcal{B})-1)/2} p_{2j+1}\left(\frac{\ell}{a}\right)^{2j+1}+p_0 & ,\ \text{if } \dim(\partial\mathcal{B}) \text{ odd}\\ \displaystyle\sum_{j=1}^{\dim(\partial\mathcal{B})/2} q_{2j}\left(\frac{\ell}{a}\right)^{2j}+q_{\log}\log\left(\frac{\ell}{a}\right)+q_0 & ,\ \text{if } \dim(\partial\mathcal{B}) \text{ even}\end{cases} \tag{3.54}$$

Where p_i and q_i are constants. The explicit results for the lowest dimensional case is

$$S_{\mathcal{B}_{(2)}}=\frac{1}{4G_N}2\pi\left(-1+\frac{\ell}{a}\right) \tag{3.55}$$

The universal (finite and cut-off independent) part of the EE is a constant: all the dependence of the EE on ℓ is through divergent terms.

3.3.2 HEE of the Thermal Equilibrium State

Interval in CFT$_{1,1}$ on $\mathbb{R}\times\mathbb{R}$

Let the system be $A = \{x \mid -\ell/2 \leq x \leq \ell/2\}$. The holographic dual of the thermal equilibrium state is a black hole in AdS$_3$. As the field theory is defined on a non compact space, we consider the Poincaré patch of the dual AdS spacetime. The metric is:

$$ds^2 = -(r^2 - m)dt^2 + \frac{dr^2}{r^2 - m} + r^2 dx^2 \tag{3.56}$$

An appropriate parametrization for the geodesic is the coordinate x. The curve is described by:

$$t = t_0 \quad , \quad r = r(x) \quad , \quad x \tag{3.57}$$

And the boundary condition is

$$r(\ell/2) \to \infty \tag{3.58}$$

The interval is centered around $x = 0$. Then, because of translation symmetry in x, continuity of the geodesic and the boundary conditions, the point of the curve which enters the most in AdS will be at $x = 0$. The value of r attained at this point is named r_*. Then:

$$r(0) = r_* \quad , \quad r'(0) = 0 \tag{3.59}$$

The functional (3.31) takes the form

$$\text{Area}(\gamma_A) = \int dx \sqrt{r(x)^2 + \frac{r'(x)^2}{r(x)^2 - m}} \tag{3.60}$$

As there is no explicit dependence on x in the integrand there is a conserved quantity:

$$\frac{\partial L}{\partial r'} r' - L = \frac{r(x)^2}{\sqrt{r(x)^2 + \frac{r'(x)^2}{r(x)^2 - m}}} = r_* \tag{3.61}$$

Where the last equality is obtained from the evaluation at $x = 0$. We can solve (3.61) for $r'(y)$:

$$r'(x) = r\sqrt{\left(1 - \frac{r^2}{r_*^2}\right)(m - r^2)} \tag{3.62}$$

Substituting this in (3.60) and changing of integration variable, we have an expression for the on-shell length of the geodesic in terms of r_*. The integration is performed in one half of the geodesic, from r_* to the regulator r_∞, and then the result is doubled in order to find the total area. Solving and expanding for $r_\infty \to \infty$ we have

$$\begin{aligned} \text{Area}(\gamma_A) &= 2\int_{r_*}^{r_\infty} dr \frac{r}{(r^2 - r_*^2)(r^2 - m)} = 2\log\left(1 + \sqrt{\frac{r_\infty^2 - r_*^2}{r_*^2 - m}}\right) \\ &= \log\left(\frac{r_\infty}{r_*^2 - m}\right) \end{aligned} \tag{3.63}$$

A relation between r_* and ℓ is obtained by integrating (3.62) and imposing the boundary conditions with the appropriate limits:

$$\int_{r_*}^{\infty} \frac{dr}{r\sqrt{(1-\frac{r_*^2}{r^2})(m-r^2)}} = \int_0^{\ell/2} dy \tag{3.64}$$

We obtain

$$r_* = \sqrt{m}\coth\left(\frac{\ell\sqrt{m}}{2}\right) \tag{3.65}$$

We can substitute this expression for r_* in (3.63). Also, the relation between the gravitational and the field theory regulators, $r_\infty = 1/a$, the black hole temperature in three dimensions, $\beta = 2\pi/\sqrt{m}$, and the relation between the Newton constant and the CFT central charge, $c = 3/(2G_N)$. Then, the final form of the HEE coincides with the formula (2.48) computed with the replica trick and a conformal transformation.

3.3.3 HEE and the Geodesic Equation. Relaxation Algorithm.

When the spatial region A has some symmetry, the problem can be dimensionally reduced (as many dimensions as symmetry generators the system A has). In particular, the most symmetric ($d-2$ symmetries) higher dimensional case can be translated into the problem of γ_A being a curve. This is achieved by taking some of the spacetime coordinates x^μ as parameters ζ^α, such that the system is invariant under translations in some of them, as done for a ball in $\mathbb{R}\times\mathbb{R}^{d-1}$ in section 3.3.1. The embedding $x^\mu = x^\mu(\zeta^\alpha)$ does not depend on the particular coordinates associated with the symmetries and as a consequence the integration over them in (3.31) is immediate and only one coordinate rests in the measure. In general, let the metric of an asymptotic AdS_{d+1} spacetime be written:

$$ds^2 = G_{ab}(x^0,x^1)dx^a dx^b + f(x^0,x^1)\mathcal{G}_{\alpha\beta}(x^\alpha)dx^\alpha dx^\beta \tag{3.66}$$

$$\text{With } \{a,b\}\in\{0,1\} \text{ and } \{\alpha,\beta\}\in\{2...d\}$$

Here, the pair of coordinates (0,1) expand together the timelike and radial directions of AdS, combined through a metric G_{ab}, and the other $(d-1)$ coordinates correspond to the transverse space, whose metric is denoted $\mathcal{G}_{\alpha\beta}$. Let the surface γ be parametrized by the coordinates $\{x^\alpha\}$ themselves. For the most symmetric systems the profile of the surface γ is given by:

$$x^0 = x^0(\zeta),\quad x^1 = x^1(\zeta),\quad \zeta,\quad x^3\ ,\quad ...\ ,\quad x^{d-1} \tag{3.67}$$

The advantage of taking such an ansatz is that the area functional (3.31) obtained from evaluating the induced metric (3.30) is the form:

$$\mathrm{Area}(\gamma_A) = \mathrm{Vol}(A_{\mathrm{int.sym}})\times\mathrm{Area}(\gamma_{\mathrm{geod}}) \tag{3.68}$$

Where $\mathrm{Vol}(A_{\mathrm{int.sym}})$ is the volume of the internal symmetry space and $\mathrm{Area}(\gamma_{\mathrm{geod}})$ is the length of a geodesic in a three dimensional effective metric.

This problem can be posed equivalently with the geodesic equation. The Euler-Lagrange equations obtained from extremizing $\mathrm{Area}(\gamma_A) = \int d\zeta\sqrt{\det h}$ when $\zeta = \lambda$ is taken as an affine parameter (proportional to the invariant proper distant, $\frac{ds}{d\lambda} = \text{const}$), can be put in the form:

$$\frac{d^2x^\mu}{d\lambda^2} + \Gamma^\mu_{\nu\rho}\frac{dx^\nu}{d\lambda}\frac{dx^\rho}{d\lambda} = 0\,. \tag{3.69}$$

Since the geodesic is required to get to the boundary, where the metric diverges, the affine parameter runs within $(-\infty, \infty)$ and the infinite length $\int ds = \frac{ds}{d\lambda}\int_{-\infty}^{\infty} d\lambda$ needs to be regularized. It is convenient to change λ to a new variable σ by defining the affine parameter through a function $\lambda = \lambda(\sigma)$ with σ in a finite range, $\sigma \in [-\sigma_0, \sigma_0]$, and with $\lim_{\sigma\to\pm\sigma_0} \lambda(\sigma) = \pm\infty$ and $\lambda(0) = 0$. The geodesic equation (3.69) in terms of the non affine parameter is

$$\frac{d^2x^\mu}{d\sigma^2} - \frac{\frac{d^2\lambda}{d\sigma^2}}{\frac{d\lambda}{d\sigma}}\frac{dx^\mu}{d\sigma} + \Gamma^\mu_{\nu\rho}\frac{dx^\nu}{d\sigma}\frac{dx^\rho}{d\sigma} = 0\,. \tag{3.70}$$

Let the coordinates be $\{t, r, x\}$, with the boundary of AdS located at a finite value r_{bdry} and the transverse direction x being irrespectively compact or not. If the system A is an interval of length ℓ at an arbitrary time t_0, the boundary conditions are

$$t(\pm\sigma_0) = t_0 \tag{3.71}$$

$$r(\pm\sigma_0) = r_{\text{bdry}} \tag{3.72}$$

$$x(\pm\sigma_0) = \pm\frac{\ell}{2} \tag{3.73}$$

And (3.70) is a system of second order differential equations with Dirichlet boundary conditions at both endpoints of the domain. We use a relaxation algorithm to solve it [114]. This consists in an iterative method that provides corrections $\Delta x^\mu(\sigma)$ to a given approximate solution $x^\mu(\sigma)$. Starting with a trial seed solution $x^\mu(\sigma)$, the equations for $\Delta x^\mu(\sigma)$ are found by evaluating the geodesic equations for $x^\mu(\sigma) + \Delta x^\mu(\sigma)$ and, requiring them to be zero, solve for $\Delta x^\mu(\sigma)$ the linearized equations in $\Delta x^\mu(\sigma)$. The solution is updated and this step is repeated iteratively until an accurate enough solution is found. In the discretized domain σ there is a big matrix that implements the linearization and constrains the solutions for the boundary conditions to hold. Solving for $\Delta x^\mu(\sigma)$ amounts to inverting this matrix. As it is mostly zero except for a strip around the main diagonal, it can be defined as a sparse matrix and the operation is numerically economic.

Once that a curve $(t(\sigma), r(\sigma), x(\sigma))$ has been obtained, the finite part of the length of the geodesic is computed by subtracting the appropriate divergent function f:

$$\int ds = \lim_{r\to r_{\text{bdry}}} f(r_{\text{bdry}} - r) \to \infty \tag{3.74}$$

The form of f is found from the divergent term of the corresponding pure AdS solution or solving the geodesic equations in series near the boundary. $f(y) \propto \log(y)$ for geodesics in AdS_3 and $f(y) \propto y^{-(d-2)}$ for geodesics in effective metrics dual to $(d-1)$ dimensional symmetric systems A, in agreement with the area law. The exact proportionality constants in these expressions depend on the radial coordinate used in each case. Taking a cut-off $\sigma_\infty \to \sigma_0$, the finite part of the length is obtained by subtracting this divergent term from the divergent affine parameter:

$$\text{Area}(\gamma_A)_{\text{finite}} = 2\lambda(\sigma_\infty) - f(r_{\text{bdry}} - r(\sigma_\infty)) \tag{3.75}$$

This result does not depend on the cut-off σ_∞ and its verification is a check for the consistency of the numerical solutions.

Part II

Results

4

Collapse in AdS I: Vaidya Spacetime

We focus on the duality between 2-dimensional CFTs and gravity on asymptotically AdS_3 geometries. The holographic proposal relates the entanglement entropy with the length of spacelike geodesics that anchor on the AdS boundary.

4.1 Vaidya Geometry

The Vaidya metric is a non static solution of Einstein equations that describes the collapse or evaporation of null dust. It was first found for asymptotically flat spaces [54] [55], but is easily generalizable to AdS spaces. Null dust describes incoherent radiation and is usually found in geometric optics approximations and through eikonal approximations of different types of matter. The energy-momentum tensor is given by:

$$T^{(\mathrm{nd})}_{\mu\nu} = (d-1)\frac{1}{2r^{d-1}}\frac{dm(v)}{dv}\delta_{\mu v}\delta_{\nu v} \tag{4.1}$$

Here v is a null incoming Eddington-Finkelstein coordinate and $m(v)$ is the mass function that describes the configuration of matter. A physically reasonable matter obeys the null energy condition [56], that is, $T_{\mu\nu}N^\mu N^\nu \geq 0$ for any null vector N^μ. [1] For the null dust energy momentum tensor $T^{(\mathrm{nd})}_{\mu\nu}$ this is

$$\frac{dm}{dv} \geq 0 \tag{4.2}$$

The Vaidya-AdS_{d+1} metric is the solution of the Einstein equations for a null dust stress tensor $T^{(\mathrm{nd})}_{\mu\nu}$ and with negative cosmological constant:

$$R_{\mu\nu} - \frac{1}{2}g_{\mu\nu}R + \Lambda g_{\mu\nu} = 8\pi G_N T^{(\mathrm{nd})}_{\mu\nu} \tag{4.3}$$

The metric in the Poincaré patch of AdS is written:

$$ds^2 = -\left(r^2 - \frac{m(v)}{r^{d-2}}\right)dv^2 + 2drdv + r^2\sum_{i=1}^{d-1}dx_i^2 \tag{4.4}$$

[1] This condition stands to have a definite positive energy density for every observer. In the context of holography it seems to be an essential condition for the field theory to behave properly under renormalization group flows, since this condition plays a key role in the demonstration of holographic central-charges-theorems [57].

To better interpret physically this spacetime let us set $m(v) = M = \text{cnst}$ and change to Schwarzschild coordinates (t, r) using

$$v = t + r^*(r), \quad \frac{dr^*}{dr} = \frac{r^{d-2}}{r^d - M}, \quad \lim_{r\to\infty} r^*(r) = 0 \tag{4.5}$$

Then the metric (4.4) is that of a static black hole with mass M

$$ds^2 = -(r^2 - \frac{M}{r^{d-2}})dt^2 + \frac{dr^2}{r^2 - \frac{M}{r^{d-2}}} + r^2 \sum_{i=1}^{d-1} dx_i^2 \tag{4.6}$$

Now let the mass function be a step function

$$m(v) = M\Theta(v) \tag{4.7}$$

This amounts to define the spacetime in two pieces: for $v < 0$ an empty AdS solution and for $v > 0$ a black hole as (4.6). Since v is an infalling null coordinate, at any time the region for $v < 0$ has smaller values of r than the region for $v > 0$. Thus, the surface $v = 0$ splits the spacetime such that the interior is empty AdS and the exterior is a static black hole. The surface $v = 0$ supports a collapsing infinitesimally thin shell of null matter. Let us smoothen the step in (4.7) and consider now a mass function of the form:

$$m(v) = \frac{M}{2}\left(\tanh\frac{v}{v_0} + 1\right) \tag{4.8}$$

Similarly, for $v \to -\infty$ one recovers pure AdS space, and for $v \to \infty$ a black hole solution. The variation of mass happens mostly in a region of size v_0 around $v = 0$. Thus, the Vaidya solution with a mass function as (4.8) corresponds to the collapse of a shell of null matter of width v_0 situated at $v = 0$.

Let the event horizon for the Vaidya spacetime be given by the surface $S \equiv r - r_{\text{eh}}(v) = 0$. Since it is a null surface, it holds $g^{\mu\nu}\partial_\mu S \partial_\nu S = 0$, or equivalently:

$$\frac{dr_{\text{eh}}}{dv} = \frac{1}{2}\left(r_{\text{eh}}^2 - \frac{m(v)}{r_{\text{eh}}^{d-2}}\right), \quad \lim_{v\to\infty} r_{\text{eh}}(v) = M^{1/d} \tag{4.9}$$

Where the boundary condition has been set to reproduce the asymptotic late time static black hole of mass M. The event horizon is said to have a teleological nature, that is, its dynamics is determined globally by the entire spacetime. As a consequence, it anticipates the collapse of matter and starts growing before this happens (see Figure 4.1). Local concepts of horizons can be defined using trapped surfaces [20]. These are co-dimension two closed spacelike surfaces along which the expansions along the two future directed normal null vectors are negative. We shall take the long used acceptation of *apparent horizon* as the outermost trapped surface, that is, the surface for which the expansions are $\theta_{\text{in}} < 0$ and $\theta_{\text{out}} = 0$. Singularity theorems assert that the existence of a trapped surface implies the formation of a singularity somewhere in its causal future in a finite proper time [56]. The apparent horizon is inside the event horizon as long as the spacetime is strongly asymptotically predictable [20], and, as it is shown in the Vaidya spacetime, it is an appropriate local object that signals the formation of a black hole. In this metric the expansions along the two future directed normal null vectors are

$$N_{\text{in}} = -\partial_r \ , \quad N_{\text{out}} = \partial_v + \frac{1}{2}\left(r^2 - \frac{m(v)}{r^{d-2}}\right)\partial_r \tag{4.10}$$

The normalization has been chosen such that $N_{\text{in}} \cdot N_{\text{out}} = -1$. The corresponding expansions are given by $\theta = \tilde{g}^{\mu\nu}\nabla_\mu N_\nu$, where the induced metric is $\tilde{g}_{\mu\nu} + N^{\text{in}}_\mu N^{\text{out}}_\nu + N^{\text{out}}_\mu N^{\text{in}}_\nu$. We obtain

$$\theta_{\text{in}} = -\frac{d-1}{r} \ , \quad \theta_{\text{out}} = \frac{d-1}{2}\left(r - \frac{m(v)}{r^{d-1}}\right) \tag{4.11}$$

And then the apparent horizon is then given by

$$r_h = (m(v))^{1/d} \tag{4.12}$$

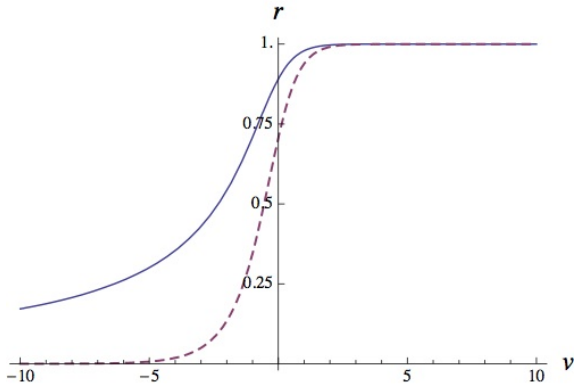

Figure 4.1: The event horizon (solid line) and apparent horizon (dashed line) for the Vaidya geometry with a mass given by (4.8) with $M = 1$. The apparent horizon responds locally to the presence of mass in the forming black hole, while the event horizon starts to grow long before.

The field theory dual to a Vaidya-AdS spacetime with a mass function such as (4.8) is described as follows. Asymptotically for $v \to -\infty$, the space is empty AdS, and for $v \to \infty$ it contains a black hole. Recalling that the coordinate v at the conformal boundary of AdS becomes the time coordinate t of the field theory, and following the holographic relations stated in section 3.1, the dual CFT state for $t \to -\infty$ is identified with the CFT ground state, and for $t \to \infty$ with a thermal equilibrium state at the same temperature than the black hole. Hence, the dynamical process in between is describing the perturbation of the CFT vacuum and relaxation to an equilibrium state. In order to confirm this expectation, we need to measure some observables along the dynamical process and compare their values with those obtained in the vacuum and in thermal equilibrium, as we shall do with the HEE.

The form of the Vaidya mass function $m(v)$ encodes the way the perturbation which takes the field theory out of equilibrium acts. For a step function as (4.7) the perturbation happens instantly at $t = 0$ in the field theory. This is dual to the instantaneous quantum quench of [5] introduced in section 2.2.2. For a mass function that varies during some finite time extent v_0, as it is the case of (4.8), the dual process is a *smooth* quench in which the change of the quench parameter does not occur suddenly but within a time extent of order v_0, that is, the CFT, starting in the ground state, suffers around $t = 0$ and during a time of order v_0 a translationally invariant perturbation that injects some energy density which triggers the evolution.

In the following sections we shall perform these computations for the three dimensional case:

$$ds^2 = -(r^2 - m(v))dv^2 + 2drdv + r^2dx^2 \tag{4.13}$$

Thus, we shall study holographically the equilibration dynamics of a CFT defined on $\mathbb{R}^{1,1}$. The inverse temperature for this metric is $\beta = 2\pi/\sqrt{m}$.

The asymptotic behavior of the metric allows to obtain the dual field theory stress-energy tensor, which is obtained by varying the gravitational action, properly regularized, with respect to the boundary metric [58]. The non trivial components of the CFT stress tensor correspond to the field theory energy density ϵ and pressure p. We obtain that both are equal to the bulk mass function:

$$\epsilon(t) = p(t) = m(t) \tag{4.14}$$

4.2 Geodesics

Let the entangling system A be an interval of length ℓ in $x \in [0, \ell]$. Parametrizing the surface γ_A with this coordinate x, the geodesics are defined by $(v(x), r(x))$. With these conventions, the length functional (3.31) is

$$\text{Area}(\gamma_A) = \int dx \sqrt{r^2 + 2r'v' - (r^2 - m(v))v'^2} \tag{4.15}$$

Following the methods introduced in section 3.3 one observes that the second order Euler-Lagrange system can be reduced introducing the conservation equation associated to invariance in x. Introducing the constant r_*, we write the constancy of $\sum_i p_i q_i' - L$ as

$$\frac{r^4}{r_*^2} = r^2 + 2r'v' - (r^2 - m(v))v'^2 \tag{4.16}$$

And we may reduce the second order equations to

$$r^2 - r^2v'^2 - rv'' + 2v'r' = 0 \tag{4.17}$$

The system (4.16)-(4.17) is supplemented with equal-time and fixed-end boundary conditions. For an interval of length ℓ at boundary time t the associated curve is such that

$$r(0) = r(\ell) \to \infty \tag{4.18}$$

$$v(0) = v(\ell) = t \tag{4.19}$$

Because of translation symmetry of x, continuous curves are symmetric with respect to $x = \ell/2$, where $r'(\ell/2) = v'(\ell/2) = 0$. Evaluating (4.16) in that point we find that r_* is the deepest value of r.

Equation (4.16) implies that the length (4.15) of the minimal curves has the form

$$\text{Area}(\gamma_A)(\ell, t) = \frac{2}{r_*}\int_0^{\ell/2} dx\ r(x)^2 \tag{4.20}$$

This expression is infinite due to the diverging metric close to the boundary. A finite part $\tilde{\mathcal{A}}_\gamma$ is extracted by removing the divergence that arises in the asymptotics of the AdS geometry:

$$\tilde{\mathcal{A}}_\gamma = \frac{2}{r_*}\int_\epsilon^{\ell/2} dx\ r(x)^2 - 2\log r(\epsilon) \tag{4.21}$$

In order to find the solutions, the problem (4.16)-(4.19) is integrated numerically (we set $M = 1$). First we solve the equations in a power series at $x = 0$ close to the boundary:

$$x \approx \frac{r_*}{2r^2} \tag{4.22}$$

$$v \approx t - \frac{1}{r} + \frac{b}{2r^2} \tag{4.23}$$

Where the integration constants r_* and b are fixed by requiring that the boundary conditions (4.18) and (4.19) hold at $x = \ell$. This requires $b = 0$ for both the cases of pure AdS and Schwarzschild-AdS, but for Vaidya it takes values in $[0, 1]$, as it is shown in Figure 4.2.

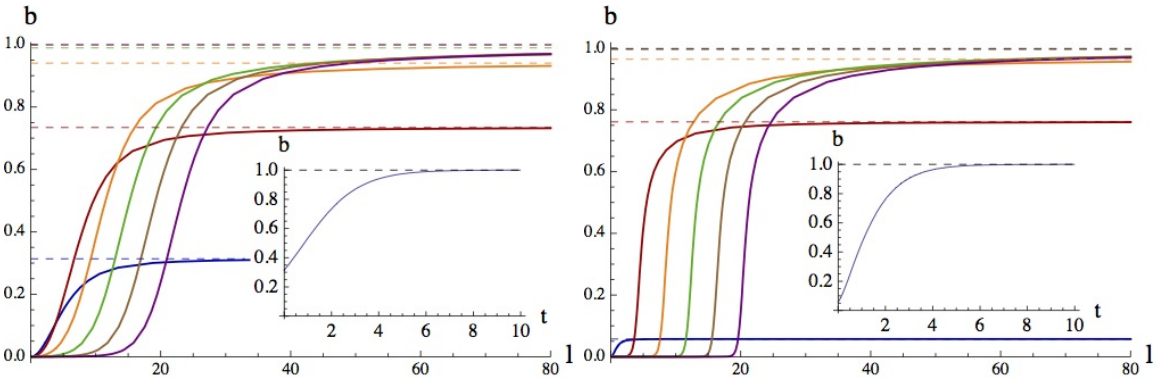

Figure 4.2: Value of b in (4.23) as a function of ℓ for $t = 0, 2, .., 10$ (solid lines) and its asymptotic value b_∞ for $\ell \to \infty$ (dashed lines). The time evolution of b_∞ is plotted in the inset. Left and right figures correspond to $v_0 = 2$ and $v_0 = 1/3$ respectively .

The search for the appropriate b that makes all boundary conditions hold is implemented with a shooting method, in which we fix the time t and use (r_*, b) as inputs. At $x = 0$ the boundary conditions are automatically fulfilled, because of construction of the power series solution (4.22)-(4.23). The value of r_* determines the associated interval length ℓ and the value of b determines the time t reached at the other end of the curve, at $x = \ell$. We demand that the boundary times at both ends are the same, so the boundary conditions (4.18) and (4.19) hold. Therefore we shoot with the variable b to find curves that verify the boundary conditions. Once the correct b has been found for each curve, the geodesic is completely determined, and we can extract the boundary parameters (t, ℓ).

The shape of the geodesics can be examined in Figure 4.3, where some curves have been plotted at a given time. We note that the maximum value of v corresponds to t, that is, all the curves extend to decreasing values of v as they penetrate into the bulk, which corresponds to longer intervals. The dependence of v_*, the minimum value of v, with the size of the interval is plotted in Figure 4.4, and it is monotonically decreasing. This implies that at any time t there will be long enough intervals with geodesics able to probe the whole collapse process.

We can differentiate three regimes. There are curves in the asymptotic region where the only relevant curvature is due to the AdS space, and hence these curves are similar to geodesics in pure AdS. These correspond to small intervals. Bigger ones, as the light green in the Figure 4.3, have their associated geodesics extending almost attached and parallel to

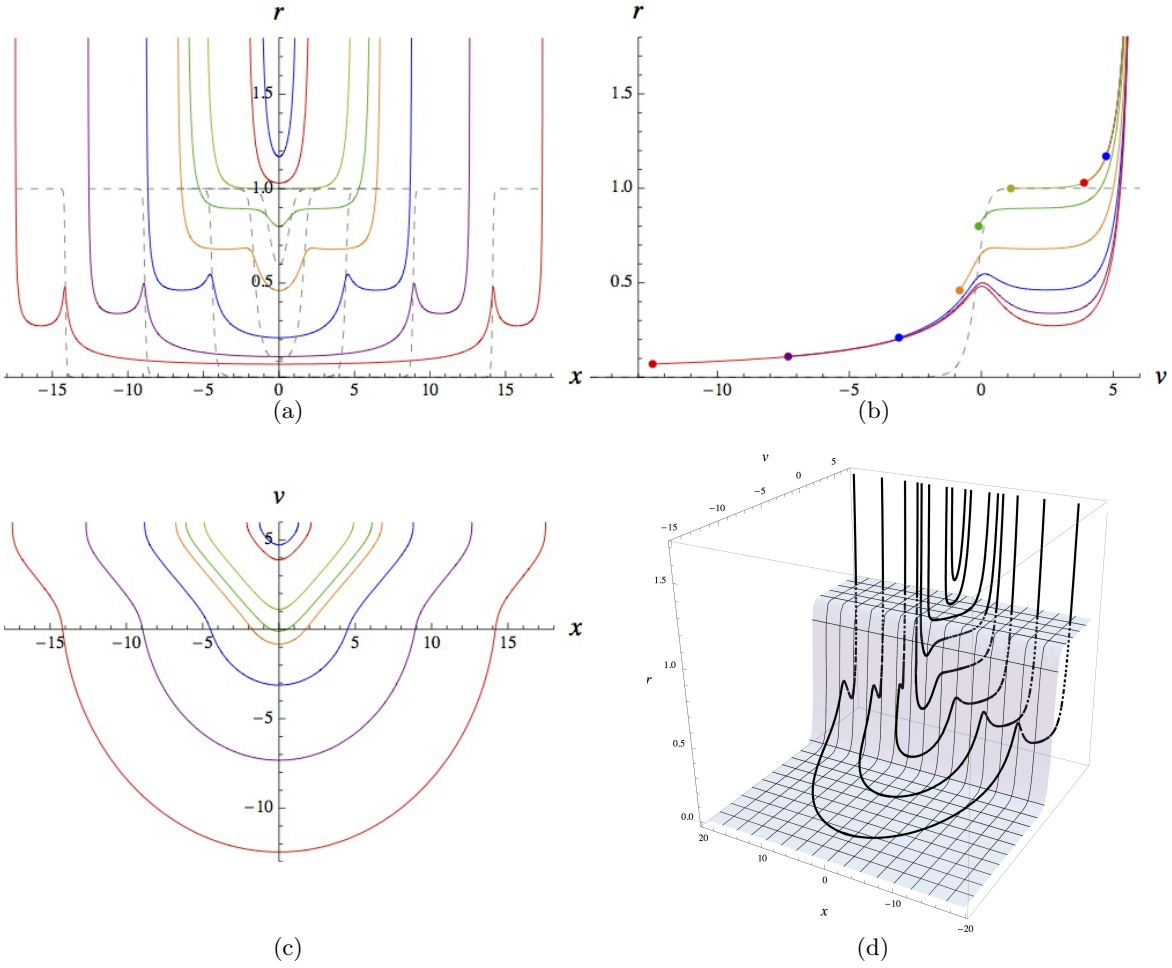

Figure 4.3: Profile of geodesics for different ℓ at $t=6$ and $v_0=1/3$. Projection into the (a) $r-x$ plane, (b) $r-v$ plane and (c) $v-x$ plane. (d) Full profile of the geodesics. The dashed line in (b) and the shaded surface in (d) signal the location of the apparent horizon. In (a) the dashed lines represent the position of the apparent horizon at the value of v defined by the trajectory of each geodesic: $\sqrt{m(v(x))}$.

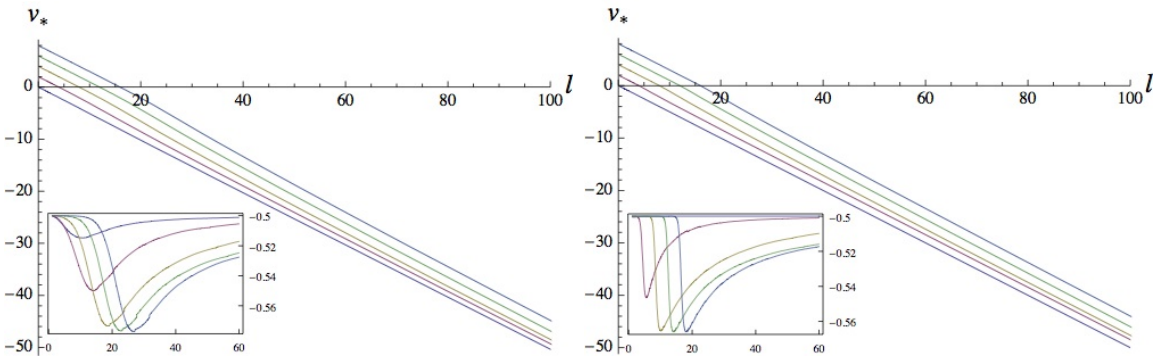

Figure 4.4: For $t = 0, 2, .., 10$, value of v_* as a function of the interval size ℓ, and in the inset its derivative $\partial_\ell v_*$. Left and right figures correspond to $v_0 = 2$ and $v_0 = 1/3$ respectively .

the horizon, which in this regime has already acquired its final value. Curves in this regime are responsible for the extensive dependence of the EE. Finally, the associated geodesics of longer intervals penetrate both the event and apparent horizons at some $v > 2v_0$ and exit at around $v \approx 0$.

The onset of the second regime can be estimated by demanding that v_* is above $\sim 2v_0$, which is when the black hole is approximately completely formed. When this holds, the curves are in the region of space where the metric is effectively like a static black hole, and we can solve (4.5) to write the relation between v, t and r:

$$v = t - \frac{1}{2\sqrt{M}} \log \frac{r + \sqrt{M}}{r - \sqrt{M}} \tag{4.24}$$

The relation between l and r_* for geodesics in the Schwarzschild-AdS metric is obtained from (3.65):

$$\ell = \frac{1}{\sqrt{M}} \log \frac{r_* + \sqrt{M}}{r_* - \sqrt{M}} \tag{4.25}$$

From these two expressions we derive

$$\ell = 2(t - v_*) \tag{4.26}$$

Hence we obtain that $v_* > 2v_0$ for

$$\ell < 2(t - 2v_0) \tag{4.27}$$

We note that this is consistent with the limits established in the quantum quenches reviewed in section 2.2.2. In fact, this simple relation (4.27), which determines the intervals at a given time for which the associated geodesics stay in the static black hole part of spacetime, determines the horizon region of the horizon effect characteristic of quantum quenches.

The bound (4.27) is not enough to produce an extensive dependence in the EE. The EE in thermal equilibrium (2.48) is extensive only for sizes $\ell \gtrsim \beta/2$. Compatibility with (4.27) implies that a clear extensive regime for the EE is not established before

$$t_{\text{ext}} \approx \beta/4 + 2v_0 \tag{4.28}$$

In Figure (4.5) it is shown the space derivative of Area(γ_A) for two different quenches. The effect of the quench time extent v_0 is manifest.

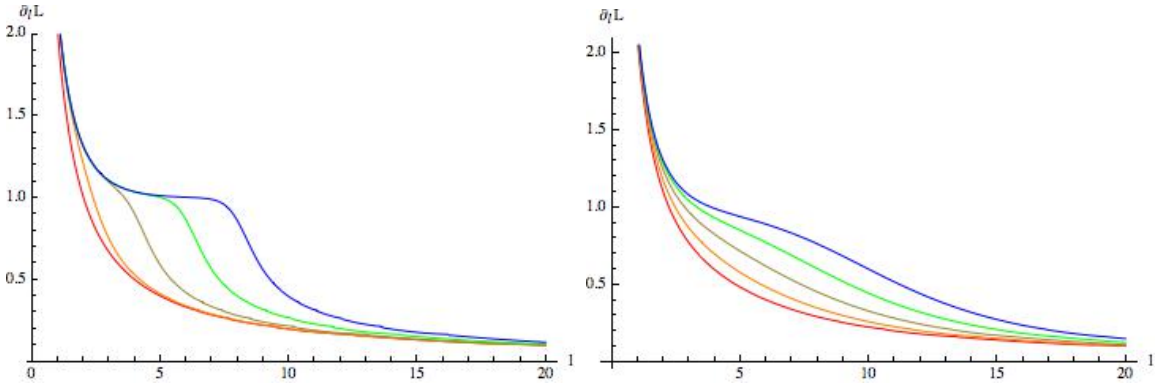

Figure 4.5: Plots of $\partial_\ell \text{Area}(\gamma_A)$ for $t = 0, 1, 2, 3, 4$. Left and right plots correspond to $v_0 = 1/3$ and $v_0 = 2$ respectively. The time t_{ext} in (4.28) is that for which a horizontal piece is appreciated in these curves. The influence of the parameter v_0 in t_{ext} is clear from these plots.

4.3 Holographic Entanglement Entropy

The description of the spacelike geodesics obtained in the Vaidya metric allows inferring the behavior of the HEE, which is proportional to the length of the corresponding geodesic. Explicitly, the dependence of Area(γ_A) on ℓ and t is shown in Figures 4.6. The entropy as a function of ℓ for different times presents three different behaviors, in correspondence with the three regimes of geodesics discussed in section 4.2.

For small ℓ the HEE has a logarithmic dependence at all times, matching the form (2.45) of the EE of the ground state. From the field theory point of view this happens for intervals smaller than the scale of thermal excitations, $\ell \lesssim \beta$. This bound in the gravity side determines interval sizes whose associated geodesic stay close enough to $r \to \infty$ such that the effective geometry is pure AdS.

For larger intervals the HEE matches the EE of the thermal state (2.48), with an extensive dependence given by $S \sim \frac{\pi c}{3\beta}\ell$. This is in correspondence with geodesics in the second regime and happens up to

$$\ell \lesssim 2(t - 2v_0) \ , \tag{4.29}$$

For even larger intervals ($\ell \gtrsim 2(t+2v_0)$) the HEE abandons the linear growth and returns to a logarithmic dependence on ℓ. The dual geodesics are those which enter in the region behind the horizon for v approximately in $[0, t]$. These geodesics also contain a portion in the $v < 0$ part, since $v_* < 0$. The form of the metric in the $v < 0$ region translates into the logarithmic behaviour of the HEE in this regime.

For asymptotically large intervals we can show that in the limit $\ell \to \infty$:

$$S(\ell, t) \to s(t) + \frac{c}{3} \log \frac{\ell}{\epsilon} \tag{4.30}$$

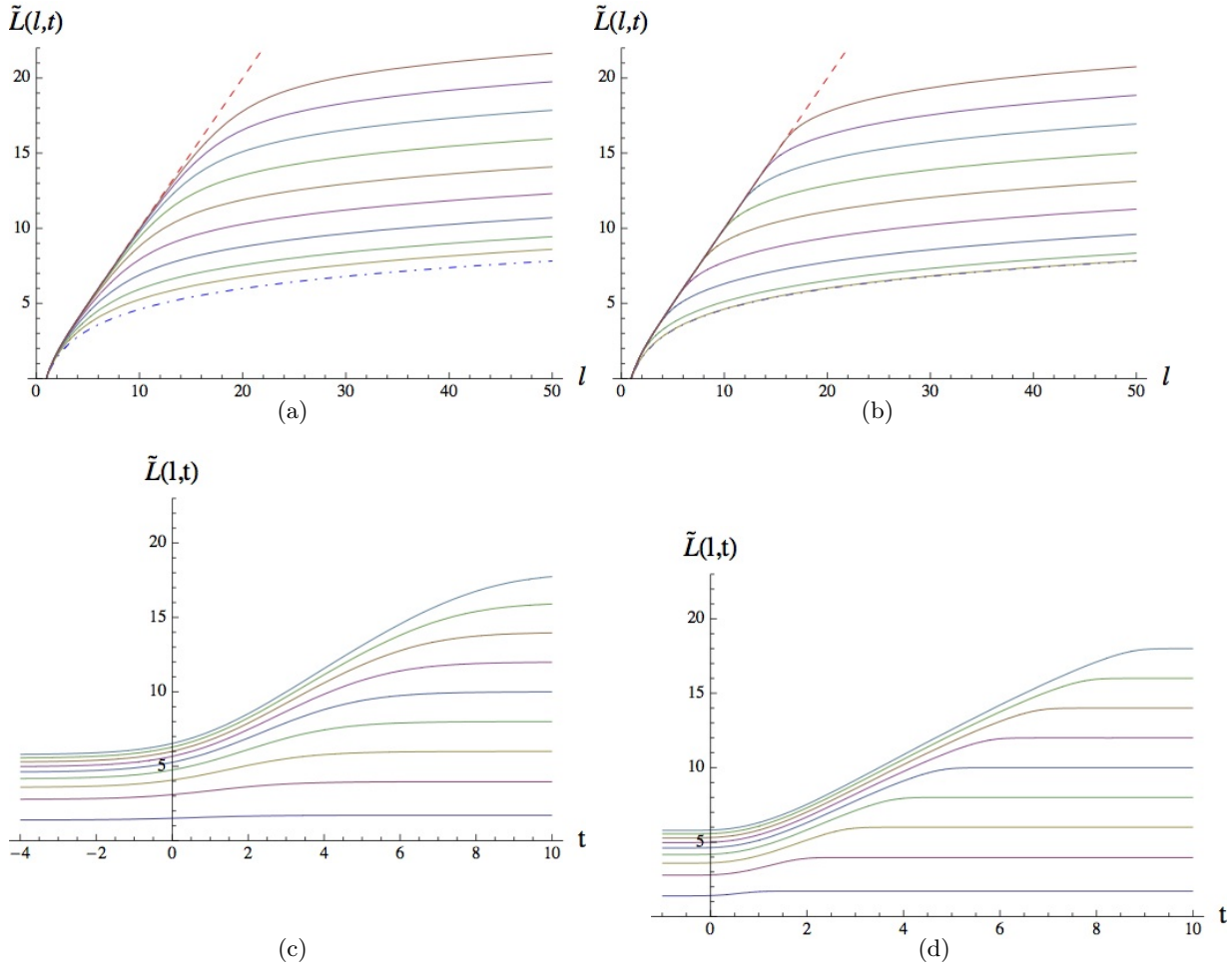

Figure 4.6: Top Figures: Finite part of the length of the geodesics as a function of ℓ for fixed times $t = 0, 1, ..., 8$ for $v_0 = 2$ (left) and $v_0 = 1/3$ (right). The dashed line corresponds to the thermal equilibrium (2.48) and dot-dashed line to the vacuum (2.45). Bottom Figures: Finite part of the length of the geodesics as a function of t for fixed interval sizes $\ell = 2, 4, ..., 18$ for $v_0 = 2$ (left) and $v_0 = 1/3$ (right). Both figures show clearly the horizon effect and the effective thermalization typical of quantum quenches.

Where the function $s(t)$ depends on the perturbation and has its holographic origin in the behind-the-horizon region of space. This function can be computed numerically. The limit $l \to \infty$ corresponds to $r_* \to 0$. Let us define $\tilde{x} = x/r_*$ and express the functions r and v in terms of it: $r = r(\tilde{x})$, $v = v(\tilde{x})$. Inserting these expressions in the equations of motion (4.16)-(4.17), and in the limit $r_* \to 0$, we obtain the equations for the infinite geodesics:

$$r^4 = 2r'v' - (r^2 - m(v))v'^2 \tag{4.31}$$

$$2v'r' - r^2v'^2 - rv'' = 0 \tag{4.32}$$

As in this limit the focus is on an end of the geodesic, boundary conditions at both ends of the curve cannot be imposed simultaneously. The conditions $r(0) \to \infty$ and $v(0) = t$ are then supplemented with the requirement that the geodesic asymptotes to a fixed time geodesic in pure AdS at $r \to 0$. This demand is sufficient to shoot the remaining integration constant and completely determine the curve.

The function $s(t)$ in (4.30), being the difference in entropy relative to that of the ground state, is then computed from the regularized length of the infinite geodesic by

$$s(t) = \frac{1}{4G_N}\left(\tilde{\mathcal{A}}_{\gamma,\infty} - 2\log\frac{\ell}{\epsilon}\right) = \frac{1}{2G_N}\left(\int_\epsilon^\xi d\tilde{x}\; r(\tilde{x})^2 - \log\frac{r(\epsilon)}{r(\xi)}\right) \tag{4.33}$$

The last term stands for two subtractions: one is the usual definition of the finite part of the entanglement entropy via an ultraviolet cutoff $\epsilon \to 0$. The other corresponds to the ground state EE, which is related to the large part of the geodesic in the $v < 0$ pure AdS zone. Hence (an arbitrary) ξ is chosen in this region. The value of $s(t)$ is independent of both the UV cutoff and ξ.

Plots for $s(t)$ for perturbations with different values of v_0 are shown in Figure 4.7. The main feature of this function is that after some time it is a linear function in t with twice the slope than what the entropy in thermal equilibrium (2.48) has in ℓ.

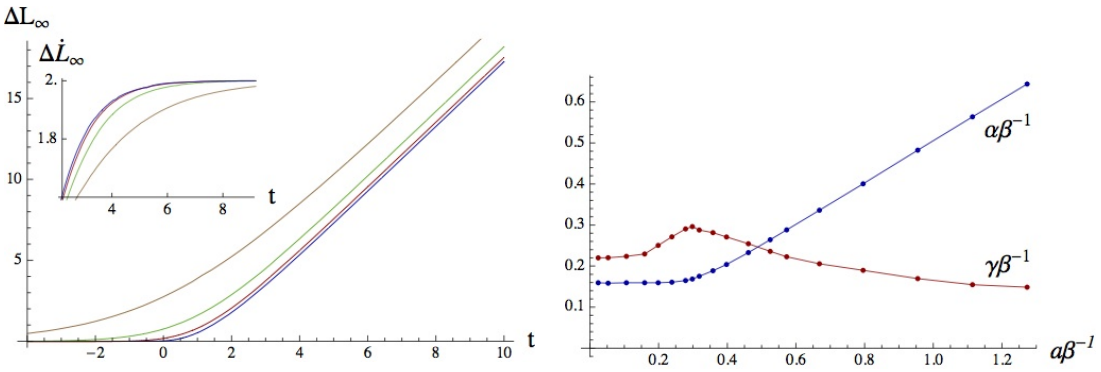

Figure 4.7: Left: Finite part of the length of the asymptotic geodesics, $\Delta L_\infty(t) = 4G_N s(t)$, with $s(t)$ given in (4.33), for $v_0 = 1/3, 1, 2, 4$, and on the inset its time derivative. As in previous figures, $\beta = 2\pi$. Right: The fitting parameters of formula (4.34), expressed through the dimensionless quotients $\alpha\beta^{-1}$ and $\gamma\beta^{-1}$ as a function of $v_0\beta^{-1}$.

Since the mass function $m(v)$ asymptotes with exponential tails associated to the tanh function, we find that the function $s(t)$ fits well to a linear plus an exponential term of the form

$$s(t) = \frac{\pi c}{3\beta}\left(2t + \alpha e^{\frac{\gamma - t}{\alpha}}\right) - s_0 \tag{4.34}$$

The dependence of α and γ on v_0 is plotted in Figure 4.7. We see that for slow perturbations, when $v_0 \gtrsim 0.5\beta$, the width α of the exponential term in (4.34) is $\alpha = v_0/2$ and the parameter γ tends to a constant. For rapid quenches, $v_0 \lesssim 0.2\beta$, both α and γ tend to constant values. We shall be interested below in the time $\bar{t}$ for which $s(t)$ behaves (practically) linearly. To have a notion of this timescale, we require that the exponential term in (4.34) is not greater than a 1% of the linear term in t. This implies

$$\bar{t} = \gamma + 4\alpha \tag{4.35}$$

For sudden quenches, $v_0 \lesssim 0.2\beta$, we have

$$\bar{t} \approx 0.85\beta \tag{4.36}$$

The fact that (4.36) is independent of the time extent of the perturbation suggests that it has a meaning as a characteristic timescale for the evolution of the holographic quenched system. Note that $\bar{t}$ occurs latter than t_{ext}, the time in (4.28) at which the finite piece of the entanglement entropy starts exhibiting an extensive regime. For slow quenches, when $v_0 \gtrsim 0.5\beta$, the threshold time $\bar{t}$ for the linear growth of $s(t)$ is governed by the time extent of the perturbation v_0, and $\bar{t} \approx t_{\text{ext}}$.

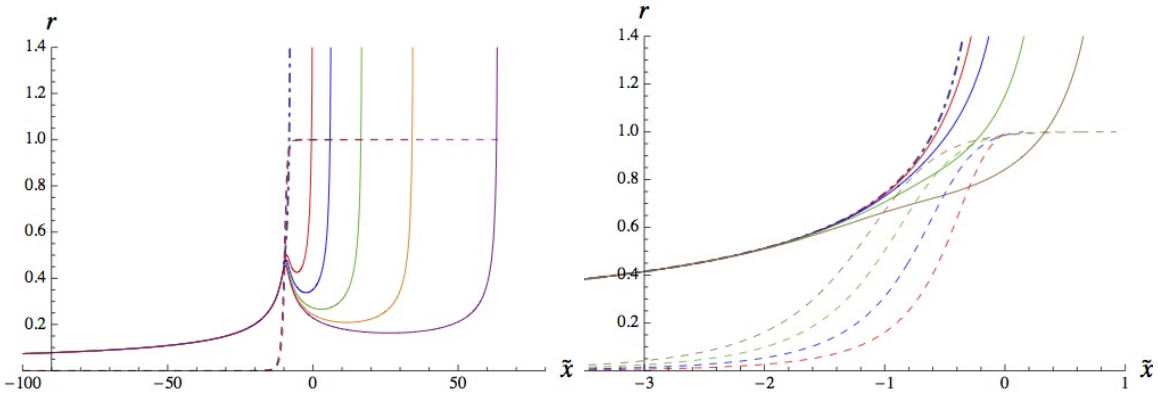

Figure 4.8: Left: Radial projection of the infinite interval geodesics as a function of the rescaled variable $\tilde{x}$ for $a = 1/3$ and $t = 3, 3.5, 4, 4.5, 5$ from left to right. The dashed lines represents the position of the apparent horizon as seen by each curve, and practically coincide for all these geodesics. The dot-dashed line corresponds to the infinite AdS_3 geodesic. Right: Infinite interval geodesics for $a = 1/3$ at $t = 0.8, 1, 1.4, 1.7$ from left to right, and the projection of the apparent horizon in the same color than the associated geodesic . The dot-dashed line corresponds to the infinite AdS_3 geodesic.

To complete the analysis, we consider the early time behavior of the geodesics. Contrary to what happens for $t > t_{\text{ext}}$, at early times the geodesics enter the black hole formation region without necessarily reaching the apparent horizon. Moreover, there is a threshold time before which geodesics stay always outside. This happens after the onset of the perturbation. Taking as an example $\beta = 2\pi$ and $a = 1/3$, from Figure 4.8 we observe that geodesics of any length stop crossing the apparent horizon before $t \approx 1.4$, well after the perturbation has ended. At that time $S(\ell, t)$ already differs appreciably from the vacuum result, with $s(t)$ being of order $c/6$ as can be seen in Figures 4.6. Although the apparent horizon is not a necessary ingredient in the holographic derivation of the EE, its role in

it could indicate how much information it encodes about the entanglement properties of the field theory. An important related question is whether the apparent horizon can be of relevance to define a notion of field theory entropy in far from equilibrium situations [4] [59]. Contrary to the case of the event horizon in static backgrounds, we have seen that the apparent horizon does not act as a wall for the geodesics involved in the calculation of the entanglement entropy. However for $t > t_{\text{ext}}$ it strongly influences the geodesic shape and length, with $s(t)$ measuring the geodesic segment behind it. Not even this applies in the early, far from equilibrium stages of the evolution, when the apparent horizon does not seem to play a role in what regards the holographic derivation of the entanglement entropy.

We note that the length of spacelike geodesics, besides as entanglement entropy for the case of AdS_3, can be related to two point functions of field theory operators with large conformal dimension, as stated in section 3.1. For these reduced set of two-point functions, the analysis of geodesics in the Vaidya model is consistent with the results for the evolution of two point functions after a quantum quench in a CFT_{1+1} [34] [35].

4.3.1 Comparison with Quantum Quenches

The results for the holographic entanglement entropy in the Vaidya geometry show agreement with the studies of quantum quenches in CFT computed in [5] and reviewed in section 2.2.2. As a function of the size of the system, the entanglement entropy is extensive for small intervals, those with $\ell \lesssim 2t$, while for big intervals, with $\ell \gtrsim 2t$, it has the same dependence on ℓ as the entanglement entropy of the ground state has. Alternatively, as a function of time, after some short initial transient time, the entanglement entropy grows linearly with time until $t \approx \ell/2$, when the final constant value, equal to the value of the thermal entropy, is reached.

However, there are two differences between the Vaidya setup and the quantum quenches of section 2.2.2. First, the sudden change in the dynamics happening in a quantum quench occur instantaneously, so it should be modeled by a Vaidya geometry in which the mass function is a Heviside step function as in (4.7). This corresponds to taking $v_0 \to 0$ in (4.8), the thin shell limit [79]. The non zero v_0 in the present work has the effect of delaying the saturation time: the perturbation does not happen entirely at $t = 0$, but it is not until $t \approx 2v_0$ that the most part of it has acted. Then the saturation does not occur abruptly at $t \approx \ell/2$ but starts approximately at $t \approx \ell/2 - 2v_0$ and by $t \approx \ell/2 + 2v_0$ has practically reached the final value.

The other difference is in the dependence on ℓ for $\ell \gtrsim 2(t+2v_0)$, and has its origin in the form of the initial state. While in [5] it is the ground state of a gapped theory with mass gap $m_0 \sim \tau_0^{-1}$, in this holographic construction the initial configuration is effectively the pure AdS geometry, which is dual to the ground state of a CFT. The entanglement pattern differs between these two situations. The gapped system does not have long range entanglement (for distances larger than the correlation length $\sim \tau_0$ the entanglement entropy is constant), while the conformal case implies long range entanglement with logarithmic dependence on the size ℓ. As a result, in the Vaidya model the entanglement entropy for $\ell \gtrsim 2(t+2v_0)$ does not saturate to a constant value, but recovers the logarithmic behaviour of the initial state.

4.4 Propagation of Entanglement

The extensive behavior of the EE for $\ell \leq 2t$ and its saturation to a constant for $t \geq \ell/2$ after a quantum quench lead to the important conclusion that entanglement propagates in a CFT_{1+1} with velocity $v_E = 1$ [5]. This causal propagation at a finite speed is responsible for the appearance of the horizon effect. The Vaidya model of collapse allows for the holographic check of this property in an equilibration process with initial long range entanglement.

Concerning the evolution of the HEE, we note that for asymptotically large intervals, for which (4.30) holds, the next relation is always fulfilled:

$$\left(2\frac{\partial}{\partial \ell} + \frac{\partial}{\partial t}\right)(S(\ell,t) - s(t)) = 0 \tag{4.37}$$

However, the domain of validity of this expression is enhanced to the regimes where $s(t)$ and $S(\ell,t)$ are linear functions of t and ℓ respectively (being the slope of the former twice that of the later). This is actually the case for $t \gtrsim \bar{t}$, as shown in section 4.3, and for $\ell \gtrsim \beta/2$, as can be seen in Figure 4.9.

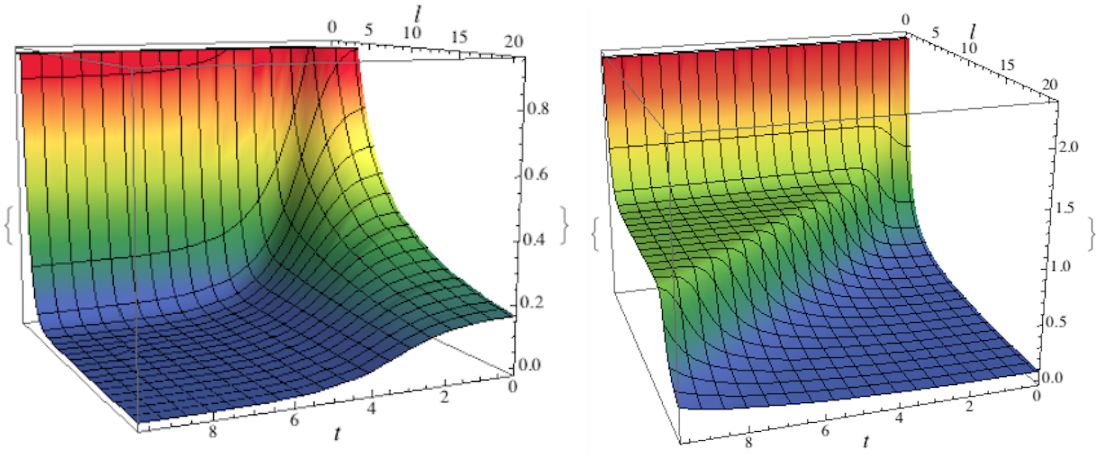

Figure 4.9: Left: Evaluation of the lhs of (4.37) for $a = 1/3$ and $\beta = 2\pi$. Right: Plot of $\partial_\ell L$ for $a = 1/3$ and $\beta = 2\pi$. The time of the onset of the plateau corresponds with t_{ext}. It is clear that $\bar{t} > t_{\text{ext}}$, as explained in the text.

Integrating (4.37) we have

$$S(\ell,t) = f(\ell - 2t) + s(t) \tag{4.38}$$

For all $t > \bar{t}$ and $\ell > \beta/2$, and in particular for the horizon region $\ell \approx 2t$, where the entanglement entropy changes from the extensive to the logarithmic behavior. This implies that after $\bar{t}$ a regime of steady evolution has been achieved, in which the only change of $S(\ell,t)$ around $\ell \approx 2t$ is a linear increase with time described by the function $s(t)$. Reproducing the extensive regime of the entanglement entropy (2.48) determines

$$f(x) = \frac{c}{3}\log\frac{\beta}{2\pi a} + \frac{\pi c}{3\beta}x + s_0 \ , \ \text{for} \ \ x < -4v_0 \tag{4.39}$$

And for large positive values of x the function f develops a logarithmic dependence for consistency with (2.48):

$$f(x) \approx \frac{c}{3} \log \frac{x + x_0}{a} \ , \text{ for large } x \tag{4.40}$$

Expression (4.38) also applies to the evolution after a quantum quench as in [5], with the only difference that $f(x) = 0$ for $x > 0$ and (4.39) holds for $x < 0$. The analysis of quantum quenches performed in [1] requires $t, \ell >> \tau_0 \approx \beta_{\text{eft}}$ and hence is valid for times well after the analogue of $\bar{t}$ and intervals over the threshold for extensive behavior. This is consistent with the regime of validity of (4.38). In this way we found not only a qualitative but also quantitative agreement between the evolution of EE in critical quantum quenches and in the holographic model. The fact that they correspond to quite different type of perturbations strongly supports that a very generic behaviour for the EE of 2-dimensional CFTÕs holds even in time dependent situations.

4.4.1 Unitary Evolution

As discussed in section 2.2.4, because the quantum mechanical evolution e^{-iHt} is manifestly unitary, a full understanding of the appearance of thermal values associated to macroscopic observables is still a challenge. Nevertheless, one can show holographically through the HEE that the evolution is unitary.

For a pure state, the EE of a subsystem A equals that of its complement:

$$S_A = S_{\bar{A}} \tag{4.41}$$

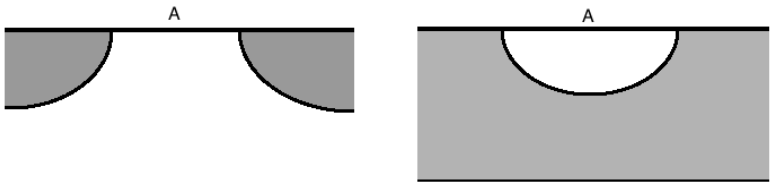

Figure 4.10: The two possible candidates for the minimal surface associated to the HEE of $\bar{A}$.

Contrary to what happens for the computation of S_A, for $S_{\bar{A}}$ there are two possible choices for the holographic surface, consistent with the requirement of being homologous to the spatial region $\bar{A}$ (the bulk surface together with the subsystem itself define the boundary of some volume in the bulk). These are shown in Figure 4.10. Taking the interval A, the first possibility is a geodesic with the same boundary conditions (4.18) and (4.19) but extending to $x \to \pm\infty$. The other one is then the preferred configuration as long as it is finite, and consists in two disjoint pieces: a geodesic joining the boundaries of $\bar{A}$, which is the same whose length gives S_A, and another geodesic extending in $x \in (-\infty, \infty)$ without reaching the AdS boundary. Such a curve is given by

$$r = 0, \quad v \to -\infty \tag{4.42}$$

Since at $v \to -\infty$ the mass is zero there is no singularity and the geodesic can step on $r = 0$. Evaluating (4.15) we find that this solution has zero lenght. As a result, the

entaglement entropy of $\bar{A}$ is the same as that of A, and the state is pure at all times in agreement with a unitary evolution.

One can show that a similar selection happens for empty AdS when the system is considered as the appropriate limit of two disjoint pieces $[u_1, u_2] \cup [w_1, w_2]$. For this case the competition between the two possibilities depends on the dimensionless ratio

$$x = \frac{(w_1 - u_1)(w_2 - u_2)}{(u_2 - u_1)(w_2 - w_1)} \tag{4.43}$$

In such a way that for $x < 1/2$ the disconnected configuration is preferred, while for $x > 1/2$ it is the other, as shown in [60]. The limits $u_1 \to -\infty$, $v_2 \to \infty$ imply $x \to 1$.

4.5 HEE in Higher Dimensions: Disk in CFT_{2+1}

In this section we present the numerical results describing the evolution of the HEE in a higher dimensional case. Originally, after the publication of [1], we further exploited the Vaidya model to compute the evolution of the HEE after a quantum quench for disks and strips in CFT_{2+1} and CFT_{3+1}. However, before this work was entirely completed, these results were published in a very interesting paper [77]. Later, the phenomenology associated to the equilibration of higher dimensional systems after a quantum quench was modelled by the so called tsunami picture [61], which essentially follows the quasiparticle picture interpretation and extends it to higher dimensions. The objective of this section is to present some of these results.

We study the evolution of the HEE after a global quench in a CFT_{2+1}. The spatial entangling system to consider is a disk of radius ℓ:

$$A = \{x \ | \xi \leq \ell\} \ , \tag{4.44}$$

Where ξ is the radial coordinate in the boundary. We consider that the field theory undergoes a global quantum quench as described in this section for the (1+1)-dimensional case. The gravitational dual is provided by a four-dimensional Vaidya-AdS metric. Using the same bulk coordinates that in (4.4), the metric is written:

$$ds^2 = -\left(r^2 - \frac{m(v)}{r}\right) dv^2 + 2drdv + r^2 \left(d\xi^2 + \xi^2 d\phi^2\right) \tag{4.45}$$

The mass function $m(v)$ is taken as in (4.8):

$$m(v) = \frac{M}{2}\left(\tanh\frac{v}{v_0} + 1\right) \tag{4.46}$$

As explained in section 3.3, and due to the spherical symmetry of the system, a convenient choice consists in parametrizing the RT surface γ_A in terms of ξ:

$$v = v(\xi) \ , \ r = r(\xi) \ , \ \xi \tag{4.47}$$

For which the boundary conditions are

$$v(\ell) = t \ , \ r(\ell) \to \infty \tag{4.48}$$

For this metric the functional (3.31), which gives the area of the surface γ_A, is:

$$\text{Area}(\gamma_A) = 2\pi \int d\xi \; \xi \sqrt{r\left(2rr'v' + m(v)v'^2 - r^3(v'^2 - 1)\right)} \tag{4.49}$$

The equations of motion derived from extremizing (4.49) are solved numerically. Once they are found, evaluating (4.49) on-shell gives the (divergent) area of γ_A. The finite cut-off independent part is obtained by subtracting the appropriate divergent term, which is found by computing the EE for the same system in the ground state, as done to arrive to (3.55), where the result was $2\pi\ell/a$.

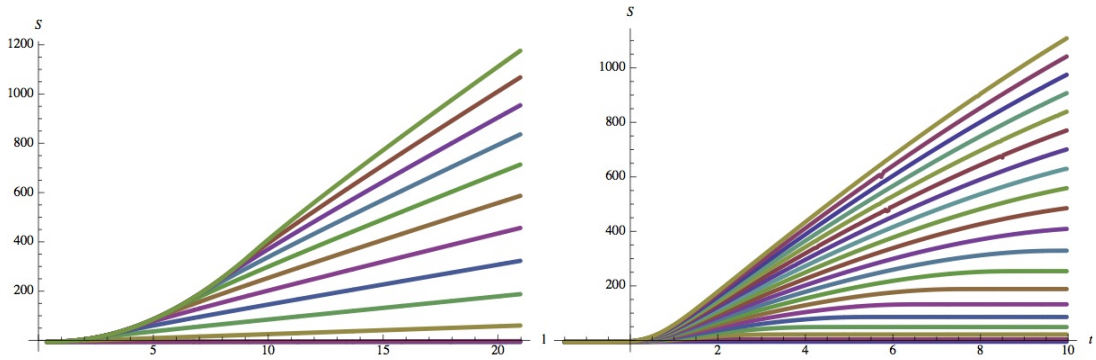

Figure 4.11: Evolution of the EE, represented for fixed times as a function of ℓ (left) and for fixed radii as a function of t (right).

We show in Figure 4.11 the results of the computation of the area of the surfaces as a function of t and ℓ. Both the horizon effect and the effective thermalization are appreciated at a speed $v_E = 1$. Figure on the right hows how it takes longer times for the HEE to acquire a constant value as the size ℓ is bigger. Then the constant value reached by the HEE coincides with that of the thermal entropy. In the left plot of Figure 4.11 this corresponds to the quadratic dependence of S on ℓ (extensivity) for $\ell < 2t$.

We found similar results for a ball in CFT_{3+1}. The EE for $\ell < 2t$ is cubic and for $\ell > 2t$ it is quadratic.

Tsunami Picture:

Given the quasiparticle picture description for the evolution of EE after a quantum quench in 1+1 dimensions [5], its generalization to higher dimensions gives rise to the tsunami picture [61]. It states that the EE is effectively propagated via an *entanglement tsunami*, which is sourced in the boundary ∂A of the entangling system A and travels inwards at a speed v_E with a sharp wave front (see Figure 4.12). As a result, the EE at a given time is the EE for the same system in the ground state plus a term that is proportional to the area covered by the tsunami at that time.

This explains the linear behavior of S in the left plot of Figure 4.11 for disks with $\ell > v_E t$. They correspond to big enough systems such that the tsunami has not had time to fully cover the whole interior. The region which has been covered is a circular crown with radii $(\ell - v_E t)$ and ℓ. Its area is then a linear polynomial on ℓ, with coefficients depending on time, linearly for the term proportional to ℓ and quadratically for the independent term.

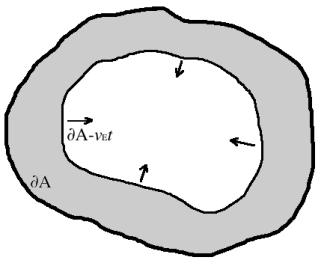

Figure 4.12: Visualization of the growth of EE as due to a tsunami propagating inwards the system. At a time t the entanglement wave front is located in the region $\partial A - v_E t$. When $\partial A - v_E t$ shrinks to zero the system A is effectively thermalized.

The straightforward generalization to compute the volume of a higher dimensional spherical crown shows that the EE of a D-dimensional ball of radius ℓ at time t (for $\ell > v_E t$) has the form:

$$S_A = \sum_{i=0}^{D-1} a_i (v_E t)^{D-i} \ell^i \ , \tag{4.50}$$

With a_i being constants. This time dependence in (4.50) can be checked in Figure 4.12.

5

Collapse in AdS II: Scalar Collapse

We solve the equations of motion of a massless scalar field and the metric and discuss the implications of some solutions for the dual gauge theory, for which we will evaluate the holographic entanglement entropy for such solutions.

5.1 Scalar collapse

We consider Einstein gravity with negative cosmological constant coupled to a real massless scalar field in four dimensions,

$$S = \int d^4x\sqrt{g}\left(\frac{1}{16\pi G_4}R - 2\Lambda - \frac{1}{2}\partial_\mu\phi\partial^\mu\phi\right) , \tag{5.1}$$

with $\Lambda = -3/l^2$. We set $8\pi G_4 = 2$ as well as $l = 1$. This system has been examined recently for the numerical study of gravitational collapse in asymptotically global AdS spaces, and we summarize some of the known results. Our emphasis, however, is set in pushing the simulation beyond the apparent horizon formation. With the aim of motivating our interpretation in the dual theory, we pursue the evolution as far as the numerical code permits us to approach the final stationary black hole.

5.1.1 Equations of motion

We will follow the ansatz and conventions in [90] for a spherically symmetric collapse. For the line element this gives

$$ds^2 = \frac{1}{\cos^2 x}\left(-A(t,x)e^{-2\delta(t,x)}dt^2 + \frac{dx^2}{A(t,x)} + \sin^2 x\, d\Omega_2^2\right) , \tag{5.2}$$

where $x \in [0, \pi/2]$ is a compact radial coordinate, and $d\Omega_2^2$ stands for the metric of the unit sphere. The equations of motion can be casted in a first order form

$$\dot{\Phi} = \left(Ae^{-\delta}\Pi\right)' \quad , \quad \dot{\Pi} = \frac{1}{\tan^2 x}\left(\tan^2 x\, Ae^{-\delta}\Phi\right)' , \tag{5.3}$$

$$A' = \frac{1+2\sin^2 x}{\sin x\cos x}(1-A) - \sin x\cos x\, A\,(\Phi^2+\Pi^2) , \tag{5.4}$$

$$\delta' = -\sin x\cos x\,(\Phi^2+\Pi^2) . \tag{5.5}$$

where $\Phi = \phi'$ and $\Pi = A^{-1}e^{\delta}\dot{\phi}$, with ϕ' and $\dot{\phi}$ the space and time derivatives of the scalar field respectively. Equations (5.3) are evolution equations for the scalar field, and (5.4)

is the Hamiltonian constraint. Due to isotropy, there are no evolution equations for the metric components.

We want to solve the previous system of differential equations given smooth initial data for the scalar field. Regularity at the origin implies $A(t,0)=1$, which fixes the integration constant from (5.4). Equation (5.5) is invariant under time dependent shifts of the function $\delta(t,x)$. This is equivalent to reparameterizing the time direction, a gauge freedom left over by the ansatz (5.2). Since we are interested in the holographic dictionary, a natural way to fix this freedom is by requiring t to be the proper time at the boundary, namely $\delta(t,\pi/2)=0$. Further imposing that the total mass remains constant along the evolution sets to zero the non-normalizable mode of the scalar, associated with a source term in the dual field theory lagrangian[1]. Under these conditions, the expansion of the fields close to the origin is

$$\phi=\phi_0(t)+\mathcal{O}(x^2)\,,\qquad A=1+\mathcal{O}(x^2)\,,\qquad \delta=\delta_0(t)+\mathcal{O}(x^2)\,, \tag{5.6}$$

whereas close to the boundary one finds

$$\phi=\phi_\infty(t)y^3+\mathcal{O}(y^5)\,,\qquad A=1-2My^3+\mathcal{O}(y^6)\,,\qquad \delta=\mathcal{O}(y^6)\,, \tag{5.7}$$

with $y=\pi/2-x$. The total mass is

$$M=\frac{1}{2}\int_0^{\pi/2}dx\,\rho(t,x)\,,\qquad \rho(t,x)=\tan^2x\,(\Phi^2+\Pi^2)\,e^{-\delta}\,, \tag{5.8}$$

where ρ provides a description of the radial energy distribution of the scalar pulse.[2]

Concerning initial conditions, they will be set as values for $\Pi(0,x)$ and $\Phi(0,x)$. The numerical integration of equations (5.3)-(5.5) subject to the above described initial and boundary conditions is accomplished using a finite difference method with a fourth order Runge-Kutta algorithm. In addition to the equations (5.3), (5.4) and (5.5) there is an additional "momentum constraint" $\dot{A}+2\sin x\cos xA^2e^{-\delta}\Phi\Pi=0$. Fulfillment of this equation and constancy of the mass will be used as quality check of our numerical simulations.

The choice of the slice $t=0$ as initial data surface is suited to the observable we want to study, namely the entanglement entropy. Ideally, we would require that its holographic derivation at any positive boundary time does not require information from across our initial data surface. The entanglement entropy is captured by the area of extremal surfaces in the bulk that anchor on the boundary of AdS to the boundary of a chosen region. In a static spacetime, these extremal surfaces are minimal surfaces and can be shown to live on constant t slices. Although this does not hold for a dynamical background, deviations are small in the cases we consider here as we will see below. For comparison, an alternative choice is to set initial data on the null infalling surface $v=0$, where v is an Eddington-Finkelstein coordinate (see for example [107][108]). This would be inconvenient in our case, as extremal surfaces ending at a boundary time $t\gtrsim 0$ would pierce that surface towards negative values of v.

[1] The scalar field can also take a constant value at infinity of no physical relevance.

[2] The integrand of (5.8) is not uniquely defined. The choice $\tilde{\rho}=\tan^2x\,(\Phi^2+\Pi^2)\,A$ reconstructs equally M [90]. Both functions give quite similar results.

Instead of performing a scan over the full space of initial conditions for the scalar field, we have restricted to gaussian type profiles localized either close to the origin of AdS

$$\Phi_c(x) = 0\,, \qquad \Pi_c(x) = \frac{2\epsilon}{\pi} \exp\left(-\frac{4\tan^2 x}{\pi^2\sigma^2}\right)\,. \tag{5.9}$$

as in [90], or close to the boundary

$$\Phi_b(x) = 0\,, \qquad \Pi_b(x) = \frac{12\epsilon}{\pi} \exp\left(-\frac{4\tan^2(\pi/2-x)}{\pi^2\sigma^2}\right)\cos^3 x\,. \tag{5.10}$$

These second type of boundary conditions, although exhibiting a very similar phenomenology to the first type, looks more akin to the Vaidya setup that has been used to model an analog to a quench in the dual field theory.

Altogether, our initial conditions are therefore parameterised by two variables, the amplitude ϵ and the width σ. Of course, the space of initial conditions is infinite dimensional, and may hide surprises that deserve to be unveiled. Some of them involve stationary regular solutions with and without rotation [100] and, from them, at least one has been constructed numerically [101].

5.1.2 Collapse portrait

Black holes formed in the collapse of a spherical shell of a massless real scalar field are of Schwarzschild type and can have either positive or negative specific heat. With our conventions, the threshold mass separating both cases is [3]

$$M_{th} = \frac{2}{3\sqrt{3}} \sim 0.385\,. \tag{5.11}$$

Big (small) black holes refer to those with masses above (below) this threshold, which correspondingly have positive (negative) specific heat. Due to the negative specific heat, small black holes can not be in thermal equilibrium with their own Hawking radiation, and they will evaporate very much as they do in flat space. For small G_N however, Hawking radiation is suppressed and the process of evaporation becomes very slow as compared with the time scales we will be interested in. Moreover this type of configurations has been shown to have higher entropy than thermal AdS with the same energy [109]. Hence in the microcanonical ensemble we are considering, both small and large AdS black are valid collapse end products.

Regardless of which one of the profiles (5.9) or (5.10) are used as initial data, for masses above or comparable to M_{th}, the direct formation of a black hole of the total mass is observed. Decreasing the mass neatly below M_{th}, the emerging apparent horizon starts trapping only a fraction of the scalar pulse, while the rest scatters towards the boundary. Upon lowering the amplitude further, a critical black hole (actually a naked singularity) of vanishing radius (hence mass) can form. This is in total agreement with the findings by Choptuik [88] in asymptotically flat space.

The presence of an apparent horizon is signalled by a zero of the function $A(t,x)$. However this function does not strictly vanish at any finite value of t, since as it drops the

[3] Schwarzschild-AdS$_4$ black holes have a temperature $T = (3\tan^2 x_h + 1)/\tan x_h$, where x_h is the largest root of $2M\cos^2 x = \tan x$. The threshold mass is set by requiring $dT/dM = 0$.

relative redshift factor with respect to the boundary grows very large and the dynamics gets frozen around the emergent horizon. Hence in the coordinate system we are using, it only makes sense to define the time of horizon formation as that when the minimum of $A(t, x)$ drops below a sufficiently small value. In this sense it should be understood below.

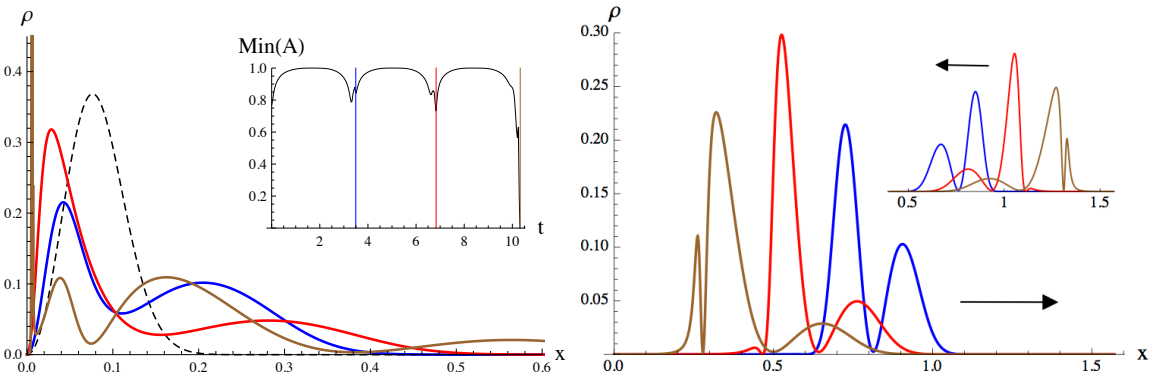

Figure 5.1: Evolution of a narrow pulse (5.9) with $\sigma = 1/16$ and $M = 0.015$. Left: the dashed line shows the initial mass distribution function. The curves in color denote the mass density profile at the times when the pulse bounces against the origin producing a minimum of $A(t, x)$ (see inset). Field values grow wild with time at the origin, enhancing the non-linear effects. Right: scalar profiles from the first (blue), second (red) and third (brown) bouncing cycles; the arrows indicate the direction of movement. The scalar profile changes its shape when scattering at the origin, while it travels almost unaltered along the full radial coordinate.

New effects appear below the threshold amplitude for critical collapse. In flat space, all the mass would just be reflected back to infinity and that would be the end of the story. Here instead, the massless scalar pulse that escapes towards the boundary of AdS reflects in finite proper time, and falls in again. In [90] [95] support for a remarkable phenomenon was provided for AdS_{d+1} when $d \geq 3$: well localized scalar profiles of arbitrary small initial amplitude always generate a horizon after a sufficient number of bouncing cycles. The mechanism behind this phenomenon is the transfer of energy from long to small wavelengths along the evolution [90] [96]. Analogous effects are well known from fluid dynamics [110], where they are referred to as weak turbulence. This fact is responsible for the change of shape of the traveling wave and the sharpening of at least one of its fronts. Its action is most effective at the origin, where the bouncing produces extremely high values of the fields, therefore enhancing the effect of the nonlinearities. After enough number of bounces a sufficiently sharp subpulse freezes, and the radial minimum of $A(t, x)$ drops abruptly (see inset in Fig.5.1a). This is the defining time for an apparent horizon formation, although as said before, in these coordinates the exact formation occurs in infinite time.

We would like to point out an effect accompanying the transfer of energy towards small wavelengths. Each time the signal scatters at the origin and a part of it sharpens, the rest instead tends to increase its radial dispersion. This behavior, which will prove to have important consequences for the dual field theory, is illustrated in Fig.5.1a using a narrow initial profile which requires three bounces for collapse. There we have plotted the mass distribution function $\rho(t, x)$ (5.8) at the times of closest approach to the origin. On Fig.5.1b

we illustrate how the scalar profile changes shape when it scatters at the origin, while its shape remains largely unaffected upon propagating and reflecting against the boundary. The profiles in color blue, red and brown correspond respectively to configurations along the first, second and third bouncing cycles. The apparent horizon is generated from the small spiky front in the brown profile.

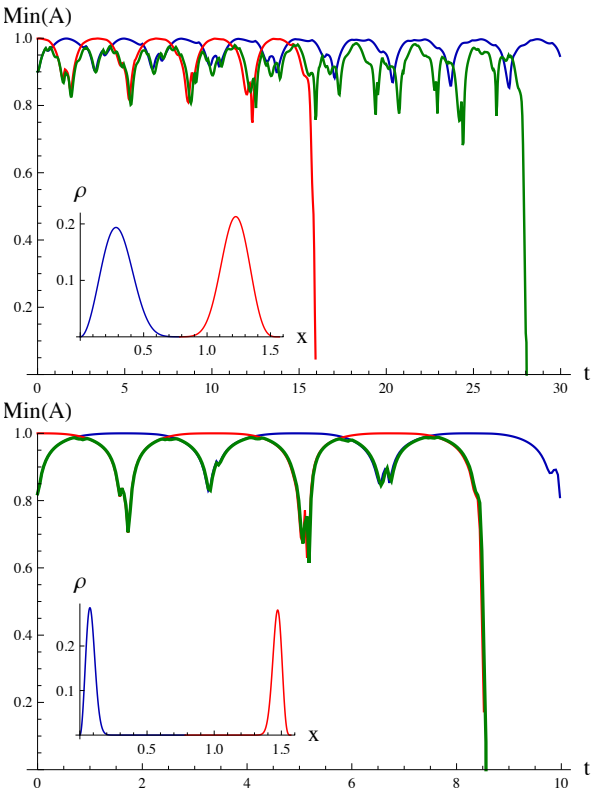

Figure 5.2: Evolution of the initial data (5.9) (blue), (5.10) (red) and the combined profile (5.12) (green) for the following subpulse data. Left: $\sigma = 0.25$ and $M = 0.012$. Right: $\sigma = 1/16$ and $M = 0.029$. In the inset, the initial mass density function. The left initial data have more overlap than the right ones. The horizon formation time for the fast collapsing pulse (red curve) gets affected and delayed (green curve), whereas it remains unaltered in the non-overlapping case on the right.

Besides the mass, a parameter which has strong influence on the evolution of a scalar pulse is its broadness. The relevance of this parameter was made manifest in [102]. It was shown that the turbulent mechanism characteristic of the narrow pulse evolution becomes less efficient as the broadness of the profile grows. Broad pulses quickly develop a subpulse structure with infalling and outgoing components which scatter among themselves. In order to better understand the interaction among subpulses, let us consider a different initial profile: a linear combination of (5.9) and (5.10) producing two well localized pulses close to the origin and the boundary

$$\Phi(x) = 0\,, \qquad \Pi(x) = \Pi_c(x) + \Pi_b(x)\,. \tag{5.12}$$

We choose them to have the same broadness and the same mass. When the tails of the initial pulses have some overlap, the creation of an apparent horizon is delayed with

respect to the independent evolution of the pulse that would collapse first, Π_b. We observe in Fig.5.2a that the number of bounces necessary for the creation of a horizon increases. Hence scattering tends to work against weak turbulence, which in this example finally wins. Interestingly, pulses with a negligible initial superposition are practically transparent to each other, as shown in Fig.5.2b.

Collapse processes with very broad initial profiles present distinguished characteristics. They are delocalized along the complete radial direction in the major part of the evolution. The oscillation periodicities of these solutions are determined, besides radial displacement, by their internal subpulse structure. As a result, the bouncing cycles are not neatly defined, see Fig.5.3a. Moreover, the horizon emerges supported by a finite fraction of the pulse mass, in contrast to narrow pulses where it can be vanishingly small. Delocalized pulses require masses around 40% the threshold mass (5.11) to generate an apparent horizon. When the total mass is decreased, a point is reached where the time elapsed until horizon formation abruptly increases [102] [103]. For masses below this threshold our results join previous analysis supporting the establishment of a regular quasi-standing wave [100]-[103].

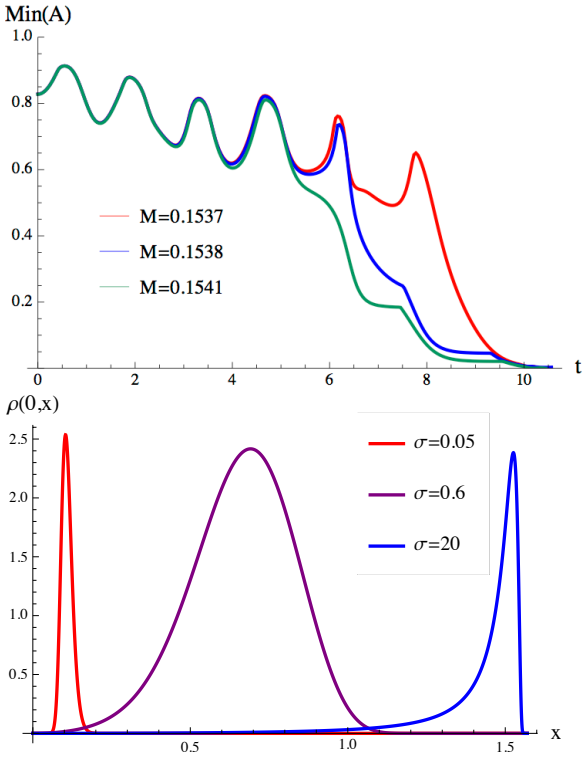

Figure 5.3: Left: Broad initial profiles of the form (5.9) with $\sigma = 0.6$. Right: influence of the parameter σ on the initial mass density function $\rho(0, x)$. ϵ has been adjusted to make all curves similar in height.

For initial conditions of the form (5.9) the threshold broadness for the existence of regular solutions appear to be around $\sigma \sim 0.35$ [102]. In [103] the numerical analysis at $\sigma = 0.6$ confirmed the regularity of the evolution. However, for large values of σ, again collapse to black hole formation is observed. Their interpretation thereafter is that, for

some intermediate values of σ, the evolution lies within the domain of attraction of stable periodic solution that bifurcate from the fundamental mode of the linearized scalar wave equation in AdS, which the authors in [99] termed "oscillons". For the lowest frequency in AdS_4 they are given by

$$\phi^{osc}_{j=0}(t,x) = a\cos(3t+\alpha)\cos^3 x\,, \tag{5.13}$$

with constants a and α. For $\alpha = \pi/2$, the initial conditions

$$\Pi^{osc}_{j=0}(0,x) = 3a\cos^3 x\,, \qquad \Phi^{osc}_{j=0} = 0\,, \tag{5.14}$$

are actually very similar to those coming from (5.9) with $\sigma \sim 0.6$.

On the other hand, the sharpness or broadness of the initial profile should be established on the mass density function, $\rho(x)$, rather than on the profile of the scalar field. We observe from the Fig.5.3b that indeed, sharp localized profiles exist both at small and at large values of σ. Similar reasoning can be applied to initial conditions of the form (5.10). When $\sigma \gtrsim 2$ the exponential factor in that profile can be neglected, and $\Pi_b(0,x) \propto \Pi^{osc}_{j=0}(0,x)$. We have checked that for small enough amplitudes the evolution of these initial data is regular up to the reach of our computational capabilities.

5.1.3 Post-horizon evolution

Previous numerical simulations have been stopped at the moment when an apparent horizon forms. We need however to pursue the evolution as close as possible to the set up of the final static black hole in order to give a dual interpretation to the collapse processes we are studying. Although the dynamics around an emergent horizon gets practically frozen, the part of the scalar pulse that escapes its trapping effect continues traveling and reflecting towards the boundary. We have been able to describe this dynamics using the same coordinate system (t,x) by increasing the resolution of the radial grid. Using grids with up to 10^5 points we have obtained post-horizon evolutions within an acceptable precision. Namely we have checked that the momentum constraint remains under control, the total mass of the configuration keeps constant up to few percent, and all function converge smoothly under variations of the resolution.

In Fig.5.4 we plot the post-horizon evolution of a narrow profile for which $A(t,x)$ abruptly drops after one bounce (see inset). The horizon radius at that moment is approximately half the one of a Schwarzschild BH of the total mass. When the apparent horizon emerges, the leftover scalar profile has already started its way to the AdS boundary. The mass distribution function at this moment is shown in Fig.5.4a (light blue). Subsequently this outgoing fraction of the pulse bounces with the boundary and falls in again, being partially absorbed and partially reflected. As a result of this, a new minimum of $A(t,x)$ drops to zero at a larger value of x, in accordance with the expected growth of the horizon. This is shown in Fig.5.4b. We managed to follow this process past the completion of a second bounce with an acceptable precision. The total mass of the scalar pulse, obtained by integrating $\rho(t,x)$ and which should keep constant along the evolution, only suffers a 2% loss in each post-collapse cycle for a grid of 5×10^4 points (see inset). The numerical noise around the minima of A in Fig.5.4b could be linked to the small mass loss.

The horizon radius after two bounces is still far from that of a Schwarzschild BH of the total mass (dashed black line in Fig.5.4b). Several further bouncing cycles appear

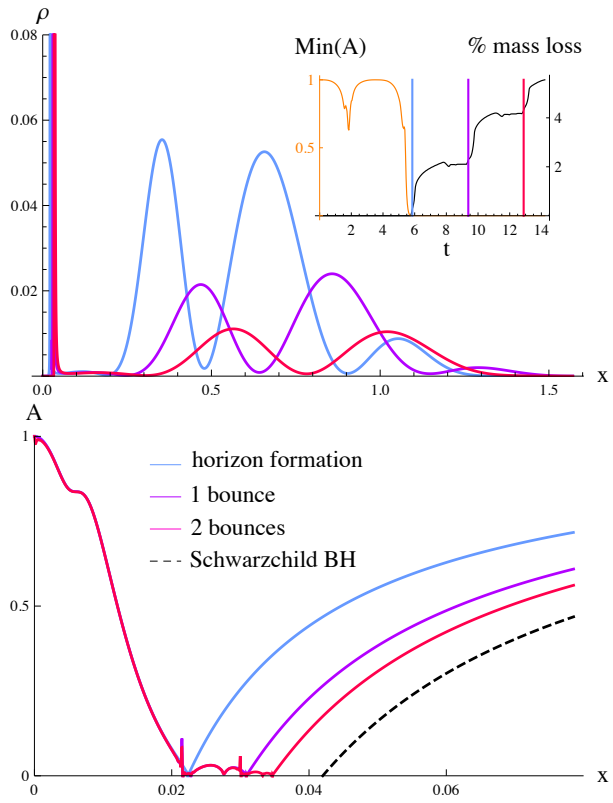

Figure 5.4: Evolution of a narrow pulse (5.10) with $\sigma = 0.1$ and $M = 0.021$. Left: leftover scalar pulse after horizon formation and two post-collapse bounces. Right: horizon growth.

to be necessary to complete the collapse process. This is likely a generic feature. At a linearized level one can calculate the absorption of scalar field to be consistent with an outside amplitude that decreases exponentially with time $|\phi|_{out} \sim \exp(-\omega_l t)$ with $\omega_l \sim r_h^2$, [111] [112]. Of course, deriving this dependence in the full non linear setup is an interesting question we hope to report on in the near future.[4]

As it was the case for the pre-horizon dynamics, the post-horizon counterpart also depends on the broadness of the scalar profiles. Pulses of intermediate broadness show some degree of localization along the pre-horizon evolution. However once an apparent horizon emerges, the fraction of the scalar pulse left out looses radial localization and a damped quasi-standing wave sets in. This is indeed consistent with a result presented in the previous subsection. Namely, the weak turbulence mechanism implies, together with the progressive sharpening of a fraction of the scalar pulse, the radial dispersion of the rest.

An example of this behavior is shown in Fig.5.5a for an initial profile (5.9) with $\sigma = 0.25$. After two well defined bouncing cycles, the value of $A(t, x)$ suddenly drops. As the evolution continues new minima of A appear at growing values of the radial coordinate, until the final value given by the radius of a Schwarzschild black hole of the total mass is reached (see inset). We have plotted a complete cycle of the left-out quasi-standing

[4] We would like to thank Vitor Cardoso for clarification on this point.

wave (blue, red and magenta curves), which perfectly matches the generation of new A minimum. Following the post-horizon evolution is less demanding numerically for broad that for narrow pulses. We could reach a horizon radius up to within 3% of the final value in our example while keeping the mass loss around 0.1% using a grid with 2×10^4 points.

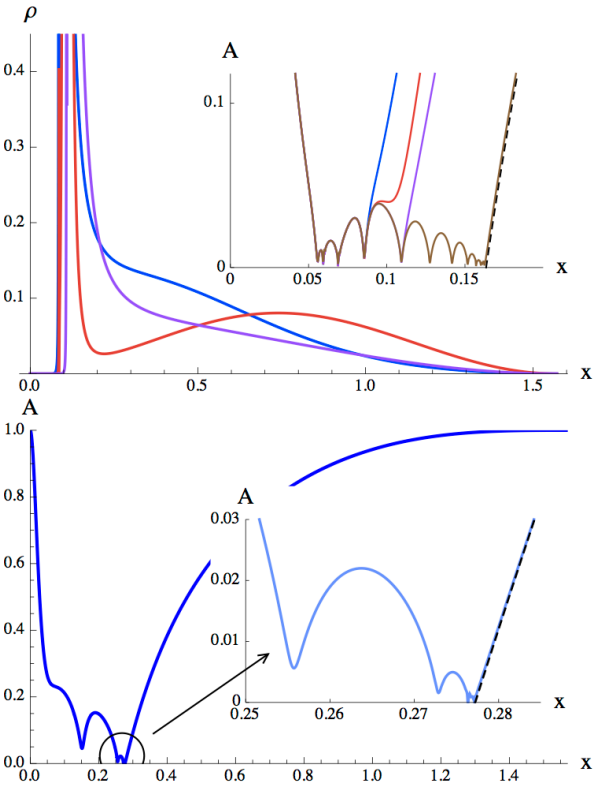

Figure 5.5: Left: cycle of the post-horizon damped wave for a profile (5.9) with $\sigma = 0.25$ and $M = 0.085$. In the inset we have plotted $A(t, x)$ when the collapse process is nearly completed. The dashed black line shows $A(x)$ for a Schwarzschild BH of the total mass. Right: same plot as in the inset for a profile (5.9) with $\sigma = 0.6$ and $M = 0.1538$.

In the case of radially delocalized pulses, the function $A(t, x)$ does not drop abruptly to zero. This can be observed in Fig.5.3a for several pulses with $\sigma = 0.6$. A dynamics similar to the quasi-standing wave of Fig.5.5a, but with a stronger damping, is established when the minimal radial value of A stops oscillating and starts decreasing. However, the minimum of A only becomes vanishingly small at a radial position very close to the final horizon radius. This can be appreciated in Fig.5.5b for the scalar pulse with $M = 0.1538$ from Fig.5.3a.

The periodicity of the bouncing cycles is a very important information for the dual interpretation of the collapse processes. The bouncing period of narrow pulses is always bigger but close to π, increasing with the mass and broadness of the scalar profile[5]. Instead, when the pulses are broad and dynamics is radially delocalized, a shorter periodicity

[5]The bouncing period is practically π when measured with respect to proper time at the origin [90]. However for a boundary observer more energetic pulses take a longer time to climb up their own gravitational potential.

emerges. It governs the metric oscillations of the broad initial profiles shown in Fig.5.3a, as well as the damped quasi-stationary wave of Fig.5.5. The presence of a faster oscillation should be traced back to the internal dynamics of the delocalized scalar pulse, rather than to radial propagation. The value of its period is always bigger but not far from $\pi/3$. The origin of this frequency is related to the large overlap that broad profiles have with the regular periodic solution found in [101], which, in turn, branches out from the lowest linear "oscillon" (5.13). The periodicity of (5.13) is actually $2\pi/3$. However if we consider the backreaction of this scalar configuration on the metric, which is sourced by the squares of the field derivatives, its resulting natural period is $\pi/3$.

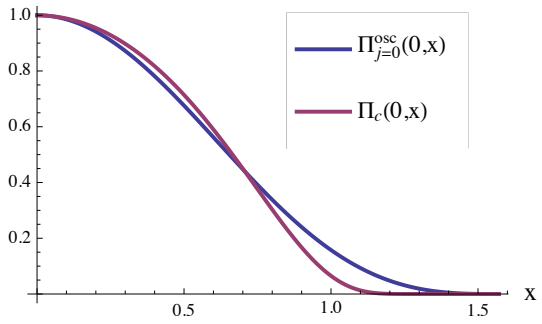

Figure 5.6: Initial data for $\Pi_c(0,x)$ with $\sigma = 0.6$ and $\Pi^{osc}_{j=0}(0,x)$ for the lowest linear "oscillon" given in (5.13), chosen to have the same height. The overlap is substantial, supporting the argument that their posterior evolutions, for small amplitudes, are in the same island of stability around the (close to) $w_0 = 3$ periodic nonlinear solution constructed in [101].

The appearance of this frequency is mysterious from the point of view of the quantum field theory. As a matter of fact, a hint on some experimental quantum observable which may have frequencies in the "oscillon" sequence, $\omega_j = d + 2j$, would have breathtaking implications pointing towards a more than accidental relevance of the AdS/CFT correspondence.

5.2 Dual interpretation of the bounces

5.2.1 Dephasing and self-reconstruction

An important notion in out of equilibrium physics is that of dephasing time. This is the time that a system takes to lose quantum coherence. Since we are dealing with closed systems, this notion will rather refer to the moment at which entanglement becomes inaccessible to macroscopical observables. After dephasing, the system is expected to relax to a stationary state, generically a thermal state.

The linear growth in threshold time, as shown in (4.27), implies that no matter how long we wait after a quench in an infinite system, there are always large enough regions where quantum coherent correlations can be detected. Namely, dephasing is never achieved at the global level. With the aim at providing a dual interpretation for the bouncing geometries studied in the previous section, we review now the different scenarios

that can arise on a compact space. As motivated above, we assume that the initial state that triggers the field theory evolution presents stronger entanglement among neighbouring degrees of freedom. The typical separation of entangled components will start growing much as it does in the non-compact case. What happens after the maximal separation is achieved depends however, crucially, on interactions.

The simplest case to consider is that of a non-interacting theory with linear dispersion relation living on a circle. Any initial state reconstructs itself periodically, preventing the system to equilibrate. When the initial state is homogeneous, this periodicity is

$$t_0 = \frac{L}{2v} \tag{5.15}$$

with L the length of the circle and v the propagation velocity of the excitations [86] [113]. We will refer to t_0 as propagation time, since it is the time that two particles moving apart with speed v on the circle take to meet again.

The pattern in an interacting field theory is expected to differ substantially. As entangled excitations created at close points reach maximal separation on the circle, and naively start approaching again, interactions will have generically randomized their relative phases preventing the initial state from reconstructing [86]. A strongly interacting holographic version of this behavior is provided by the 3d collapse of a thin spherical shell of null dust. The absence of pressure induces the formation of a black hole by direct collapse, and the EE of half the circle achieves a final value at

$$t = \frac{L}{4}\,. \tag{5.16}$$

This time consistently equals the one needed by two particles that separate at the speed of light to reach opposite points on the circle.

The evolution of dephasing not only hinges upon the microscopic dynamics, but also depends upon the structure of the initial state. Let us illustrate this statement with an easy example, by looking at the behavior of free systems with a non-linear dispersion relation. This is the case of a periodic chain of coupled harmonic oscillators

$$H = \frac{1}{2}\sum_{i=1}^{N}\left[\pi_i^2 + \nu^2(\phi_{i+1}-\phi_i)^2\right]. \tag{5.17}$$

Its spectrum is given by non-interacting modes of momentum $p = 2\pi n/N$ with $n = 0,\ldots,N-1$ and frequency

$$\omega_p = 2\nu \sin\frac{p}{2}\,. \tag{5.18}$$

For $p \ll \pi$ the dispersion relation becomes linear, $\omega_p \simeq \nu p$. An initial wave packet constructed out of low momenta will reconstruct itself with period $t_0 = N/2\nu$, as in (5.15). No sign of relaxation will appear until enough time has passed to render important the non-linearity of the dispersion relation. If the wave packet is centered around frequency $\bar{\omega}$, this time is [62]

$$t \simeq \frac{N^2}{\bar{\omega}}\,. \tag{5.19}$$

Afterwards the system dephases and tends to a stationary state.[6] The dephasing time can be much larger than the propagation time t_0 if $\bar{\omega}$ is chosen sufficiently small. It is

[6]The stationary state generically differs from thermal equilibrium since the occupation numbers of non-interacting modes are conserved along the evolution

important to emphasize here that this dependence of the relaxation process on the initial state is indeed seen in experimental setups [67] [68] [69] [72].

We can now state the main proposal of this chapter: *collapses which require bouncing on the AdS boundary before forming a horizon are holographically dual to field theory evolutions where the initial state is partially reconstructed several times before achieving equilibration.*

In other words, the dephasing time is much larger than the typical propagation time, in analogy with the case of the harmonic chain above. We have argued that in an interacting field theory this is not the generic behavior. However, that reasoning can fail for states with small enough energy density. The finite size of the system introduces an intrinsic scale and, hence, the dynamical process can also depend on the energy density of the initial state. This is precisely what is found in the holographic models based on the collapse of a massless scalar profile [90]. When the mass of the scalar shell is above the threshold (5.11) for the formation of a large black hole, the shell is completely trapped behind a horizon by direct collapse. Bouncing with the AdS boundary is only required when the final black hole to be formed is small.

In the same way that an infalling scalar pulse is to be holographically interpreted as a growing separation between entangled excitations, the stages of the evolution when it moves towards the AdS boundary should represent entangled excitations joining again. This can be neatly seen using a thin shell of null dust that travels outwards and reaches the boundary at $t=0$. The same reasoning that for an infalling shell sets the bound (4.27), leads now to

$$0 \leq l \leq -2t\,, \tag{5.20}$$

for the size of intervals producing a thermal result for the entanglement entropy. Hence their size decreases as the system evolves towards $t = 0$, as can be predicted from the qualitative picture in Fig.2.3.

A very nontrivial support for this picture comes from the periodicity of the scalar pulse in the bulk. From the numerical simulations, one can see that its evolution from the boundary to the center and back completes a full roundtrip with a period of approximately π (see for example the inset in figure 5.1a). Now, recalling that in the gravitational system we have fixed the radius of the boundary sphere to unity, the expected reconstruction time (5.15) is

$$t_0 = \frac{L}{2} = \pi \tag{5.21}$$

where $L = 2\pi$ is the length of an equator. As we have mentioned in Section 2, the exact periodicity is slightly bigger than π and this delay increases with the amplitude of the pulse. We will relate this fact to the presence of interactions in Section 4.1.

Besides dephasing, another process which is crucial in order to achieve thermal equilibrium is the equipartition of energy among degrees of freedom. If the radial position of the traveling shell would also describe this process, we should expect an oscillatory pattern in the evolution of the occupation numbers. However periodicities in occupation numbers are more naturally associated with Poincare recurrences, and in a large N system these take a much longer time than $L/2$. Hence we are led to conclude that the radial displacement of the scalar shell is not directly related with the redistribution of energy, and its periodic behaviour is tantamount to the reconstruction, or revival, of the initial dual quantum state. Evidence for revivals has been observed experimentally in cold atoms

systems [91]. At a theoretical level, it has been seen in quantum spin chains [92] [93] and also in CFT in 1+1 dimensions [94].

5.2.2 Broadness versus time span

In our set up no reference is made as to how the initial state that triggers the evolution was created. In order to understand the implications of broad scalar profiles, it is however useful to discuss rough characteristics of field theory perturbations that can holographically relate to them.

To gain insight we can resort again to the familiar case of the Vaidya metric

$$ds^2 = \frac{1}{\cos^2 x}\left[-\left(1 - m(v)\frac{\cos^2 x}{\tan x}\right)d^2v + 2dvdx + \sin^2 x\, d\Omega_2^2\right] \tag{5.22}$$

with v an Eddington-Finkelstein infalling coordinate. We choose a mass function satisfying

$$m(v) = \begin{cases} 0 & v < -\Delta t\,, \\ M & v > 0\,. \end{cases} \tag{5.23}$$

It represents the building up of an energy density $\epsilon = M$ in a finite time span Δt starting from the CFT vacuum. The null dust shell sourcing the metric (5.22) has support in the region $v \in [-\Delta t, 0]$. Upon transforming to the Schwarzschild coordinates (t, x), the shell exhibits a finite broadness in the radial direction. This is shown in Fig.5.7a, where the intersection of a succession of slices of constant t with the location of the shell, highlighted in yellow, determines its radial localization. Its profile at several t slices is plotted in Fig.5.7b.

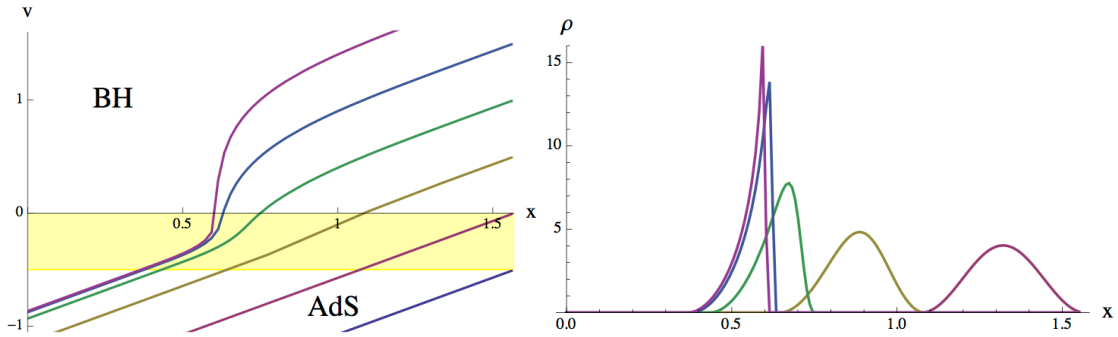

Figure 5.7: Left: intersection a null dust shell with $\Delta = 1/2$, signaled in yellow, with the lines of constant $t = -0.5, 0, \ldots, 2$ in the (v, x) plane. Right: mass distribution function at the same t slices.

The mass distribution function in Fig.5.7b corresponding to $t = 0$ provides the analogue of the initial data we are dealing with in this paper. Its value at a given x reflects the density of excitations created at a prior time

$$t \sim x - \pi/2 \leq 0\,. \tag{5.24}$$

The earlier some excitations have been created, the further entangled components are able to fly apart and the deeper its holographic representation reaches in the x direction.

We will adopt this point of view in order to interpret the scalar profiles, as sketched in Fig.5.8. Hence the dual field theory state associated to a broad pulse should describe a configuration with entanglement over many length scales.

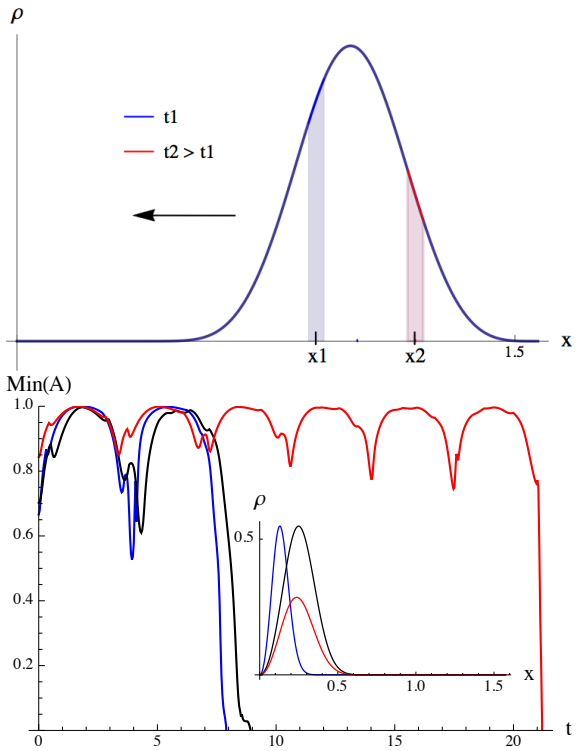

Figure 5.8: Left: Excitations sourced during small time intervals around $t_1 \sim x_1 - \pi/2$ and $t_2 \sim x_2 - \pi/2$. Right: Evolution of $\min_x A(t,x)$ for several pulses: $\sigma = 0.1$ and $M = 0.035$ (blue), $\sigma = 0.2$ and $M = 0.066$ (black) and $\sigma = 0.2$ and $M = 0.035$ (red). In the inset we plot the initial mass density distribution for each pulse.

The field theory dual to the collapse processes we are considering is in a pure state along the complete evolution (see below) [1] [86]. One pertinent question is: how much correlation exists between the components x_1 and x_2 that build up the profile in Fig.5.8a. Let us recall the evolution of the initial profile (5.12), which is composed of two well localized subpulses. When the overlap between subpulses is negligible, the gravitational dynamics renders them transparent to each other, see Fig.5.2b in Section 2. This is however not the case for the profile in Fig.5.2a, where the pulses have a small overlap. Both effects point to the existence of entanglement among the adjacent components of the profile in a way that grows with their proximity. This point deserves a deeper investigation.

On general grounds, the time that a quantum system takes to dephase should depend on the amount of strongly correlated components it contains rather than on the total energy density. According to our interpretation, the height in $\rho(0,x)$ provides a qualitative measure of the number of initially strongly correlated excitations. Hence the time for horizon formation, to be related with the dephasing time in the dual field theory, must be influenced by this value. This is what we find in Fig.5.8b, where we plot the evolution of three different pulses whose initial distributions can be seen in the inset. One of them,

blue, has half the broadness of the other two. It coincides with the black one in the value of the initial amplitude, while with the red one in the total mass. The time of horizon formation is very similar for the pulses with the same amplitude (blue and black). However when we compare pulses of the same mass, it is much longer for the broader one (red).[7]

5.3 Entanglement entropy oscillations

We will compute the holographic entanglement entropy in these geometries. The regions A we will be interested in are circular caps in the boundary $\mathbb{R}\times S_2$ of global AdS_4. Exploiting the symmetry of the problem, γ_A will be a surface of revolution which only depends on a polar angle of the boundary S_2. Hence the task is to find functions $x(\theta)$ and $t(\theta)$ that extremize the area functional subject to the boundary conditions

$$x(\theta_0)=\pi/2\,,\qquad t(\theta_0)=t_0\,,\qquad x'(0)=t'(0)=0\,, \tag{5.25}$$

where θ_0 is the angular aperture of the cap. This is a boundary value problem and to solve it we have used a relaxation algorithm as explained in Section 3.3.3.

The entanglement entropy is a UV divergent quantity and, correspondingly, the area of any surface satisfying (5.25) is also divergent. The area of the extremal surface anchoring on a cap on empty AdS_4 has been obtained explicitly [115]

$$\text{Area}(\gamma_A)=2\pi\left(\frac{\sin\theta_0}{\epsilon}-1\right)\,. \tag{5.26}$$

The factor 2π is due to the rotation symmetry of the configuration. In order to get a finite result the radial direction has been cut at $x_M\lesssim\pi/2$. The quantity $\epsilon=\cot x_M$ has the interpretation of a UV field theory cutoff. Hence the first term in parenthesis gives the area law characteristic of the entanglement entropy [23]. As discussed in Chapter 2 and in [77], we define the finite contribution to the EE by

$$S(t,\theta_0)=\frac{\pi}{2G_4}\left(\frac{\text{Area}(\gamma_A)}{2\pi}-\frac{\sin\theta_0}{\epsilon}\right) \tag{5.27}$$

The smoothness conditions (5.6) that we imposed at $x=0$ imply that γ_A is homologous to both A and $\bar{A}$. Thus $S_A=S_{\bar{A}}$, reflecting the fact that we are holographically modelling the unitary evolution of a pure state as in Chapter 4 and also explained in [86]. The equality $S_A=S_{\bar{A}}$ implies that it suffices to study the EE of regions not larger than a hemisphere, namely $\theta_0\in[0,\pi/2]$.

The portion of spacetime covered by the coordinates (t,x) does not reach behind the apparent horizon. Using a lightlike coordinate v instead of t, it has been shown in Chapter 4 that the extremal surfaces calculating the HEE in a Vaidya collapse can cross both the event and the apparent horizons. They do so for boundary times and regions whose size is larger than the scale set by the collapsing shell, which is proportional to $M^{-\frac{1}{3}}$. However we are focussing in scalar configurations for which this scale is larger than the size of the boundary sphere, since these are the only ones that require several bounces before forming a horizon. Therefore the extremal surfaces we need to calculate will not reach the apparent horizon, and the coordinates (t,x) suffice to describe them.

[7] See [102] for a systematic study of the collapse time upon varying the amplitude and the broadness.

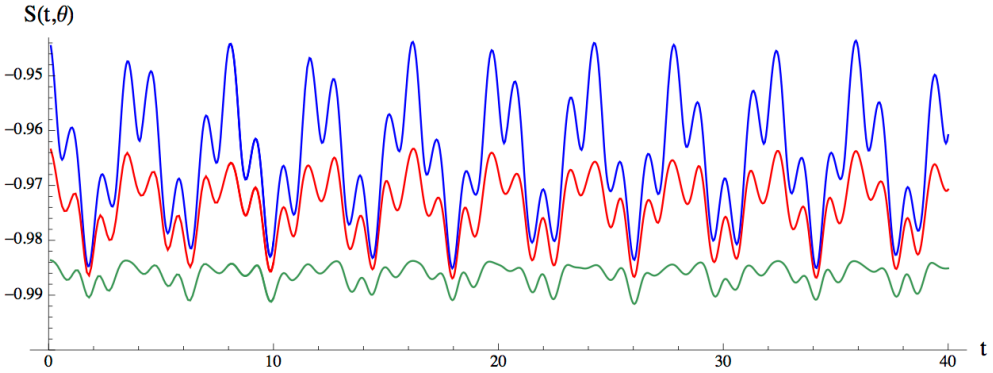

Figure 5.9: EE oscillation for an initial profile (5.9) with $\sigma = 0.4$ and $M = 0.09$. Different colors correspond to caps with angle of aperture $\theta = .9, 1.2, 1.5$.

The bouncing geometries induce an oscillating pattern in the entanglement entropy. An example is shown Fig.5.9 for a pulse with a regular evolution, namely no horizon seems to emerge, and whose dynamics is somewhat between a quasi-standing wave and a localized pulse. The holographically associated entanglement entropy exhibits oscillations with two clear periodicities, close to $\pi/3$ and π. These are respectively the periodicities characteristic of the internal dynamics of the pulse and of its radial displacement.

In the next subsections we will analyze the most relevant features of the holographic entanglement entropy evolution. Our aim is twofold: we want to learn about the non-equilibrium dynamics of finite size closed systems at strong coupling and, at the same time, explore the holographic dictionary in dynamical situations.

5.3.1 Early time dynamics

We shall start our analysis by focusing on the growth of the entanglement entropy as the scalar pulse first falls towards the interior geometry. To that purpose we consider narrow initial profiles localized close to the boundary as described by (5.10).

In Fig.5.10a we compare two well localized pulses of the same broadness but different amplitudes. One of them gives rise to a black hole of the total mass by direct collapse ($M = 0.3$), while the other requires three bounces for the emergence of an apparent horizon ($M = 0.012$). For the sake of comparison, we have rescaled the entanglement entropies of the later case such that they coincide with the former one at their maxima. We find no significant difference between the EE growth to its first maxima for the small mass process and to its final values for the direct collapse one. Pursuing this line, in Fig.5.10b we compare a one-bounce ($M = 0.014$) with a many-bounce pulse ($M = 0.008$) using the same rescaling of entropies as before. In this case there is a perfect match in the growth of the EE for both pulses. Moreover, also the decrease to the subsequent minimum is very similar. The only important difference is in the time that $S(t, \theta)$ spends at its maximum, which grows with the mass.

These results allow us to sharpen the dual interpretation. The early time dynamics proceeds very much as in non-compact space. Namely, the evolution of the entanglement entropy is qualitatively well described by the propagation model in Fig.2.3, where the entangled components of the plasma separate at the speed of light. This is illustrated

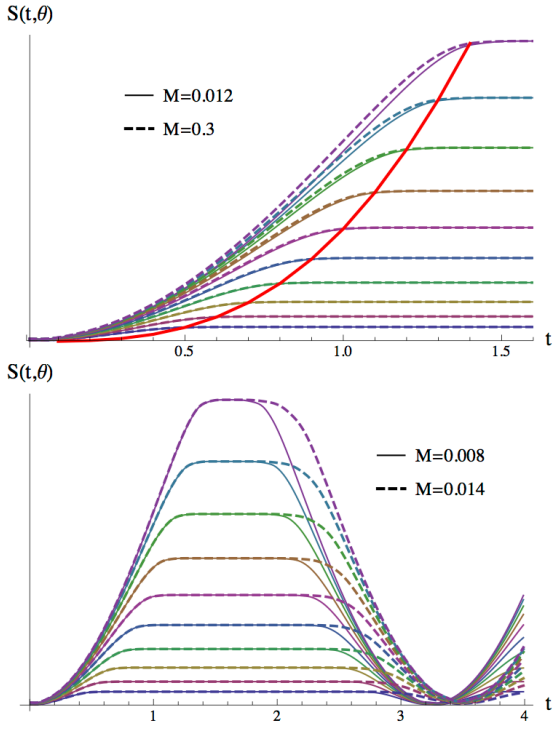

Figure 5.10: EE evolution for several pulses with $\sigma = 1/16$. Different colors correspond to caps with $\theta = .5, .6, .., 1.4$. In each graph, the EE values for the lower mass pulse have been rescaled to coincide with those of the larger mass one at their maxima for the sake of comparison. The red line on the left figure gives, for the pulse with larger mass, the EE at $t = \theta$.

by the red curve in Fig.5.10a. This curve gives the value of the EE at $t = \theta$, and very approximately signals the moment at which $S(t, \theta)$ saturates to its maxima. Moreover, we have compared the EE growth for narrow shells which form a black hole by direct collapse and Vaidya configurations of approximately the same broadness and mass, observing again no relevant difference.

The effective propagation of entanglement at the speed of light implies that the bulk of entangled excitations have reached their maximal separation on the two-sphere at $t \sim \pi/2$. However the period needed by the scalar shell to complete a bouncing cycle is always above, although close to π. It is practically π for pulses of very small mass and increases for more massive ones, as can be seen in Fig.5.10b. A dual heuristic picture for this effect could be as follows. Strong interactions might have generated a phase shift on the field theory wavefunction that effectively induces a larger radius for the two-sphere. Since the entanglement entropy depends on the actual size of the region considered, the only natural imprint of the phase shift on the EE would be to prolong the time interval that it keeps at its maximum values. Being an effect due to interaction, it should increase with the energy density of the state, $\epsilon = M$. This pattern is precisely what we observe in Fig.5.10b.

5.3.2 Holographic evolution

In this subsection we study the evolution of the entanglement entropy based on radially localized pulses. The collapse of narrow pulses is led by a transference of the energy towards high momentum modes, such that a fraction of the pulse develops a peak sufficiently sharp to become trapped by an emerging horizon. The remaining pulse is swallowed stepwise by a growing horizon, until a final black hole of the total scalar shell mass sets up.

Let us analyze first the evolution of the entanglement entropy before a horizon emerges. Remarkably we find that the EE of large regions not only oscillates, but its maxima in each bouncing cycle slightly decrease. We illustrate this effect in Fig.5.11a with a narrow pulse which starts close to the origin and requires three bounces to generate a horizon. We showed in Section 2 that when the pulse reaches the origin two opposite effects take place. Namely, together with the sharpening of a fraction of the pulse, the rest tends to increase its radial dispersion, see Fig.5.1a. As a result the extremal surfaces associated to the EE maxima of large boundary regions intersect, at each successive bounce, a growing and more spread fraction of the scalar pulse. This causes the decrease in area and, hence on $S(t,\theta)$, visible in Fig.5.11a.

Although this is a small effect, we find it relevant. It has been suggested that the entanglement entropy of half the space could provide a definition of coarse grained entropy [86]. In spite of the oscillations, we might have expected that the maxima of the entanglement entropy monotonically increase along the evolution, and their value still serves as a notion of coarse grained entropy. We have seen that not even this is true in general. Recently it has been proposed a different holographic definition of coarse grained entropy [117], related to holographic causal information [118]. It would be very interesting to study its evolution in the collapse processes we are considering.

The radial minimum of the metric function $A(t,x)$ is a useful indicator of how far from horizon formation the gravitational system is at a given time slice. The example plotted in Fig.5.11a suggests that the maxima of the EE do not necessarily relate to the minima of $A(t,x)$. Since extremal surfaces do not lie in a constant t slice in our dynamical geometries, we have to analyze what region they explore deep in the bulk before reaching the previous conclusion. For the same example, Fig.5.11b shows a projection on the (t,x) plane of the surfaces whose area gives the EE maxima of large caps in the last pre-horizon cycle. They stay indeed well before the time slice where the value of A drops to zero, $t_h \sim 11$. The area of a surface seems to be maximized by a competition between reaching deep in the bulk and keeping outside the traveling shell. After the weak turbulence mechanism has acted on the scalar pulse, the area maximizing configuration arises slightly before A drops to its minimal value. Indeed, the minima along the time evolution of A describe a different situation: the moments at which a well localized peak of the scalar profile is at its closest approach to the origin. Hence the entanglement entropy turns out not to be precisely correlated with the moment at which a horizon emerges. In particular, it decreases the instants before an apparent horizon first forms.

It is interesting to describe the behavior of the extremal surfaces with respect to the t slicing. As long as they do not reach the scalar shell, they live on slices of constant t. If an extremal surface intersects a fraction of the falling pulse, the part involved deviates from constant t towards smaller values of the time coordinate. On the contrary, it deviates towards bigger values when it intersects a fraction of the pulse travelling towards the AdS boundary. This is the case in Fig.5.11b where the projections in the (t,x) plane show that

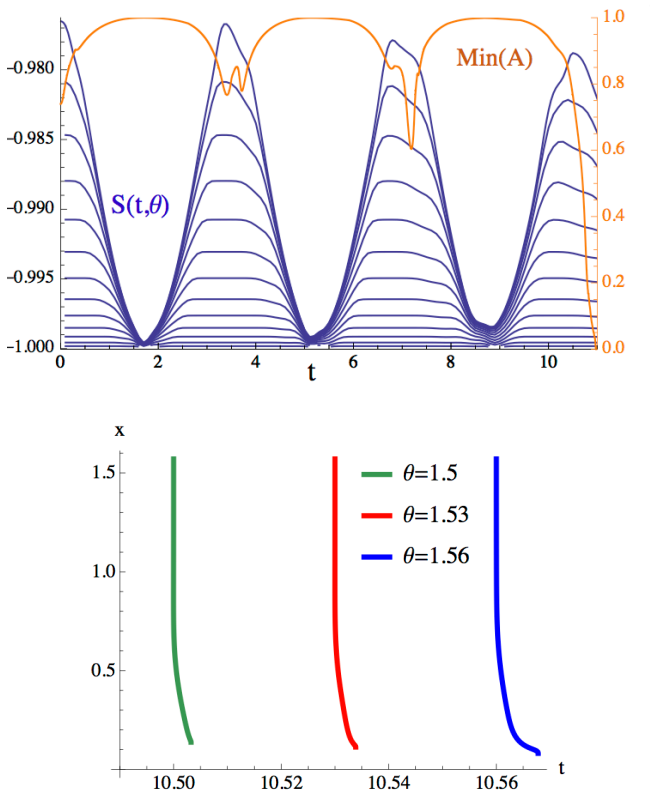

Figure 5.11: Scalar profile (5.9) with $\sigma = 0.1$ and $M = 0.012$. Left: Evolution of the EE for caps with $\theta = .5, \ldots, 1.5$. We have superposed in orange the minimal radial value of $A(t, x)$. Right: Projection on the (t, x) plane of the surfaces responsible for the EE maxima of large caps in the last bouncing cycle before the horizon forms.

the extremal surfaces tilt towards larger values of t at their inner portion. Indeed, they reach the part of the scalar profile not trapped by the emerging horizon, and which has started to move away from the origin before the horizon neatly forms.

We have plotted in Fig.5.12 the post-horizon evolution of the entanglement entropy. Using a grid of 7×10^4 points we could complete five oscillations beyond horizon formation with a mass loss below 3%. The oscillations of entanglement entropy neatly reflect the impact of the horizon, decreasing their amplitude at a pace correlated with the approach of the horizon to its final value. The maxima of the EE, whose value dropped along the pre-horizon phase, should rise to the result prescribed by a black hole of the total mass. Indeed, we observe that the maxima slowly but monotonically increase along the post-horizon cycles. The green dashed line in Fig.5.12 signals the value that the EE of a $\theta = 1.5$ cap should reach. Its slight decrease just reflects that we did have into account the small mass loss of the numerically simulation.

The traveling pulse keeps radial localization along the first five post-horizon cycles.[8]

[8] Radial localization is manifest in the time span of the oscillations, which is close to π before and after a horizon first forms. In spite of this, the radial spread of the profile progressively increases (recall Fig.5.4a for a similar example). This can be detected in the emergence of a small modulation in the EE with a

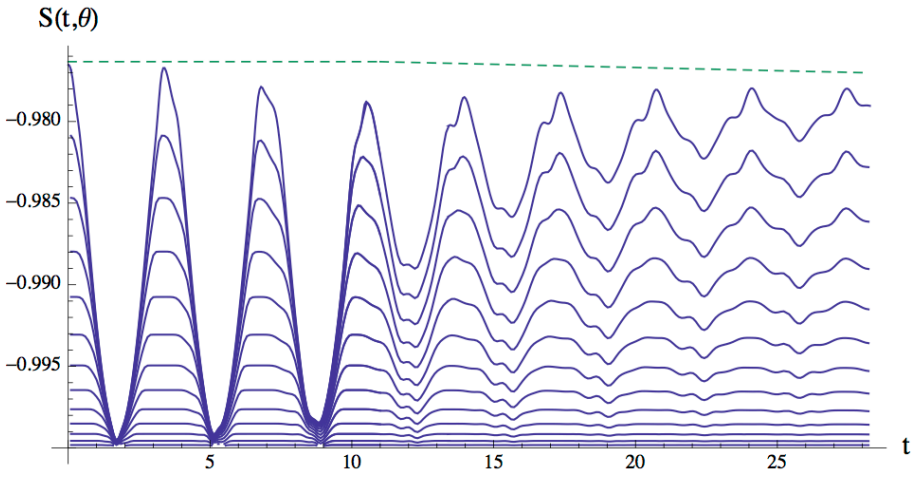

Figure 5.12: Post-horizon evolution of the EE for the same case plotted in Fig.5.11. The time for the first collapse is $t_h \sim 11$, and at around $t = 28$ the horizon radius is 83% of its final value. The green line gives $S(\theta = 1.5)$ for a static black hole of the total mass, where we did have into account the numerical mass loss along the evolution.

Following the argumentation in Section 3, this suggests that while part of the system dephases in correspondence with the appearance of an apparent horizon, part of it still retains quantum coherence. Moreover, a typical separation could be associated to the remaining entangled degrees of freedom, linked to the radial position of the pulse. Thus a pattern emerges in which the system undergoes a stepwise loss of quantum coherence, triggered by the dephasing of a subset of the degrees of freedom.

Before closing this section, we would like to draw attention to the striking similarity between the oscillations in EE shown in Fig.5.12, and those of a different, albeit also non-local, operator of the XY quantum spin chain studied in [92] (see Fig.1).

5.3.3 Behavior across critical points

A very relevant characteristic in the collapse of narrow pulses is that the fraction of energy in the sharp front which generates the horizon can become arbitrarily small. The transition between processes with n and $n+1$ bounces happens indeed as the energy of the trapped front vanishes. Therefore, it becomes relevant to investigate the behavior of the entanglement entropy across these critical collapses. The question we want to answer is whether the appearance of a horizon, no matter how small, leaves an imprint in the posterior evolution of the entanglement entropy. On line with the results in the previous subsection, the answer we find is negative.

In Fig.5.13a we plot the evolution of the radial minimum of $A(t, x)$ for two initial profiles (5.9) with broadness $\sigma = 0.1$ and masses $M = 17.324$ and $M = 17.32$. The former generates a horizon after two bounces with radius $x_h = 0.0025$, which is 4.4% of the Schwarzschild radius associated to its total mass. A trapped horizon emerges for the latter after three bounces with a radius one order of magnitude larger, $x_h = 0.02$, which is 35%

shorter period, consistent with $\pi/3$.

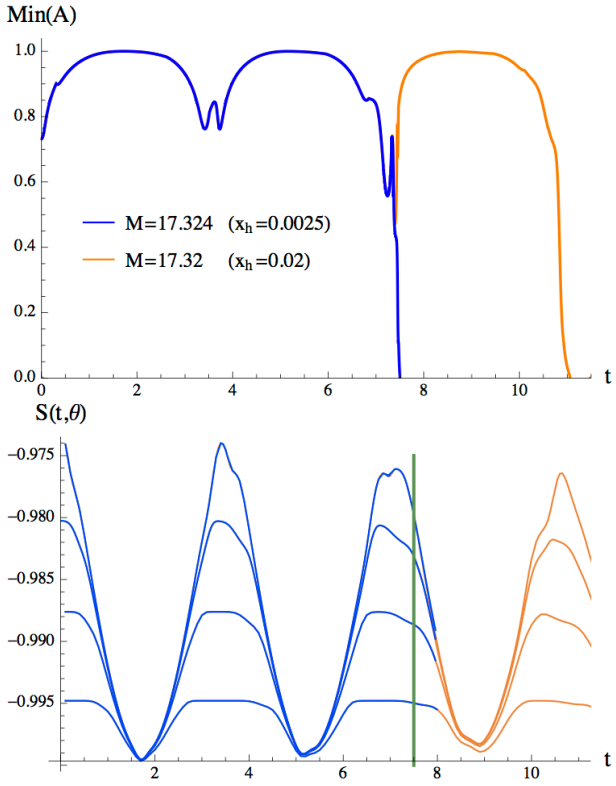

Figure 5.13: Two pulses with $\sigma = 0.1$ and masses slightly above (blue) and below (orange) critical collapse. Left: minimal radial value of $A(t, x)$. Right: EE evolution for caps with $\theta = 0.9, 1.2, 1.4, 1.56$. The green line marks horizon formation time for the above critical pulse.

of its corresponding Schwarzschild radius. Hence the masses of the two profiles are close to the critical value for the transition between two and three bouncing pre-horizon cycles, being the former slightly above and the latter slightly below. Pursuing the evolution of the profile above critical past the time when the value of A abruptly drops, at $t_h \sim 7.5$, is numerically very demanding. With a grid of 10^5 points we could only prolong one further time unit while keeping within an acceptable precision.

As can be seen in Fig.5.13b, there is no difference between the oscillations of the entanglement entropy in the two cases, both before t_h and shortly afterwards, even for spherical caps very close to a hemisphere.

5.3.4 Dependence on the initial state

We analyze now how the evolution of the entanglement entropy is influenced by the shape of the scalar profile, which according to our arguments mainly relates to the entanglement configuration of the initial state. We have focussed above on sharply localized pulses. We will consider now the effect of an increasing broadness by taking as example the two pulses studied in Fig.5.5, of broadness $\sigma = 0.25$ and $\sigma = 0.6$.

The $\sigma = 0.25$ pulse exhibits some degree of radial localization previous to the emer-

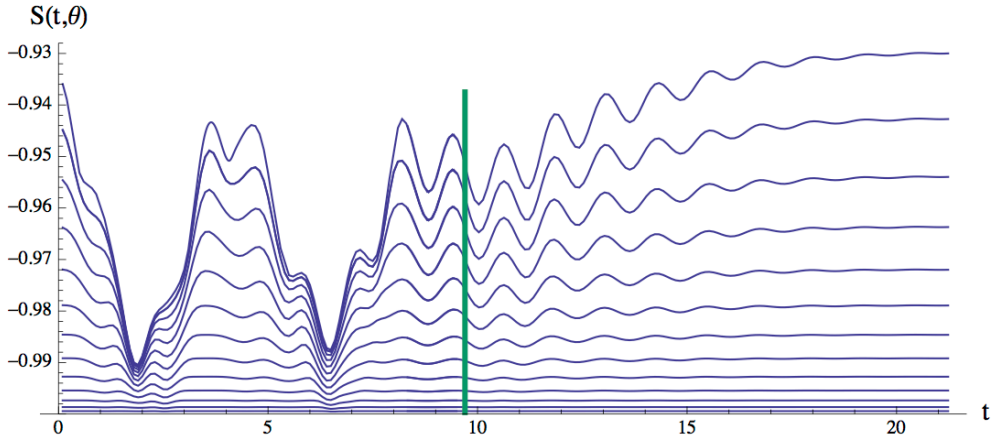

Figure 5.14: EE evolution to its equilibrium values for caps $\theta = .5, .., 1.5$ derived from an initial scalar profile (5.9) with $\sigma = 0.25$ and $M = 0.036$. The time at which $\min_x A(t,x) < 0.006$ has been signaled in green.

gence of an apparent horizon, while its post-horizon dynamics is that of a quasi-standing wave (see Fig.5.5a). These two regimes are clearly distinguished by the entanglement entropy, which we show in Fig.5.14. The green line signals the time at which the radial minimum of $A(t,x)$ drops below 0.006: $t_h \sim 9.7$. Before t_h the EE oscillates with a period of roughly 4.5 units (hence $> \pi$), and moreover its value at the local maxima decreases along the evolution. On top of these characteristic features of narrow pulses, the emergence of a shorter modulation can be clearly appreciated. After t_h only oscillations with a periodicity close to $\pi/3$, proper of a radially delocalized dynamics, are present. They are in one to one correspondence with the minima of A shown in the inset of Fig.5.5a. The damped nature of the post-horizon evolution is reflected in the decrease of the EE oscillation amplitude. Its maxima monotonically approach the equilibrium value corresponding to a Schwarzshild black hole of the total scalar profile mass. The approach is more efficient in this case than in the narrow pulse of Fig.5.12, which retains some radial localization along the post-horizon evolution.

The $\sigma = 0.6$ pulse in Fig.5.5b is radially delocalized along its complete evolution. Its mass is 40% the threshold mass for large AdS_4 black holes. Hence it develops quite massive subpulses, that delay in climbing their gravitational potential. This favors the recombination of subpulses into a single very broad peak, as can be observed in the first two snapshots of Fig.5.15a. At some point this dynamics gives way to the establishment of a strongly damped oscillation. It happens at $t \sim 7$ for the example in Fig.5.15a. The third snapshot of the mass distribution profile corresponds to this regime. The minimum radial value of $A(t,x)$ drops below 0.006 at $t_h \sim 11$, when practically the complete scalar pulse has been trapped by the emergent horizon.

The evolution of the entanglement entropy for this pulse is shown in Fig.5.15b. The EE maxima do not decrease along the evolution. The amplitude of the EE oscillations starts decreasing once the damped quasi-stationary regime sets in. At t_h the EE has practically reached its equilibrium values. Throughout the complete evolution the oscillations have invariably a period $\gtrsim \pi/3$.

Finding a qualitative field theory explanation for this period seems difficult. Its

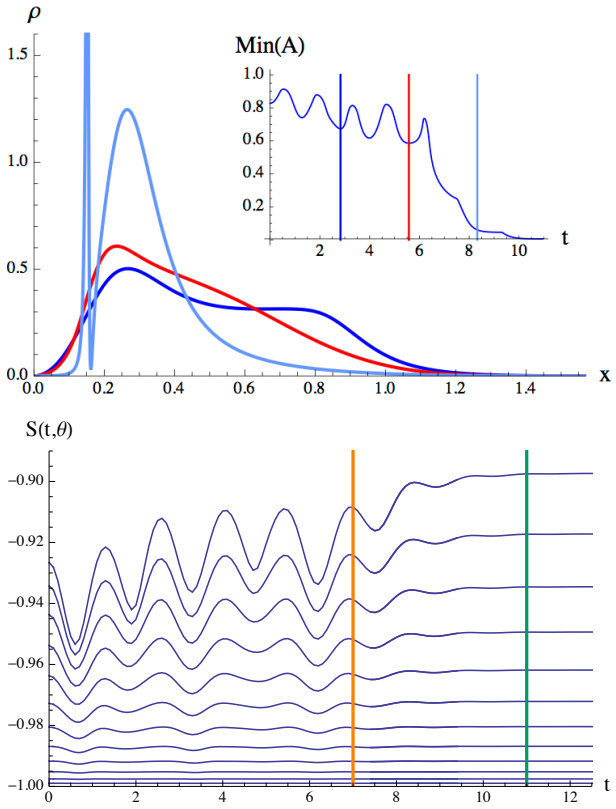

Figure 5.15: Initial profile (5.9) with $\sigma = 0.6$ and $M = 0.1538$. Left: three snapshots in the evolution of the scalar pulse. Right: EE for caps $\theta = .5, .., 1.5$. The time at which the quasi-stationary regime sets in has been signaled in orange and t_h in green.

gravitational origin is in the internal dynamics of the scalar profile rather than on the radial propagation. From the field theory point of view, this hints towards having its root in the strong coupling dynamics of the out of equilibrium plasma.

We have argued that the collapse of narrow pulses describes a stepwise relaxation process, triggered by the dephasing of a subsystem. The evolution of broad pulses suggests a quite different mechanism. The dynamics leading to the strongly damped oscillations involves in this case the whole system. We proposed in Section 3 that broad pulses correspond configurations with entangled excitations over many length scales. Hence we conclude that, in such situation, dephasing triggered by a subsystem is disfavored. Moreover, when the mass of a broad pulse drops below a certain threshold no horizon appears to be formed [102]. This would indicate that reaching a stationary state is harder for states of small energy when this involves the complete system, than when it affects only a subsystem. For the former case, and under the assumption of a spherically symmetric collapse, below a certain energy density the dual field theory system seems to never lose quantum coherence.

6 Spectrum

We consider again solutions of the self gravitating scalar field found in the previous chapter and study further details of the collapsing process by defining spectral decompositions of the scalar field and the energy and tracking their evolution.

6.1 Oscillons

In this section we review the construction of the basis of oscillons, the eigenfunctions of the linearized problem that form the basis in which to define the spectral decompositions.

Consider a scalar field ψ in AdS with no backreaction on the metric [87]. The equation of motion is:

$$(\Box - \mu^2)\psi = 0 \tag{6.1}$$

Imposing separation of variables, the angular part is given by eigenfunctions of the laplacian in S^2 (spherical harmonics $Y_{\ell m}(\Omega)$):

$$\psi(t, x, \Omega) = \sum_{k,\ell,m} \phi_{k\ell m}(t, x) Y_{\ell m}(\Omega) \tag{6.2}$$

For the other variables one obtains the equation:

$$(\partial_t^2 + L)\phi(t, x) = 0 \tag{6.3}$$

With

$$L = -\frac{1}{\tan^{d-1} x}\partial_x \left((\tan^{d-1} x)\partial_x\right) + \frac{\mu^2}{\cos^2 x} + \frac{\ell(\ell + d - 2)}{\sin^2 x} \tag{6.4}$$

Where μ is the mass of the scalar field and ℓ is the angular momentum of the spherical harmonic. For our massless, spherically symmetric case, $\mu = \ell = 0$, which will be considered from now on.

Further separating variables, $\phi(t, x) = T(t)X(x)$, we obtain:

$$T''(t) = -\omega^2 T(t) \tag{6.5}$$

$$LX(x) = \omega^2 X(x) \tag{6.6}$$

Hence, the time part is a purely oscillatory term with a frequency ω, which is an eigenvalue of the operator L. This, in turn, is a self-adjoint operator in the space $L^2(dx \tan^{d-1} x, [0, \pi/2])$. Its eigenfunctions $\varphi_j(x)$ are the *oscillons*, with corresponding eigenvalues ω_j^2, such that

$L\varphi_j = \omega_j^2 \varphi_j$. The solution of the spherically symmetric scalar field in fixed AdS background is expressed as a superposition of products of oscillons and harmonic functions:

$$\phi(x,t) = \sum_{j=0}^{\infty} \alpha_j \cos(\omega_j t + \beta_j)\varphi_j(x) \tag{6.7}$$

The eigenvalues and the eigenfunctions are:

$$\omega_j^2 = (d+2j)^2 \tag{6.8}$$

$$\varphi_j(x) = \mathcal{N}_j^{(d)} \cos^d x \ {}_2F_1(-j, d+j, \frac{d}{2}; \sin^2 x) \tag{6.9}$$

With the normalization constants $\mathcal{N}_j^{(d)}$ for AdS_{d+1} given by:

$$\mathcal{N}_j^{(2)} = 2\sqrt{j+1} \tag{6.10}$$

$$\mathcal{N}_j^{(3)} = 4\sqrt{\frac{(j+1)(j+2)}{\pi}} \tag{6.11}$$

Which ensure that the oscillons are orthonormal, $(\varphi_i, \varphi_j) = \delta_{ij}$, under the inner product

$$(f,g) = \int_0^{\pi/2} dx \tan^{d-1} x \ f(x)g(x) \tag{6.12}$$

Hence the oscillons form an orthornomal basis of $L^2(dx \tan^{d-1} x, [0, \pi/2])$ and any function $F(x)$ in this space can be expanded as:

$$F(x) = \sum_{j=0}^{\infty} F_j \varphi_j(x) \ , \quad \text{with } F_j = (\varphi_j, F) \tag{6.13}$$

Furthermore, the Parseval identity will be useful, which, much like Pythagoras theorem, it allows expressing the squared norm of a vector as the sum of the squares of its components in an orthogonal basis:

$$||g||^2 = \int_0^{\pi/2} dx \tan^2 x \ g(x)^2 = \sum_{j=0}^{\infty} g_j^2 \ , \quad \text{with } g_j = (\varphi_j, g) \tag{6.14}$$

6.2 Spectrum of the scalar field

As the oscillons are solutions for the equation for a probe scalar field, it is natural to project the solutions for a backreacted gravity background on that same basis:

$$\phi(t,x) = \sum_{j=0}^{\infty} f_j(t)\varphi_j(x) \ , \quad \text{with } f_j(t) = (\varphi_j, \phi) \tag{6.15}$$

We consider also the derivatives of the oscillons conveniently normalized:

$$\eta_j(x) \equiv \frac{1}{\omega_j}\varphi_j'(x) \tag{6.16}$$

Such that it holds $\int_0^{\pi/2} dx\ \eta_1(x)\eta_2(x) = \delta_{ij}$. These functions are useful to express the derivatives of the field, which are the dynamical variables to which we changed to solve numerically the system in (5.3). We have:

$$\dot{\phi}(t,x) = \Pi(t,x)A(t,x)e^{-\delta(t,x)} = \sum_{j=0}^{\infty} f_j'(t)\varphi_j(x) \tag{6.17}$$

$$\phi'(t,x) = \Phi(t,x) = \sum_{j=0}^{\infty} f_j(t)\omega_j\eta_j(x) \tag{6.18}$$

Then the spectral coefficients and their time derivatives are obtained by projecting in the corresponding basis:

$$f_j'(t) = (\varphi_j, \Pi A e^{-\delta}) \tag{6.19}$$

$$f_j(t) = \frac{1}{\omega_j}(\eta_j, \Phi) \tag{6.20}$$

Let us describe the evolution of the scalar ϕ in terms of its spectral series f_j. The initial configurations (5.9) and (5.10) have $\Phi = 0$ but $\Pi \neq 0$. This implies through (6.17) and (6.18) that the initial conditions we are using for the spectral series are

$$f_j(0) = 0 \tag{6.21}$$

$$f_j'(0) \neq 0 \tag{6.22}$$

In Figure (6.1) some initial configurations $f_j'(0)$ corresponding to different parameters (ϵ, σ) are shown . The broadness of a profile is captured by the location $j_{\max}$ of the maximum of f_j. For broad pulses $j_{\max} = 0$.

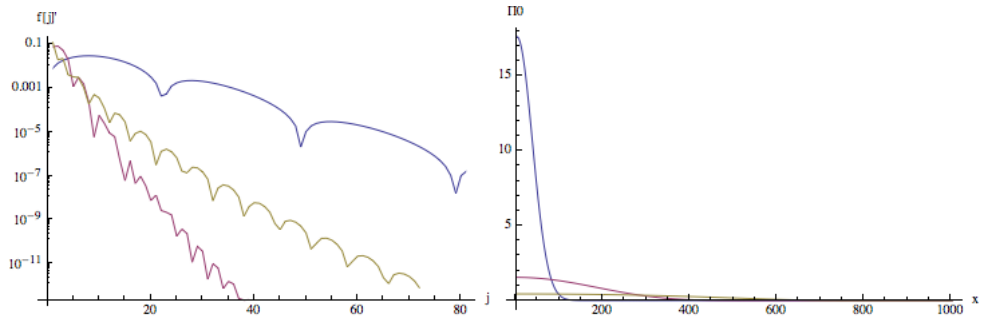

Figure 6.1: Left: Spectrum $f_j'(0)$ for three initial configurations of the form (5.9). They all have the same mass $M = 0.01$, and broadness $\sigma = 0.05$ (blue), $\sigma = 0.25$ (red) and $\sigma = 0.65$ (yellow). Right: the corresponding profiles of the scalar field.

Some general aspects of the spectral series can be outlined. Concerning the distribution in the order of the mode, it is observed how the dynamics tends to make the $f_j(t)$, at a given time t, a oscillatory series in j, with sharp minima and smooth maxima which fit, for high enough j, to curves $e^{-a(t)j+b}$, with $a(t) > 0$. The excitation of higher modes, measured by the approach of the function $a(t)$ to zero, takes place in different fashions depending on the broadness of the scalar pulse, showing that it is related to the self interaction of the scalar field.

The distributions corresponding to $f_j'(t)$ show the same behaviour than that of $f_j(t)$. Curiously, the corresponding envelope $e^{-a(t)j+b}$ is the same for narrow pulses. For broad pulses only a is approximately the same for both $f_j(t)$ and $f_j'(t)$ but b is not. This is shown in Figure 6.2.

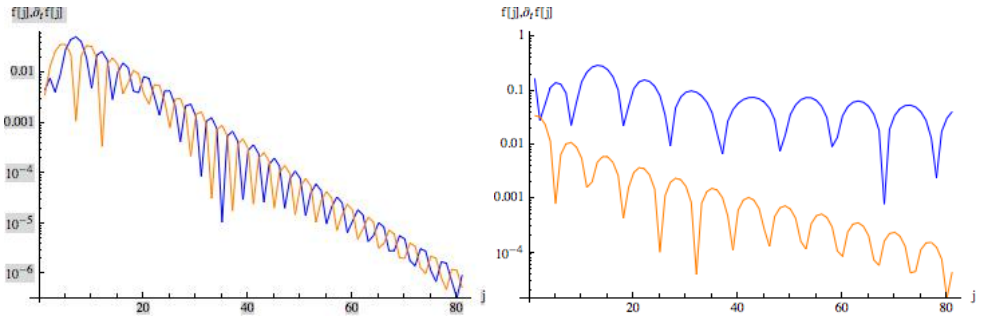

Figure 6.2: Left: Plot of $f_j(t)$ (blue) and $f_j'(t)$ (orange) at a some given time for a narrow profile of $\sigma = 0.09$. They both adjust to the same envelopes. Right: Plot of $f_j(t)$ (blue) and $f_j'(t)$ (orange) at a some given time for a broad profile of $\sigma = 3$.

We show below the time evolution of some singles mode. Low order modes at the first stages of the evolution oscillate harmonically at a frequency $\mathcal{O}(\varepsilon^2)$-shifted from that of the corresponding oscillon [90]. Then the frequency shows a smooth dependence on t. At these levels the nonlinearities reflect mainly in a modulation of the amplitude with time. That the amplitude of the low levels grows or not is a characteristic specific for narrow and broad pulses respectively, as seen in Figures 6.4, 6.6, 6.7 and 6.9.

The shape of the evolution of the modes shows reminiscences of the form $\sum_k A_k \cos(\Omega_k t)$ [101]. We find that for low modes there is a dominant frequency related to that of the corresponding oscillon. For some value of j this frequency starts to be irrelevant as the value of $f_j(t)$ does not pass through zero twice per period associated to this frequency, see Figure (6.3). This value of j increases as the amplitude of the initial profile decreases. The highest modes are not oscillatory and are excited abruptly.

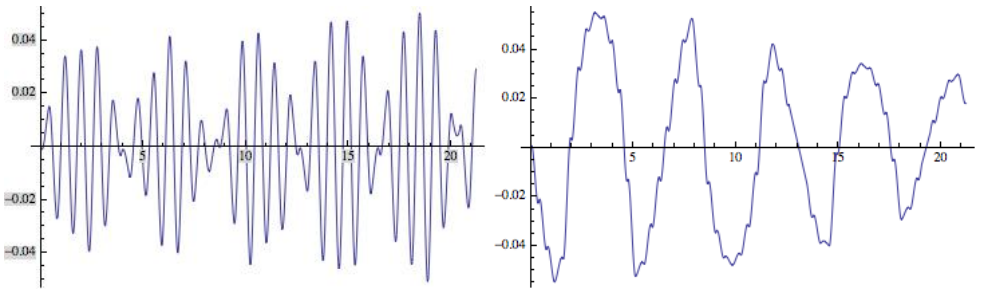

Figure 6.3: For a narrow profile of $\sigma = 0.09$. Left: Evolution of the 5th mode. At around $t = 4$ we see the first corrupted oscillation. Right: Evolution of the 8th mode, where the main frequency is much lower than that of the oscillon of the same order.

6.2.1 Narrow pulses

The global maximum of the distributions f_j and f_j' for a narrow scalar profile is at some $j_{\max} > 0$. The location $j_{\max}$ of the maximum remains approximately constant, while the modes below $j_{\max}$ become slightly excited along the evolution. The evolution of the lowest mode has been plotted in Figure 6.4, where it can be seen the increase in amplitude along the evolution.

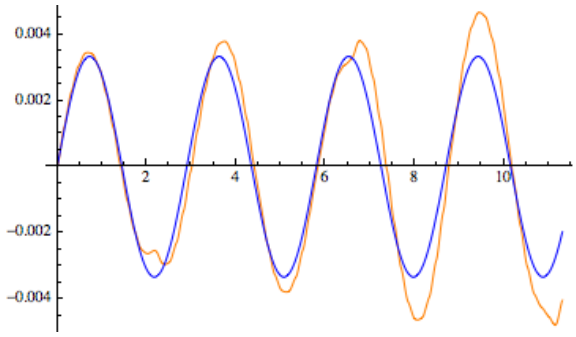

Figure 6.4: The orange curves represents the evolution of the mode $j = 0$ for a narrow pulse. The blue curve is the harmonic function of the corresponding oscillon with a phase shift: $\cos((\omega_0 + k\varepsilon^2)t)$, plotted for comparison. $\varepsilon = 0.07$ and $k \approx 170$.

For $j > j_{\max}$ the maxima of the distribution soon define an envelope of the form

$$f_j(t) \sim e^{-a(t)j} \tag{6.23}$$

As defined by this function, the approach of $a(t)$ to zero signals the excitation of high modes. The transfer of energy to the higher modes is enhanced by the self interaction of the field through its coupling to gravity. It can be seen in Figure (6.5) how $a(t)$ remains constant when the pulse is moving freely or bouncing with the AdS boundary, having a stepwise decay at the moments when the pulse collides with itself in the center of AdS. The decay is steeper in the first collisions and decreases exponentially with time.

Concerning single mode evolution, it is interesting to study also trajectories in the phase space. Since we have a second order differential problem for the spectral coefficients $f_j(t)$, the infinite dimensional phase space is spanned in $\{f_j(t), f_j'(t)\}$. We plot in Figure (6.6) some sections that correspond to the trajectories of some single modes.[1] We distinguish three kinds of trajectories for narrow pulses, consistently with the evolution described by (6.23) Low modes trace curves not very different of ellipses, but with an amplitude that increases along the evolution. The trajectories of intermediate modes, those around the maximum in the distribution at $t = 0$, remain at a bounded amplitude. Finally, high modes evolve chaotically, not even describing well defined oscillations, and always with a growing amplitude. In general, the trajectories in phase space present spikes in the beginning and they are smoothened along the evolution.

[1] In the linearized system the trajectories are ellipses with ω_j being the ratio between the semiaxis.

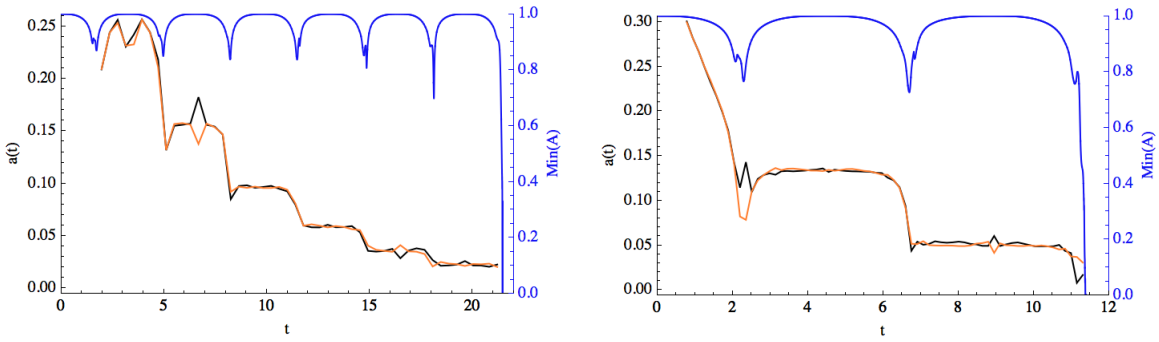

Figure 6.5: Evolution of the function $a(t)$ in (6.23) for $f_j(t)$ (black) and $f_j'(t)$ (orange) for two different narrow pulses that collide in the center of AdS seven times (left) and three (right) . The minimum of A, represented by the blue curve, shows clearly how the variation of $a(t)$ is associated to self interaction of the scalar field.

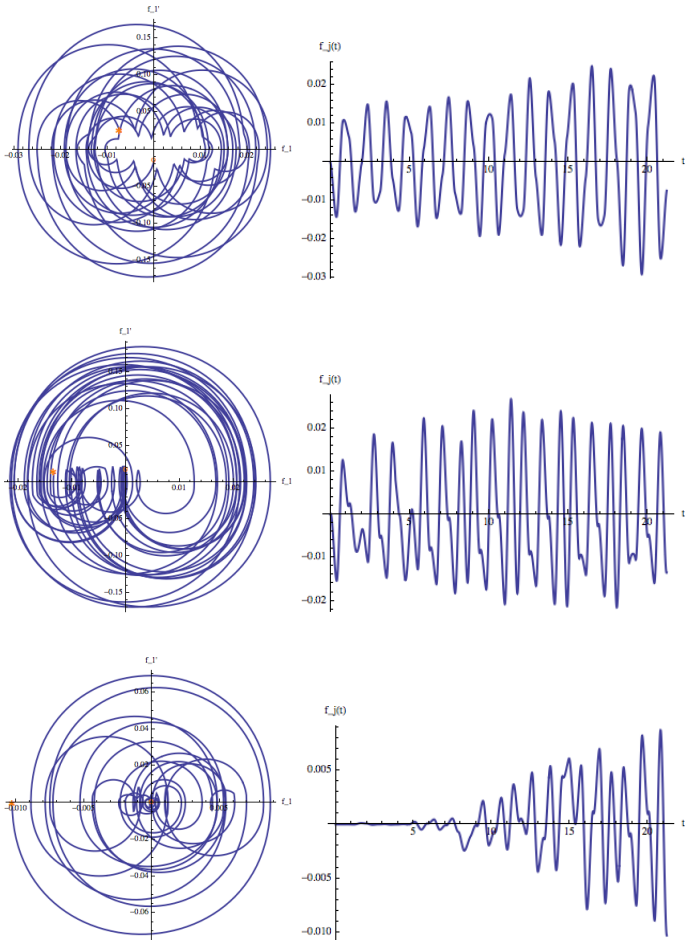

Figure 6.6: Evolution of single modes for the narrow pulse of $\sigma = 0.09$ in phase space (f_j, f_j') (left) and only the component $f_j = f_j(t)$ (right). Plots correspond from top to bottom to $j = 2$, 14, 38 as representatives of the regimes mentioned in the text.

6.2.2 Broad pulses

Contrary to what happens for narrow pulses, the lowest modes for broad pulses decrease along the evolution, as shown in Figure 6.7.

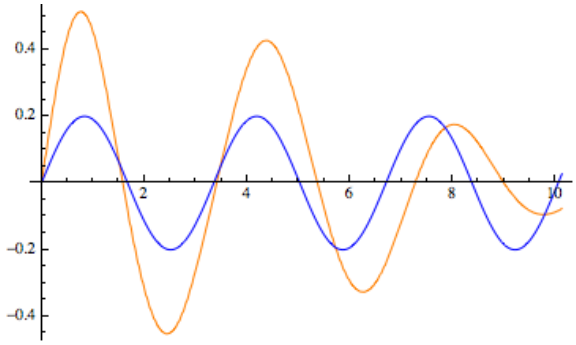

Figure 6.7: The orange curves represents the evolution of the mode $j = 0$ for a broad pulse. The blue curve is the harmonic function of the corresponding oscillon with a phase shift: $\cos((\omega_0 + k\varepsilon^2)t)$, plotted for comparison. $\varepsilon = 3$ and $k \approx 1/8$.

The series of local maxima of the spectral series at a given time fits well to a function $e^{-a(t)j}$ for high enough j. As before, the approach of $a(t)$ to zero gives a measure of how higher modes become excited during the gravitational evolution. An instance of this process has been plotted in Figure (6.8). Comparing with Figure (6.5) we observe that $a(t)$ evolves completely different: it is not a stepwise approach at all, and at some stages $a(t)$ can even increase. This agrees with the interpretation that the self interaction of the scalar pulse, which is more intense during the shocks at the origin for narrow pulses, is responsible for the transfer of energy to higher modes. For broad pulses, according with the description of the previous chapter, the energy is spread in space and there are no well defined shocks at the center of AdS but continuous interactions associated to internal infalling and outgoing components within the pulse.

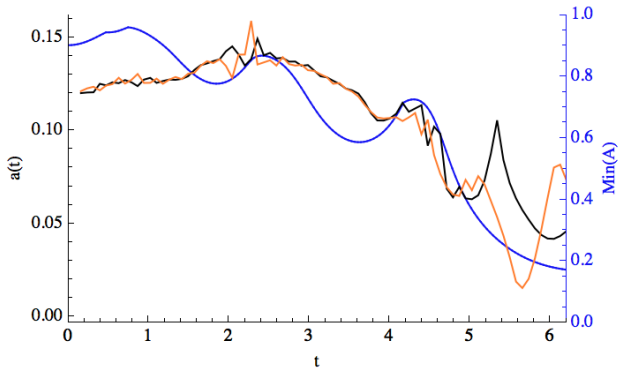

Figure 6.8: Evolution of the function $a(t)$ in (6.23) for $f_j(t)$ (black) and $f_j'(t)$ (orange) for a broad pulse. The minimum of A is represented by the blue curve.

Trajectories in phase space for broad pulses lowest modes are damped along the

evolution, while high modes suddenly increase their amplitude, see Figure (6.9). There are not seem to be modes in an intermediate regime where the amplitude does not vary much, as found for narrow pulses.

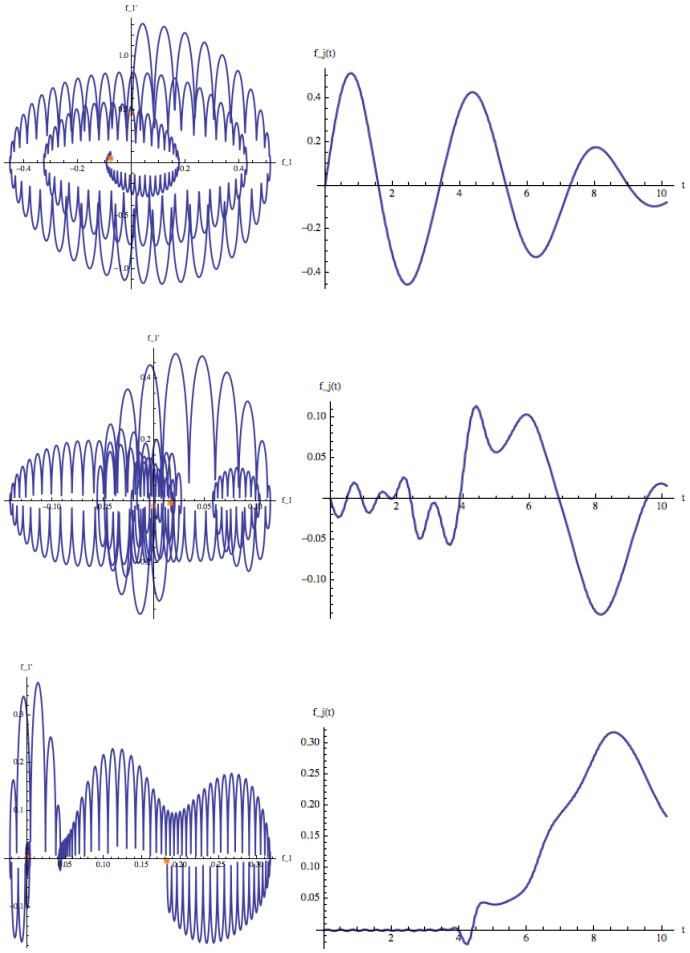

Figure 6.9: Evolution of single modes in phase space (f_j, f_j') (left) and only the component $f_j = f_j(t)$ (right). Plots correspond from top to bottom to $j = 0$, 4, 12.

6.3 Spectrum of the Conserved Mass

For the conserved mass of the spacetime we use the following expression:

$$M = \frac{1}{2}\int_0^{\pi/2} dx \tan^2 x \; A(x,t)\left(\Pi(x,t)^2 + \Phi(x,t)^2\right) \tag{6.24}$$

As this quantity is computed by integrating over space with the weight $\tan^2 x$, it fits to a Parseval formula of the form (6.14). and it can be expanded in oscillons:

$$M = \sum_{j=0}^{\infty} m_j^2(t) \quad , \quad m_j(t) = (\varphi_j, \rho) \tag{6.25}$$

The conserved mass contains two components, one with the Π field and the other with Φ, $M = M^{\Pi} + M^{\Phi}$. As with the scalar field, we use the φ_j and η_j in (6.16) [90]. The energy modes E_j are defined:

$$E_j^2 = E_{\Pi,j}^2 + E_{\Phi,j}^2 \quad , \quad \begin{cases} E_{\Pi,j} &= (\varphi_j, \frac{1}{\sqrt{2}}\sqrt{A}\Pi) \\ E_{\Phi,j} &= (\eta_j, \frac{1}{\sqrt{2}}\sqrt{A}\Phi) \end{cases} \tag{6.26}$$

Some similar features as those found for the spectrum of the scalar field are identified. In particular for the present purposes, we note that the variation of the modes happens when the pulse is close to the origin, as shown in Figure 6.10.

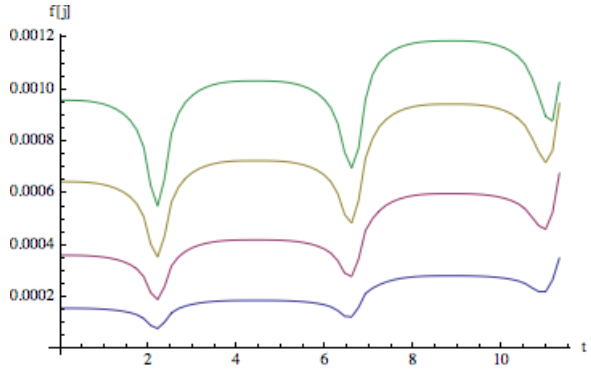

Figure 6.10: Evolution of modes E_2, E_3, E_4 and E_5 for a narrow pulse that requires three shocks at the origin to collapse.

6.4 Spectral decomposition of the Mass Aspect Function

For the general metric (5.2) we consider a generalization of the mass of a static black hole. For this aim, we equate the $g_{xx}(t,x)$ term of (5.2) and the same metric component of an AdS-Schwarzschild black hole with a non constant mass $\mathcal{M}(t,x)$, the mass aspect function:

$$\mathcal{M}(t,x) = \frac{\sin x}{2\cos^3 x}\left(1 - A(t,x)\right) \tag{6.27}$$

This accounts for the total energy at time t in the interval $[0,x]$. At $x = \pi/2$ it gives the ADM mass M of the spacetime, $\mathcal{M}(t,\pi/2) = M$. For a Schwarzschild black hole $\mathcal{M}(t,x) = M$, consistently with the assumption that all the mass is at the singularity at $x = 0$.

The mass aspect function can be formally expanded in the oscillons basis:

$$\mathcal{M}(x,t) = \sum_{j=0}^{\infty} \mu_j(t)\varphi_j(x) \quad , \quad \mu_j(t) = (\varphi_j, \mathcal{M}) \tag{6.28}$$

For a static black hole of mass M we expand:

$$M = \sum_{j=0}^{\infty} \mu_j^{(\mathrm{Sch})}\varphi_j(x) \quad , \quad \mu_j^{(\mathrm{Sch})} = (\varphi_j, M) \tag{6.29}$$

To obtain:

$$\mu_j^{(\mathrm{Sch})} = (-1)^j \frac{4}{3+2j}\sqrt{\frac{(j+2)(j+1)}{\pi}}M \tag{6.30}$$

A plot of this series is in Figure (6.11). The asymptotic value for large j is:

$$\lim_{j\to\infty} \mu_j^{(\mathrm{Sch})} = \frac{2}{\sqrt{\pi}}M \tag{6.31}$$

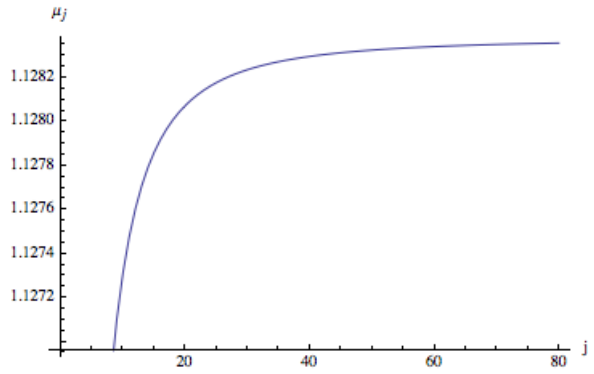

Figure 6.11: Plot of $\mu_j^{(\mathrm{Sch})}$ for a mass $M = 1$.

The evolution of some low and high modes has been plotted in Figure 6.12 for the evolution of a narrow pulse. All modes oscillate around the series $\mu_j^{(\mathrm{Sch})}$ of a black hole of the same mass. Low modes oscillate accompanying the bounces of the pulse and high modes are turned on after some time. The amplitude of oscillation along the evolution is bigger as the order of the mode is lower. The times of the shocks coincide with when the amplitude of the oscillations of the high modes is bigger.

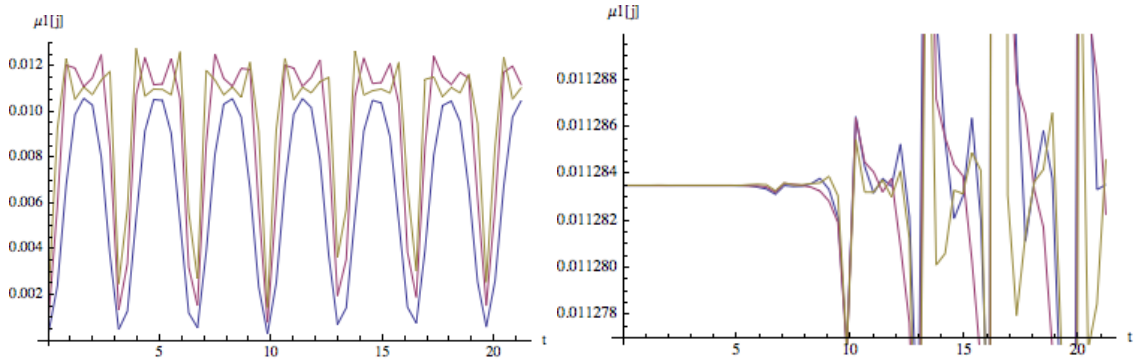

Figure 6.12: Plot of $\mu_j(t)$ for j=0, 1, 2 (left), and j=70, 71, 72 (right), for a narrow profile with $\sigma = 0.07$.

7

Conclusions / Conclusiones

The entanglement entropy, computed according to the holographic proposal [3] [4], has been the main character along this work. It has been calculated for two different gravitational collapse scenarios, and it has allowed confirming and predicting results regarding to the equilibration dynamics of the dual quantum systems. Gravitational collapse in AdS has thus confirmed as an appropriate holographic model of thermalization of a quantum system.

The difficulties overcome to get the present results had their origin mainly in the numerical computations required to solve the involved equations. Shooting and relaxation methods have been used to solve the extremization equations with prescribed boundary conditions that define the surface related to the holographic entanglement entropy. In addition, solving the scalar-gravity system has required a lot of effort to attain the necessary stability and convergence. At each slice of constant time, equations have been solved using four points stencils integrators. A fourth order Runge-Kutta method has been used to advance in time. Boundary points have demanded a special care, and ghost points have extended the interval according to the power series form of the corresponding solution, as well as dissipation routines for the propagation of numerical errors have been implemented.

In Chapter 4 it was used the Vaidya metric in Poincaré coordinates in AdS_3 as a first holographic model of thermalization. The behaviour of the holographic entanglement entropy reproduced the one found for the quantum quench dynamics of two dimensional CFTs in [5], essentially characterized by a causal propagation of the quasiparticles sourced by the perturbation at a finite velocity and a local thermalization as results of it. The horizon effect has appeared with the associated expected velocity $v_E = 1$. Also the effective thermalization of subsystems smaller than $2v_E t$ has been described holographically in terms of the particular form of the geodesics in this regime, which reach very close to the horizon but do not traverse it, and their length is actually the length of the horizon (confirming at the local level of a subsystem the correspondence between its thermal entropy and the Bekenstein-Hawking entropy of the dual AdS black hole).

Moreover, the analysis of the infinite size intervals has allowed obtaining more details and has determined that after a time $\bar{t}$ this causal behavior is the only effect that drives the evolution. The early time dynamics has also been analyzed, finding that the apparent horizon does not play a relevant role at this stage. On the other side, for the later causal dynamics the spacelike geodesics relevant for the entanglement entropy contain a piece inside the horizon. The contribution to the total length due to this part grows linearly with time and accounts for the increase of the entanglement entropy in the dual subsystem as time evolves. In addition, it has been remarked how the holographic entanglement entropy proposal implies a manifest unitary evolution in collapse scenarios

dual to thermalization processes, as long as there is no singularity in the asymptotic past of the spacetime manifold.

In Chapter 5 the objective was to study holographically some aspects of the equilibration dynamics of closed quantum systems. Following the gravity works regarding instability of AdS under scalar perturbations, the aim was to further analyze the gravitational collapse process and to use holography to describe the relaxation dynamics of the dual finite size quantum systems. For small enough amplitudes, this setup contains solutions corresponding to gravitational collapse processes requiring several bounces off the AdS boundary to generate a horizon, as in [90][99]. These spacetimes have been shown able to model holographically field theory relaxation processes with large dephasing times. Contrarily, they have not proven suitable to realize evolutions with a prethermalization stage. This is consistent with the fact that this gravity system only has the mass as conserved quantity, while prethermalization is typically associated to the closeness of a system to an integrable theory [70][72][73].

It has been proposed in Chapter 5 that the radial position of the collapsing scalar shell encodes the typical separation of entangled components in the dual out of equilibrium quantum system. When the pulse is close to the boundary, entanglement is concentrated among nearby excitations. Its fall towards the interior geometry corresponds to entangled excitations moving apart, as in the holographic model for a local quench of [85]. The travel back of the shell to the boundary is then associated to the entangled components approaching again on the boundary sphere. This interpretation is aligned with works that directly link the entanglement pattern of a field theory with a higher dimensional geometry [29]. In particular, entanglement entropy is used in [30][31] as a suitable observable to translate Einstein equations into field theory language. Going further, in [119][120] the authors propose to build up a spacetime geometry from a quantum field theory state using the Multiscale Entanglement Renormalization Ansatz (MERA) [121] and its continuum version (cMERA) [122].

As in the Vaidya model, the entanglement entropy evolution follows the one of the metric, and in this case it is shown by the obtained oscillatory pattern. For narrow scalar profiles, the periodicity of the entanglement entropy oscillations is always close to π. This is indeed the time needed by the quasiparticle excitations of the dual field theory process to travel along the equator of the boundary sphere and meet again , and provides the main support for the advocated picture. Consistently, the minima of the entanglement entropy happen when the scalar shell bounces at the boundary and the maxima are reached when the shell is close to the origin.

The entanglement entropy is not only able to detect propagation, but also interaction effects related to the internal dynamics of the shell. A main characteristic of this dynamics is weak turbulence, that governs the appearance of a horizon for profiles of small mass. It has been shown how, besides the generation of a sufficiently sharp front for collapse, there is an accompanying effect of radial dispersion in the scalar profile leftover by the emerging horizon. Interestingly, this flow of energy towards opposite scales in the bulk, is reflected in a decrease of the entanglement entropy maxima along the pre-horizon evolution.

In order to get a complete picture of the field theory relaxation process, the gravitational evolution was followed until a static black hole was almost established. For narrow initial pulses, the fraction of the scalar profile escaping from the emergent horizon exhibits radial localization along several further cycles of partial absorptions and bounces against the boundary. According to the proposed interpretation, this suggests that while part of

the system has dephased, a subset of degrees of freedom maintains quantum coherence. Moreover, a typical separation can be associated to the remaining entangled components, which still evolves with a period close to π. This stepwise pattern of relaxation is an important result of the analysis.

The amplitude of the entanglement entropy oscillations neatly reflects the formation of a horizon, decreasing as the trapped mass increases. In spite of this, the emergence of an apparent horizon does not leave a sharp imprint on the entanglement entropy. Neither do the regions of its stepwise growth. Along the post-horizon evolution the entanglement entropy exhibits damped but smooth oscillations.

Finally, in Chapter 6 some details of the gravitational collapse solutions found in Chapter 5 have been given, by defining and analyzing the evolution of spectral decompositions of the scalar field and the energy. This point of view has complemented the description made in the previous chapter which considers the radial distribution of the energy pulse along the evolution. Also, the mode analysis has stressed that the non linear self interaction of the scalar field, mediated by the coupling to gravity, is responsible for the concentration of energy in smaller scales. This has been manifest for narrow pulses, which travel almost freely through AdS and the interaction takes place at the shocks in the origin. Correspondingly, the envelope of the spectral distributions is approximately constant except at the instants of the shocks, when a steep increase is observed that implies the excitation of higher modes. Broad pulses have not shown this behavior, as the transfer of energy to higher modes is disordered and continuous, which is consistent with the substructure of such pulses as described in Chapter 5, since they contain subpulses going forth and forward and thus interactions take place continuously.

Conclusiones

La entropía de entrelazamiento, calculada según la propuesta holográfica [3][4], ha sido la protagonista a lo largo de este trabajo. Ha sido calculada para dos escenarios distintos de colapso gravitatorio, y ha permitido confirmar y predecir resultados relativos a las dinámicas de alcance del equilibrio de los sistemas cuánticos duales. El colapso gravitatorio en AdS se ha confirmado por tanto como un apropiado modelo holográfico de termalización de un sistema cuántico.

Las dificultades superadas para llegar a los resultados mostrados tuvieron su origen principalmente en los cálculos numéricos requeridos para resolver las ecuaciones involucradas. Para resolver las ecuaciones de extremización con las condiciones de contorno prescritas que definen la superficie relacionada con la entropía de entrelazamiento se han utilizado métodos de disparo y de relajación. Además, para resolver el sistema escalar-gravedad ha sido necesario considerable esfuerzo para alcanzar la necesaria estabilidad y convergencia. En cada rodaja de tiempo constante se han resuelto las ecuaciones usando integradores con stencils a cuatro puntos. Para avanzar en el tiempo se ha empleado un método de Runge-Kutta de cuarto orden. Los puntos extremos han requerido de especial cuidado, y se han introducido puntos fantasma para extender el intervalo de acuerdo con la correspondiente forma de las soluciones en serie de potencias, así como se han implementado rutinas de disipación para la propagación de errores numéricos.

En el Capítulo 4 se ha utilizado la métrica de Vaidya en coordenadas de Poincaré de AdS_3 como primer modelo holográfico de termalización. El comportamiento de la entropía de entrelazamiento holográfica ha reproducido el que se encuentra en la dinámica de los quenches cuánticos de TCC de dos dimensiones [5], caracterizado esencialmente por una propagación causal de las partículas creadas por la perturbación a una velocidad finita y una termalización local a causa de eso. El efecto horizonte ha aparecido con la esperada velocidad $v_E = 1$. También se ha descrito holográficamente la termalización efectiva de subsistemas menores de $2v_E t$ en términos de la forma particular de las geodésicas en ese régimen, que están casi pegadas al horizonte pero sin atravesarlo, siendo su longitud de hecho la longitud del horizonte (confirmando al nivel local de un subsistema la correspondencia entre su entropía térmica y la entropía de Bekenstein-Hawking del agujero negro en AdS dual).

Por otra parte, el análisis de intervalos de tamaño infinito ha permitido obtener más detalles y ha determinado después de un tiempo $\bar{t}$ este comportamiento causal es el único efecto en la evolución. La dinámica de los primeros instantes de tiempo también ha sido analizada, encontrando que el horizonte aparente no juega un papel relevante en esta etapa. Por otro lado, para la posterior dinámica causal las geodésicas tipo espacio asociadas a la entropía de entrelazamiento contienen una parte dentro del horizonte. La contribución a la longitud total debida a esta parte crece linealmente con el tiempo y corresponde al aumento de entropía de entrelazamiento en el subistema dual según el tiempo evoluciona. Además, se ha remarcado cómo la propuesta de la entropía de entrelazamiento holográfica implica una evolución unitaria manifiesta en escenarios de colapso duales a procesos de termalización, siempre y cuando no exista una singularidad en el pasado asintótico de la variedad del espaciotiempo.

En el Capítulo 5 el objetivo ha sido estudiar estudiar holográficamente algunos aspectos de la dinámica del alcance del equilibrio de sistemas cuánticos cerrados. Siguiendo los trabajos de gravitación que se ocupaban de la inestabilidad de AdS bajo perturba-

ciones escalares, el objetivo ha sido analizar aún más el proceso de colapso gravitatorio y usar holografía para describir la dinámica de relajación de los sistemas cuánticos finitos duales. Para amplitudes suficientemente pequeñas este planteamiento contiene soluciones correspondientes a procesos de colapso gravitatorio que necesitan varios rebotes contra la frontera de AdS hasta que se genera un horizonte, como en [90][99]. Se ha mostrado que estos espaciotiempos son capaces de modelar holográficamente procesos de relajación de teoría de campos con tiempos de desfase largos. Por el contrario, no se ha demostrado que sean apropiados para describir evoluciones con fase de pretermalización. Esto es consistente con el hecho de que este sistema de gravedad solo tiene la masa como cantidad conservada, mientras que la pretermalización está típicamente asociada a la cercanía de un sistema a una teoría integrable [70][72][73].

Se ha propuesto en el Capítulo 5 que la posición radial de la capa escalar que colapsa está relacionada con la separación típica de las componentes entrelazadas en el sistema cuántico dual fuera del equilibrio. Cuando el pulso está cerca de la frontera, el entrelazamiento está concentrado entre excitaciones cercanas. Su caída hacia el interior de la geometría corresponde al alejamiento de las excitaciones entrelazadas, como en el modelo holográfico de quench local de [85]. El viaje de vuelta del pulso a la frontera está entonces asociado con el acercamiento de las componentes entrelazadas en la esfera de la frontera. Esta interpretación está alineada con trabajos que directamente unen el perfil de entrelazamiento de una teoría de campos con una geometría de mayor dimensionalidad [29]. En particular, la entropía de entrelazamiento se utiliza en [30][31] como un observable adecuado para traducir las ecuaciones de Einstein al lenguaje de la teoría de campos. Yendo más lejos, en [119][120] los autores proponen construir geométricamente un espaciotiempo a partir de un estado cuántico usando el Ansatz de Renormalización de Entrelazamiento a Multiescala (MERA) [121] y su versión continua (cMERA) [122].

Como en el modelo de Vaidya, la evolución de la entropía de entrelazamiento sigue la de la métrica, y en este caso esto es mostrado por el patrón oscilatorio que se encuentra. Para pulsos escalares estrechos, la periodicidad de las oscilaciones de la entropía de entrelazamiento es siempre cercana a π. Éste es de hecho el tiempo que necesitan las excitaciones del proceso dual de la teoría campos para viajar a lo largo del ecuador de la esfera de la frontera y reunirse de nuevo, y proporciona el mayor soporte de la imagen propuesta. Consistentemente, los mínimos de la entropía de entrelazamiento suceden cuando la capa escalar rebota en la frontera, y los máximos se alcanzan cuando el pulso está cerca del origen.

La entropía de entrelazamiento no es solo capaz de detectar la propagación, sino también los efectos de la interacción relacionados con la dinámica interna del pulso. Una característica principal de esta dinámica es la turbulencia débil, que gobierna la aparición de un horizonte para configuraciones con masa pequeña. Se ha mostrado cómo, además de la generación de un frente suficientemente afilado para el colapso, hay un efecto de dispersión radial en el perfil escalar que queda después del incipiente horizonte. Es interesante que este flujo de energía hacia direcciones opuestas en el interior del espacio se refleja en una disminución de la entropía de entrelazamiento durante la evolución antes de la formación del horizonte.

Para tener una descripción completa del proceso de relajación en la teoría de campos, la evolución gravitatoria se ha seguido hasta que un agujero negro estático se ha establecido prácticamente. Para perfiles iniciales estrechos, la fracción del perfil escalar que escapa del horizonte emergente muestra localización radial a lo largo de varios ciclos de absorciones

parciales y rebotes contra la frontera. De acuerdo a la interpretación propuesta, esto sugiere que mientras parte del sistema se ha desfasado, un subconjunto de grados de libertad mantiene la coherencia cuántica. Por otro lado, se puede asociar una separación típica a las componentes entrelazadas que quedan, las cuales todavía evolucionan con un periodo cercano a π. Este patrón escalonado de relajación es un resultado importante del análisis.

La amplitud de las oscilaciones de la entropía de entrelazamiento refleja claramente la formación de un horizonte, disminuyendo según la masa atrapada aumenta. A pesar de esto, la emergencia de un horizonte aparente no deja un marca clara en la entropía de entrelazamiento. Tampoco lo hacen regiones de este crecimiento escalonado. A lo largo de la evolución después de la formación del horizonte la entropía de entrelazamiento muestra oscilaciones amortiguadas pero suaves.

Finalmente, en el Capítulo 6 se han dado más detalles sobre las soluciones de colapso gravitatorio encontradas en el Capítulo 5, definiendo y analizando la evolución de descomposiciones espectrales del campo escalar y la energía. Este punto de vista ha complementado a la descripción hecha en el capítulo anterior relativa a la distribución radial del pulso de energía a lo largo de la evolución. Además, el análisis de los modos ha subrayado que la autointeracción no lineal del campo escalar, mediada por el acoplo a gravedad, es responsable de la concentración de la energía en escalas más pequeñas. Esto ha sido manifiesto para pulsos estrechos, que viajan casi libremente a través de AdS y la interacción tiene lugar en los choques en el origen. Correspondientemente, la envolvente de las distribuciones espectrales es aproximadamente constante salvo en los instantes de los choques, en los que se observa un incremento escalonado que implica la excitación de modos más altos. Los pulsos anchos no han mostrado este comportamiento, pues la transferencia de energía a modos más altos es desordenada y continua, lo cual es consistente con la subestructura de dichos pulsos, como se describe en el Capítulo 5, pues contienen subpulsos yendo y viniendo y por tanto la interacción sucede continuamente.

Bibliography

[1] J. Abajo-Arrastia, J. Aparicio and E. Lopez, *Holographic Evolution of Entanglement Entropy*, JHEP **1011**, 149 (2010) [arXiv:1006.4090 [hep-th]].

[2] J. Abajo-Arrastia, E. da Silva, E. Lopez, J. Mas and A. Serantes, *Holographic Relaxation of Finite Size Isolated Quantum Systems*, JHEP **1405** (2014) 126 [arXiv:1403.2632 [hep-th]].

[3] S. Ryu and T. Takayanagi, *Holographic derivation of entanglement entropy from AdS/CFT,* Phys. Rev. Lett. **96**, 181602 (2006) [hep-th/0603001].

[4] V. E. Hubeny, M. Rangamani and T. Takayanagi, *A Covariant holographic entanglement entropy proposal,* JHEP **0707** (2007) 062 [arXiv:0705.0016 [hep-th]].

[5] P. Calabrese and J. L. Cardy, *Evolution of entanglement entropy in one-dimensional systems,* J. Stat. Mech. **0504**, P04010 (2005) [cond-mat/0503393].

[6] J. M. Maldacena, *The Large N limit of superconformal field theories and supergravity*, Int. J. Theor. Phys. **38** (1999) 1113 [Adv. Theor. Math. Phys. **2** (1998) 231] [hep-th/9711200].

[7] E. Witten, *Anti-de Sitter space and holography*, Adv. Theor. Math. Phys. **2** (1998) 253 [hep-th/9802150].

[8] S. S. Gubser, I. R. Klebanov and A. M. Polyakov, *Gauge theory correlators from noncritical string theory*, Phys. Lett. B **428** (1998) 105 [hep-th/9802109].

[9] E. Witten, *Anti-de Sitter space, thermal phase transition, and confinement in gauge theories*, Adv. Theor. Math. Phys. **2** (1998) 505 [hep-th/9803131].

[10] G. 't Hooft, *A Planar Diagram Theory for Strong Interactions*, Nucl. Phys. B **72** (1974) 461.

[11] J. D. Brown and M. Henneaux, *Central Charges in the Canonical Realization of Asymptotic Symmetries: An Example from Three-Dimensional Gravity*, Commun. Math. Phys. **104** (1986) 207.

[12] G. 't Hooft, Salamfest 1993:0284-296 [gr-qc/9310026].

[13] L. Susskind, *The World as a hologram*, J. Math. Phys. **36** (1995) 6377 [hep-th/9409089].

[14] R. Bousso, *The Holographic principle*, Rev. Mod. Phys. **74** (2002) 825 [hep-th/0203101].

[15] D. T. Son and A. O. Starinets, *Viscosity, Black Holes, and Quantum Field Theory*, Ann. Rev. Nucl. Part. Sci. **57** (2007) 95 [arXiv:0704.0240 [hep-th]].

[16] P. Kovtun, D. T. Son and A. O. Starinets, *Viscosity in strongly interacting quantum field theories from black hole physics*, Phys. Rev. Lett. **94** (2005) 111601 [hep-th/0405231].

[17] R. Baier, P. Romatschke, D. T. Son, A. O. Starinets and M. A. Stephanov, *Relativistic viscous hydrodynamics, conformal invariance, and holography*, JHEP **0804** (2008) 100 [arXiv:0712.2451 [hep-th]].

[18] S. Bhattacharyya, V. E. Hubeny, S. Minwalla and M. Rangamani, *Nonlinear Fluid Dynamics from Gravity*, JHEP **0802** (2008) 045 [arXiv:0712.2456 [hep-th]].

[19] A. Ashtekar and B. Krishnan, *Isolated and dynamical horizons and their applications*, Living Rev. Rel. **7** (2004) 10 [gr-qc/0407042].

[20] I. Booth, *Black hole boundaries*, Can. J. Phys. **83** (2005) 1073 [gr-qc/0508107].

[21] V. Balasubramanian and S. F. Ross, *Holographic particle detection*, Phys. Rev. D **61** (2000) 044007 [hep-th/9906226].

[22] L. Bombelli, R. K. Koul, J. Lee and R. D. Sorkin, *A Quantum Source of Entropy for Black Holes*, Phys. Rev. D **34** (1986) 373.

[23] M. Srednicki, *Entropy and area*, Phys. Rev. Lett. **71** (1993) 666 [hep-th/9303048].

[24] M. M. Wolf, *Violation of the entropic area law for Fermions*, Phys. Rev. Lett. **96** (2006) 010404 doi:10.1103/PhysRevLett.96.010404 [quant-ph/0503219].

[25] J. Eisert, M. Cramer and M. B. Plenio, *Area laws for the entanglement entropy - a review*, Rev. Mod. Phys. **82** (2010) 277 doi:10.1103/RevModPhys.82.277 [arXiv:0808.3773 [quant-ph]].

[26] C. Holzhey, F. Larsen and F. Wilczek, *Geometric and renormalized entropy in conformal field theory*, Nucl. Phys. B **424** (1994) 443 [hep-th/9403108].

[27] P. Calabrese and J. L. Cardy, *Entanglement entropy and quantum field theory*, J. Stat. Mech. **0406** (2004) P06002 [hep-th/0405152].

[28] P. Calabrese and J. L. Cardy, *Entanglement entropy and quantum field theory: A Non-technical introduction*, Int. J. Quant. Inf. **4** (2006) 429 [quant-ph/0505193].

[29] M. Van Raamsdonk, *Comments on quantum gravity and entanglement*, arXiv:0907.2939 [hep-th].

[30] M. Nozaki, T. Numasawa, A. Prudenziati and T. Takayanagi, *Dynamics of Entanglement Entropy from Einstein Equation*, Phys. Rev. D **88** (2013) 026012 [arXiv:1304.7100 [hep-th]].

[31] N. Lashkari, M. B. McDermott and M. Van Raamsdonk, *Gravitational Dynamics From Entanglement "Thermodynamics*, arXiv:1308.3716 [hep-th].

[32] P. Di Francesco, P. Mathieu and D. Senechal, *Conformal field theory*, . New York, USA: Springer (1997) 890 p.

[33] P. Calabrese and J. Cardy, *Entanglement and correlation functions following a local quench: a conformal field theory approach*. J. Stat. Mechanics. (2007) P10004.

[34] P. Calabrese and J. Cardy, *Quantum Quenches in Extended Systems*, J. Stat. Mech. **0706** (2007) P06008 [arXiv:0704.1880 [cond-mat.stat-mech]].

[35] P. Calabrese and J. L. Cardy, *Time-dependence of correlation functions following a quantum quench*, Phys. Rev. Lett. **96** (2006) 136801, [cond-mat/0601225].

[36] S. Sotiriadis and J. Cardy, *Quantum quench in interacting field theory: A Self-consistent approximation*, Phys. Rev. B **81** (2010) 134305 [arXiv:1002.0167 [quant-ph]].

[37] S. Bravyi, M. B. Hastings and F. Verstraete, *Lieb-Robinson Bounds and the Generation of Correlations and Topological Quantum Order*, 2006 Phys. Rev. Lett. **97**, 050401 [quant-ph/0603121].

[38] S. J. Rey and J. T. Yee, *Macroscopic strings as heavy quarks in large N gauge theory and anti-de Sitter supergravity*, Eur. Phys. J. C **22** (2001) 379 [hep-th/9803001].

[39] J. M. Maldacena, *Wilson loops in large N field theories*, Phys. Rev. Lett. **80** (1998) 4859 [hep-th/9803002].

[40] A. Rényi, *On measures of information and entropy*, Proceedings of the 4th Berkeley Symposium on Mathematics, Statistics and Probability 1960. pp. 547-561.

[41] *The Holographic bound in anti-de Sitter space*, hep-th/9805114.

[42] T. Banks, M. R. Douglas, G. T. Horowitz and E. J. Martinec, *AdS dynamics from conformal field theory*, hep-th/9808016.

[43] S. W. Hawking and D. N. Page, *Thermodynamics of Black Holes in anti-De Sitter Space*, Commun. Math. Phys. **87** (1983) 577.

[44] S. Ryu and T. Takayanagi, *Aspects of Holographic Entanglement Entropy*, JHEP **0608** (2006) 045 [hep-th/0605073].

[45] R. M. Wald, *Black hole entropy is the Noether charge*, Phys. Rev. D **48** (1993) 3427 [gr-qc/9307038].

[46] R. Emparan, C. V. Johnson and R. C. Myers, Phys. Rev. D **60** (1999) 104001 doi:10.1103/PhysRevD.60.104001 [hep-th/9903238].

[47] U. H. Danielsson, E. Keski-Vakkuri and M. Kruczenski, *Spherically collapsing matter in AdS, holography, and shellons*, Nucl. Phys. B **563** (1999) 279 [hep-th/9905227].

[48] U. H. Danielsson, E. Keski-Vakkuri and M. Kruczenski, *Black hole formation in AdS and thermalization on the boundary*, JHEP **0002** (2000) 039 [hep-th/9912209].

[49] P. M. Chesler and L. G. Yaffe, *Horizon formation and far-from-equilibrium isotropization in supersymmetric Yang-Mills plasma*, Phys. Rev. Lett. **102** (2009) 211601 [arXiv:0812.2053 [hep-th]].

[50] G. Beuf, M. P. Heller, R. A. Janik and R. Peschanski, *Boost-invariant early time dynamics from AdS/CFT*, JHEP **0910** (2009) 043 [arXiv:0906.4423 [hep-th]].

[51] P. M. Chesler and L. G. Yaffe, *Boost invariant flow, black hole formation, and far-from-equilibrium dynamics in $N = 4$ supersymmetric Yang-Mills theory*, Phys. Rev. D **82** (2010) 026006 [arXiv:0906.4426 [hep-th]].

[52] S. Bhattacharyya and S. Minwalla, *Weak Field Black Hole Formation in Asymptotically AdS Spacetimes*, JHEP **0909** (2009) 034 [arXiv:0904.0464 [hep-th]].

[53] S. R. Das, T. Nishioka and T. Takayanagi, *Probe Branes, Time-dependent Couplings and Thermalization in AdS/CFT*, JHEP **1007** (2010) 071 [arXiv:1005.3348 [hep-th]].

[54] P. C. Vaidya, *The external field of a radiating star in general relativity*, Curr. Sci. **12** (1943) 183.

[55] P. C. Vaidya, *The gravitational field of a radiating star*, Pro. Indian Acad. A. 33 (1951) 264.

[56] S. W. Hawking and G. F. R. Ellis, *The Large scale structure of space-time*, Cambridge University Press, Cambridge, 1973.

[57] R. C. Myers and A. Sinha, *Holographic c-theorems in arbitrary dimensions*, JHEP **1101** (2011) 125 [arXiv:1011.5819 [hep-th]].

[58] K. Skenderis, *Lecture notes on holographic renormalization*, Class. Quant. Grav. **19** (2002) 5849 [hep-th/0209067].

[59] P. Figueras, V. E. Hubeny, M. Rangamani and S. F. Ross, *Dynamical black holes and expanding plasmas*, JHEP **0904** (2009) 137 [arXiv:0902.4696 [hep-th]].

[60] M. Headrick, *Entanglement Renyi entropies in holographic theories*, Phys. Rev. D **82** (2010) 126010 [arXiv:1006.0047 [hep-th]].

[61] H. Liu and S. J. Suh, *Entanglement Tsunami: Universal Scaling in Holographic Thermalization*, Phys. Rev. Lett. **112** (2014) 011601 [arXiv:1305.7244 [hep-th]].

[62] A. Polkovnikov, K. Sengupta, A. Silva and M. Vengalattore, *Nonequilibrium dynamics of closed interacting quantum systems*, Rev. Mod. Phys. **83**, 863 (2011) [arXiv:1007.5331 [cond-mat.stat-mech]].

[63] E. Fermi, J. Pasta and S. Ulam, May 1955, Document LA-1940.
G. P. Berman and F. M. Izrailev, *The Fermi-Pasta-Ulam problem: Fifty years of progress* Chaos, Volume 15, Issue 1, pp. 015104-015104-18 (2005). arXiv:nlin/0411062.

[64] S. M. Ulam, *A collection of mathematical problems*, (Interscience Inc., New York 1960).

[65] N. J. Zabusky and M. D. Kruskal, *Interaction of solitons in a collisions plasma and the recurrence of initial states*, Phys. Rev. Lett. **15**, 240-243 (1965).

[66] F. M. Izrailev and B. V. Chirikov, *Statistical Properties of a Nonlinear String*, Institute of Nuclear Physics, Novosibirsk, USSR, 1965.

[67] T. Kinoshita, T. Wenger and D.S. Weiss, *A quantum Newton's cradle*, 2006, Nature **440** 900.

[68] M. Gring, M. Kuhnert, T. Langen, T. Kitazgawa, B. Rauer, M. Schreitl, I. Mazets, D. A. Smith , E. Demler and J. Schmiedmayer, *Relaxation and Prethermalization in an Isolated Quantum System*, Science 337, 1318 (2012); DOI: 10.1126/science.1224953, arXiv:1112.0013.

[69] S. Trotzky, Y. -A. Chen, A. Flesch, I. P Mc Cullough, U. Schollwöck, J. Eisert and I. Bloch, *Probing the relaxation towards equilibrium in an isolated strongly correlated one-dimensional Bose gas*, Nature Physics 8, 325-330(2012) doi:10.1038/nphys2232, arxiv:1101.2659.

[70] E. Jaynes, Phys. Rev *Information Theory and Statistical Mechanics* **106**, 620, 1957.

[71] M. Rigol, V. Dunjko, V. Yurovsky and Maxim Olshanii. *Relaxation in a Completely Integrable Many-Body Quantum System: An Ab Initio Study of the Dynamics of the Highly Excited States in 1D Lattice Hard-Core Bosons*, Phys. Rev. Lett. 98, 050405 (2007).

[72] M. Kollar, F.A. Wolf and M. Eckstein, *Generalized Gibbs ensemble predicction of prethermalization plateaus and their relation to nonthermal steady states in integrable systems*, Physical Review B **84**, 054304 (2011).

[73] Adu Smith, et. al., *Prethermalization revealed by the relaxation dynamics of full distribution functions*, New Journal of Physics, arXiv 1212.4645.

[74] Giuseppe Mussardo, *Infinite-time Average of Local Fields in an Integrable Quantum Field Theory after a Quench*, arXiv[1308.4551].

[75] H. Casini, M. Huerta and R. C. Myers, *Towards a derivation of holographic entanglement entropy,* JHEP **1105**, 036 (2011) [arXiv:1102.0440 [hep-th]].

[76] A. Lewkowycz and J. Maldacena, *Generalized gravitational entropy*, JHEP **1308**, 090 (2013) [arXiv:1304.4926 [hep-th]].

[77] T. Albash and C. V. Johnson, *Evolution of Holographic Entanglement Entropy after Thermal and Electromagnetic Quenches*, New J. Phys. **13**, 045017 (2011) [arXiv:1008.3027 [hep-th]].

[78] V. Balasubramanian, A. Bernamonti, J. de Boer, N. Copland, B. Craps, E. Keski-Vakkuri, B. Muller and A. Schafer *et al.*, *Thermalization of Strongly Coupled Field Theories*, Phys. Rev. Lett. **106** (2011) 191601 [arXiv:1012.4753 [hep-th]].

[79] V. Balasubramanian, A. Bernamonti, J. de Boer, N. Copland, B. Craps, E. Keski-Vakkuri, B. Muller and A. Schafer *et al.*, [78] *Holographic Thermalization*, Phys. Rev. D **84** (2011) 026010 [arXiv:1103.2683 [hep-th]].

[80] D. Galante and M. Schvellinger, *Thermalization with a chemical potential from AdS spaces*, JHEP **1207** (2012) 096 doi:10.1007/JHEP07(2012)096 [arXiv:1205.1548 [hep-th]].

[81] A. Allais and E. Tonni, *Holographic evolution of the mutual information*, JHEP **1201** (2012) 102 doi:10.1007/JHEP01(2012)102 [arXiv:1110.1607 [hep-th]].

[82] V. E. Hubeny, *Extremal surfaces as bulk probes in AdS/CFT*, JHEP **1207** (2012) 093 doi:10.1007/JHEP07(2012)093 [arXiv:1203.1044 [hep-th]].

[83] X. Zeng and W. Liu, *Holographic thermalization in Gauss-Bonnet gravity*, Phys. Lett. B **726** (2013) 481 doi:10.1016/j.physletb.2013.08.049 [arXiv:1305.4841 [hep-th]].

[84] W. Baron, D. Galante and M. Schvellinger, *Dynamics of holographic thermalization*, JHEP **1303** (2013) 070 doi:10.1007/JHEP03(2013)070 [arXiv:1212.5234 [hep-th]].

[85] M. Nozaki, T. Numasawa and T. Takayanagi, *Holographic Local Quenches and Entanglement Density*, JHEP **1305** (2013) 080 [arXiv:1302.5703 [hep-th]].

[86] T. Takayanagi and T. Ugajin, *Measuring Black Hole Formations by Entanglement Entropy via Coarse-Graining*, JHEP **1011**, 054 (2010) [arXiv:1008.3439 [hep-th]].

[87] A. Ishibashi and R. M. Wald, Class. Quant. Gray. **21**, 2981 (2004).

[88] M. Choptuik, *Universality and scaling in gravitational collapse of a massless scalar field*, Phys. Rev. Lett. 1993, vol **70**(1), 9-12.

[89] F. Pretorius and M. W. Choptuik, *Gravitational collapse in (2+1)-dimensional AdS space-time*, Phys. Rev. D **62**, 124012 (2000) [gr-qc/0007008].

[90] P. Bizon and A. Rostworowski, *On weakly turbulent instability of anti-de Sitter space*, Phys. Rev. Lett. **107**, 031102 (2011) [arXiv:1104.3702 [gr-qc]].

[91] M. Greiner, O.Mandel, T.W. Hänsh and I. Bolch, *Collapse and revival of the matter wave field of a Bose-Einstein condensate* Nature **419**, 51 (2002).

[92] H. Rieger and F. Iglói, *Quantum relaxation after a quench in systems with boundaries*, Phys. Rev. Lett. **106** 035701 (2011);

[93] J. Häppölä, G.B. Halász, A. Hamma, *Revivals of a closed quantum system and Lieb-Robinson speed*, Phys. Rev. A **85**, 032114 (2012).

[94] John Cardy, *Thermalization and Revivals after a Quench in Conformal Field Theory*, [arXiv:1403.3040].

[95] J. Jalmuzna, A. Rostworowski and P. Bizon, *A Comment on AdS collapse of a scalar field in higher dimensions*, Phys. Rev. D **84**, 085021 (2011) [arXiv:1108.4539 [gr-qc]].

[96] O. J. C. Dias, G. T. Horowitz and J. E. Santos, *Gravitational Turbulent Instability of Anti-de Sitter Space* , Class. Quant. Grav. **29**, 194002 (2012) [arXiv:1109.1825 [hep-th]].

[97] D. Garfinkle and L. A. Pando Zayas, *Rapid Thermalization in Field Theory from Gravitational Collapse*, Phys. Rev. D **84**, 066006 (2011) [arXiv:1106.2339 [hep-th]].

[98] D. Garfinkle, L. A. Pando Zayas and D. Reichmann, *On Field Theory Thermalization from Gravitational Collapse*, JHEP **1202**, 119 (2012) [arXiv:1110.5823 [hep-th]].

[99] A. Buchel, L. Lehner and S. L. Liebling, *Scalar Collapse in AdS*, Phys. Rev. D **86**, 123011 (2012) [arXiv:1210.0890 [gr-qc]].

[100] O. J. C. Dias, G. T. Horowitz, D. Marolf and J. E. Santos, *On the Nonlinear Stability of Asymptotically Anti-de Sitter Solutions*, Class. Quant. Grav. **29**, 235019 (2012) [arXiv:1208.5772 [gr-qc]].

[101] M. Maliborski and A. Rostworowski, *Time-periodic solutions in Einstein AdS - massless scalar field system*, Phys. Rev. Lett. **111**, 051102 (2013) [arXiv:1303.3186 [gr-qc]].

[102] A. Buchel, S. L. Liebling and L. Lehner, *Boson Stars in AdS*, arXiv:1304.4166 [gr-qc].

[103] M. Maliborski and A. Rostworowski, *A comment on "Boson stars in AdS"* , arXiv:1307.2875 [gr-qc].

[104] P. Bizon and J. Jalmuzna, *Globally regular instability of AdS_3*, Phys. Rev. Lett. **111** (2013) 041102 [arXiv:1306.0317 [gr-qc]].

[105] M. Maliborski, *Instability of Flat Space Enclosed in a Cavity*, Phys. Rev. Lett. **109**, 221101 (2012) [arXiv:1208.2934 [gr-qc]].

[106] Kolmogorov, Andrey Nikolaevich *The local structure of turbulence in incompressible viscous fluid for very large Reynolds numbers*, Proceedings of the USSR Academy of Sciences (1941) 30: 299D303.

[107] M. P. Heller, R. A. Janik and P. Witaszczyk, *The characteristics of thermalization of boost-invariant plasma from holography*, Phys. Rev. Lett. **108** (2012) 201602 [arXiv:1103.3452 [hep-th]].

[108] M. P. Heller, D. Mateos, W. van der Schee and D. Trancanelli, *Strong Coupling Isotropization of Non-Abelian Plasmas Simplified*, Phys. Rev. Lett. **108** (2012) 191601 [arXiv:1202.0981 [hep-th]].

[109] O. J. C. Dias, G. T. Horowitz and J. E. Santos, *Black holes with only one Killing field,* JHEP **1107**, 115 (2011) [arXiv:1105.4167 [hep-th]].

[110] V.I. Yudovihc, *On the loss of smoothness of the solutions of Euler's equations with time* (Russian), Dinamika Sploshn. Sredy 16, 71 (1974).

[111] G. T. Horowitz and V. E. Hubeny, *Quasinormal modes of AdS black holes and the approach to thermal equilibrium*, Phys. Rev. D **62**, 024027 (2000) [hep-th/9909056].

[112] E. Berti, V. Cardoso and P. Pani, *Breit-Wigner resonances and the quasinormal modes of anti-de Sitter black holes*, Phys. Rev. D **79**, 101501 (2009) [arXiv:0903.5311 [gr-qc]].

[113] M. A. Cazalilla, *Effect of Suddenly Turning on Interactions in the Luttinger Model*, Phys. Rev. Lett.97.156403.

[114] W. H. Press, S.A. Teutolsky, W.T. Vetterling and B.P. Flannery *Numerical Recipes*, Cambridge Univ. Press. Section 17.3.

[115] C. V. Johnson, *Large N Phase Transitions, Finite Volume, and Entanglement Entropy*, arXiv:1306.4955 [hep-th].

[116] D. V. Fursaev, *Proof of the holographic formula for entanglement entropy,* JHEP **0609** (2006) 018 [hep-th/0606184].

[117] W. R. Kelly and A. C. Wall, *Coarse-grained entropy and causal holographic information in AdS/CFT*, arXiv:1309.3610 [hep-th].

[118] V. E. Hubeny and M. Rangamani, *Causal Holographic Information*, JHEP **1206** (2012) 114 [arXiv:1204.1698 [hep-th]].

[119] B. Swingle, *Entanglement Renormalization and Holography*, Phys. Rev. D **86** (2012) 065007 [arXiv:0905.1317 [cond-mat.str-el]].

[120] M. Nozaki, S. Ryu and T. Takayanagi, *Holographic Geometry of Entanglement Renormalization in Quantum Field Theories*, JHEP **1210** (2012) 193 [arXiv:1208.3469 [hep-th]].

[121] G. Vidal, *Entanglement Renormalization*, Phys. Rev. Lett. 99, 220405 (2007) [cond-mat/0512165].

[122] J. Haegeman, T. J. Osborne, H. Verschelde and F. Verstraete, *Entanglement Renormalization for Quantum Fields in Real Space*, Phys. Rev. Lett. **110** (2013) 10, 100402 [arXiv:1102.5524 [hep-th]].

[123] V. E. Hubeny and M. Rangamani, *Unstable horizons*, JHEP **0205** (2002) 027 [hep-th/0202189].